Understanding Lithosphere and Mantle Dynamics with Numerical Models Constrained by Observations

Thesis by
Xiaolin Mao

In Partial Fulfillment of the Requirements for the
Degree of
Doctor of Philosophy

CALIFORNIA INSTITUTE OF TECHNOLOGY
Pasadena, California

2019
Defended June 20, 2018

Xiaolin Mao
ORCID: 0000-0002-8410-4629

To my wife, Huan
and to my son, Ethan

ACKNOWLEDGEMENTS

Studying at Caltech has been a special journey for me which provided me with immeasurable intellectual and mental benefits. Without the help from many people, this thesis could not have been possible.

First of all, I want to thank my advisor, Mike Gurnis, for introducing me to the magic geodynamic world and allowing me to explore new directions. His guidance, encouragement, and patience over the years made it possible for us to overcome the challenges of research. I learned a lot from his critical thinking and breadth of knowledge during our discussions.

I would like to thank the other members of my thesis committee, including Mark Simons, Zhongwen Zhan, and Rob Clayton, for their suggestions and comments on my research. I also thank Mark and Rob for their wonderful geophysics field trip course into the Mojave Desert where I realized how geophysical data is collected. I also thank Zhongwen for his encouragement as a friend.

My sincere gratitude also goes out to other faculty members in Seismo Lab. Their classes and researches expanded my horizon in geophysics. My thanks also goes to Jean-Paul (Pablo) Ampuero and Dave May for their guidance and support during our collaborations on different research projects.

I am grateful to Donna Mireles, Rosemary Miller, Kim Baker-Gatchalian, Priscilla McLean and the rest of the administrative staff in Seismo Lab for all the help they have provided which made my life and work much easier.

I thank current and previous members in Mike's group: Wei Leng, Vishagan Ratnaswamy, Dunzhu Li, Ting Yang, Huiling Wang, Xi Liu, Pengfei Ma, Chris Grose, and Erin Hightower. Discussing with them during and after group meetings helped me to sort out a lot of technical problems and to improve my research.

In addition, I want to thank my officemates: Junle Jiang, Minyan Zhong, Zhe Jia, Ollie Stephenson, and Vasilije Dobrosavljevic. I also want to thank other students and post docs in the Seismo Lab who made it a delightful place: Chunquan Yu, Zefeng Li, Yenyu Lin, Justin Ko, Rachel Morrison, Daniel Bowden, Voon Hui Lai, Jorge Castillo, Jack Muir, Zhichao Shen, and everyone else.

My special thanks go to my friends at Caltech: Yiran Ma, Daoyuan Sun, Dongzhou Zhang, Yihe Huang, Junjie Yu, Han Yue, Yanghui Zhao, Qiong Zhang, Dandan

Zhang, Lingshen Meng, Shenji Wei, Junlong Kou, Jingjing Jiang, Yacong Zhou, Xingsheng Nuan, Baoyi Chen, Yunxuan Li, Liyin He, Xingyu Liu, and many others. Without them, my life at Pasadena would have been much less joyful.

I thank Kangchen Bai, Zhan Su, and Yingdi Luo for the meaningful discussions and memorable times at Caltech.

My deepest thanks go to my wife, Huan Tang, for her unconditional love and support and bringing me our lovely son, Ethan Mao.

ABSTRACT

Numerical studies play an important role in understanding lithospheric and mantle dynamics. In this thesis, we first develop and use multiphysics geodynamic models to study the evolution of subduction. Our geodynamic models are constrained by different geological and geophysical observations, including topography. We then use 3D numerical simulations of dynamic rupture with off-fault inelastic deformation to study the scaling between damage zone thickness and fault width. Finally, we study the mechanical strength and anisotropy in the continental collision region with flexural models and gravity and topography data.

Topography is valuable data for investigating lithosphere and mantle dynamics and constraining numerical studies. Topography prediction with forward models is well established at plate interiors, while it is still difficult to predict realistic topography at subduction zones. We use multiphysics geodynamic models to tackle this problem. Our models incorporate a true free surface, phase changes, and elasto-visco-plastic rheology. We also include surface processes, water migration and water weakening. We study the influences of different geophysical, petrological, and geochemical processes on topography and subduction zone evolution and show that surface geometry, surface processes, elasticity, and oceanic crust all strongly influence the stress state and deformation within plates, water weakening decouples the overriding plate and the subducting slab at the mantle wedge region and contributes to the initiation of overriding plate failure, and oceanic crust has a similar effect with sediments lubricating the subduction interface. Free slip surface topography and free surface topography have substantial differences, and free surface topography is influenced by different processes by adjusting the force balance. Application to the New Hebrides subduction zone suggests that deformation within a detached slab segment caused by the impact of the slab segment on the strong lower mantle explains the origin of the isolated deep earthquakes in the transition zone beneath the North Fiji Basin, and the difference in the seismic intensities between northern and southern deep earthquake clusters is caused by transition from strong deformation to weak deformation after the impact.

We apply our multiphysics approach to investigate the influence of inherited lithospheric heterogeneity on subduction initiation at the Puysegur Incipient Subduction Zone (PISZ) south of New Zealand. Our predictions fit the morphology of the Puysegur Trench and Ridge and the deformation history on the overriding plate. We

show how a new thrust fault forms and evolves into a smooth subduction interface, and how a preexisting weak zone can become a vertical fault inboard of the thrust fault during subduction initiation, consistent with two-fault system at PISZ. The model suggests that the PISZ may not yet be self-sustaining. We propose that the Snares Zone (or Snares Trough) is caused by plate coupling differences between shallower and deeper parts, that the tectonic sliver between two faults experiences strong rotation, and that low density material accumulates beneath the Snares Zone.

We then turn to the scaling between damage zone thickness and fault width. Field observations indicate that damage zone thickness scales with accumulated fault displacement at short displacements but saturates at a few hundred meters for displacements larger than a few kilometers. To explain this transition of scaling behavior, we conduct 3D numerical simulations of dynamic rupture with off-fault inelastic deformation on long strike-slip faults. We find that the distribution of coseismic inelastic strain is controlled by the transition from crack-like to pulse-like rupture propagation associated with saturation of the seismogenic depth. The yielding zone reaches its maximum thickness when the rupture becomes a stable pulse-like rupture. Considering fracture mechanics theory, we show that seismogenic depth controls the upper bound of damage zone thickness on mature faults by limiting the efficiency of stress concentration near earthquake rupture fronts. We obtain a quantitative relation between limiting damage zone thickness, background stress, dynamic fault strength, off-fault yield strength, and seismogenic depth, which agrees with first-order field observations. Our results help link dynamic rupture processes with field observations and contribute to a fundamental understanding of damage zone properties.

Finally, we investigate the interactions between mechanical strength and lithospheric deformations. Variation of lithospheric strength controls the distribution of stress and strain within plates and at plate boundaries. Simultaneously, deformation caused by localized stress and strain reduces the lithospheric strength. We calculate the effective elastic thickness, T_e, which is a proxy of lithospheric strength, and its anisotropy at the Zagros-Himalaya belt and surrounding regions. T_e varies from $<$ 5 km to over 100 km, and shows good correlations with geological boundaries. Along plate boundaries, mountain belts, and major faults, T_e is usually smaller than 30 km. In basins, T_e is between 30 - 60 km. In stable cratons, T_e is larger than 60 km. In the regions with low and intermediate strength (T_e $<$ 60 km), the extent of T_e anisotropy is usually large, and the weak direction of T_e anisotropy agrees well

with the directions of GPS data and crustal stress. In stable cratons, the extent of T_e anisotropy is usually small. Our results suggest that mechanical weakening is the dominate mechanism to reduce the lithospheric strength in regions where T_e is smaller than 60 km. In stable cratons, the effects of mechanical weakening can be ignored, and only thermal weakening resulting from mantle processes can modify the lithospheric strength substantially.

PUBLISHED CONTENT AND CONTRIBUTIONS

Ampuero, Jean Paul and Xiaolin Mao (2017). Upper limit on damage zone thickness controlled by seismogenic depth. *Fault Zone Dynamic Processes: Evolution of Fault Properties During Seismic Rupture*, 227:243. doi: 10.1002/9781119156895.ch13.

X.M. participated in the conception of the project, did the simulations, made the plots, and helped write the manuscript.

Mao, Xiaolin, Michael Gurnis, and Dave A May (2017). Subduction initiation with vertical lithospheric heterogeneities and new fault formation. *Geophysical Research Letters*, 44(22). doi: 10.1002/2017g1075389.

X.M. developed the conception of the project, did the simulations, made the plots, and dominated the writing of the manuscript.

Mao, Xiaolin, Michael Gurnis, and Dave A May (2018). Predicting subduction zone topography with multiphysics geodynamic models. *Journal of Geophysical Research: Solid Earth*, submitted.

X.M. developed the conception and the numerical tools of the project, did the simulations, made the plots, and dominated the writing of the manuscript.

TABLE OF CONTENTS

LIST OF ILLUSTRATIONS

Number *Page*

LIST OF TABLES

Chapter 1

INTRODUCTION

A thorough understanding of lithosphere and mantle dynamics is a precondition to a proper interpretation of the formation and distribution of tectonic structures and events. Such an understanding also helps us to investigate the interactions between the solid Earth and other Earth systems, such as surface processes driven by topographic evolution with long-term climate change, and fluid migration within subduction zones as components of water and carbon cycles. In the lithosphere and mantle system, different processes occur over a range of timescales and require different physical models to describe the force balances and energy transfers. Numerical computations constrained by observations are a powerful tool to study these complex lithosphere and mantle processes and to test different hypothesizes. My thesis contributes to a better understanding of the lithosphere and mantle dynamics in the following aspects: through the development of a comprehensive and self-consistent multiphysics approach to simulate the long-term evolution of the lithosphere and mantle system (Chapter 2); through the application of numerical models to different locations over short and long timescales (Chapter 2, 3 and 4); and finally, I present a study of the interactions between mechanical strength and lithospheric deformation in a continental collision region (Chapter 5).

1.1 A multiphysics approach for long term lithosphere and mantle dynamics

On a geological timescale, lithosphere and mantle behave like a highly viscous fluid, and the evolution of the system is mainly driven by density variations resulting from thermal and chemical anomalies. During the past few decades, large-scale and low resolution mantle convection models with free slip surface have been widely used, and these models give us a generalized picture of the pattern of mantle convection and show how plate tectonics interacts with mantle convection (Zhong and Gurnis, 1995; Tackley, 2000). However, significant limitations exist in these models generating realistic slab behaviors as well as other model predictions, including topography at subduction zones, due to the highly simplified physics used. Some models (e.g., Gerya et al., 2002) have attempted the inclusion of more physics into the mantle convection system and reproduced some complex and detailed geological phenomena, while the relative importance of these processes need to be discussed

in order to understand the controlling mechanism.

In Chapter 2, we develop a comprehensive and self-consistent multiphysics approach to simulate long-term lithosphere and mantle dynamics. We start with a more reasonable representation of Earth's surface. Earth's surface is a stress free boundary that deforms freely in response to the motion of material below. Simultaneously, the development of topography and surface processes (erosion and sedimentation) generate loads that affect lithosphere and mantle dynamics (Kaus et al., 2008, 2010). A true free surface coupled with surface processes is incorporated in our models overcoming the traditional free-slip representation of Earth's surface with a more reliable prediction of topography. We then include phases changes, water migration, and water weakening to address the effects of the complex petrological and geochemical processes in the subduction channel, oceanic crust, and mantle wedge on the force balance of subduction zone, which are usually highly simplified or ignored in computations. An elasto-visco-plastic rheology is used with our new numerical formulation to better describe the stress evolution within plates and slabs. To clarify the influence of different geophysical, petrological, and geochemical processes on topography and subduction zone evolution, we carry out a systematic study of models with different parameters.

We apply our new method to study the New Hebrides subduction zone. A substantial number of deep focus earthquakes near the bottom of the transition zone and isolated from active subducting slabs, occur beneath the North Fiji Basin. These earthquakes can be divided into two clusters: the northern cluster has a relatively well constrained shallow-dipping structure with a high level of seismicity, while the shape of southern cluster is poorly defined with much less seismicity. These isolated deep focus earthquakes are interpreted to be within detached slab segments (Hamburger and Isacks, 1987; Okal and Kirby, 1998; Richards et al., 2011). Phase transformations related to metastable peridotite in the cold slab material are used to explain the seismicity in detached stagnant slab segments (Okal and Kirby, 1998), while this theory alone can not account for the intensity difference if both clusters were related to detached slab segments (Richards et al., 2011). Reactivation of preexisting weak structures under deformation is another possible mechanism for deep earthquakes (Jiao et al., 2000), while it was not considered as a plausible explanation for these isolated deep earthquakes since it is not clear that what drives the deformation in these detached slab segments.

Finally, also in Chapter 2, we use a full subduction zone model, which generates self-

consistent slab detachment during the early stage of evolution for a young subducting plate connected to a large plate, to provide a possible context to understand the origin of the isolated deep earthquakes beneath the North Fiji Basin.. We use the transition from strong deformation to weak deformation in the detached slab after the impact of the slab segment into the strong lower mantle to explain the cause of the difference in seismic intensities between northern and southern deep earthquake clusters. The compuations also produces other interesting and reasonable phenomena, including overriding plate failure, back-arc spreading, and trench retreat.

1.2 Subduction initiation at the incipient Puysegur subduction zone

Subduction initiation is a vital phase of the plate tectonic cycle since it fundamentally alters the global force balance on tectonic plates. Numerical studies have advanced our understanding of under what circumstances and with what physical processes a new subduction zone can develop (Toth and Gurnis, 1998; Regenauer-Lieb et al., 2001; Gurnis et al., 2004; Nikolaeva et al., 2010; Thielmann and Kaus, 2012), but uncertainty still exists and key parameters related to subduction initiation remain poorly quantified mainly due to the lack of good constraints on numerical models. At the Puysegur Incipient Subduction Zone (PISZ), just south of New Zealand, the morphology of the Puysegur Ridge shows a characteristic change from uplift in the southern part, where the total convergence is less, and subsidence in the northern part, the Snares Zone (or Snares Trough), where the total convergence is largest. Discrete flat-topped segments, which are interpreted as the results of subaerial exposure and erosion, are also evident at both northern and southern parts of the Puysegur Ridge. The southernmost segment is close to sea level (-120 m), while a peak subsidence of $\sim$ 1800 m is found in the Snares Zone in the north, suggesting that the southern part has only experienced uplift, while there was uplift followed by subsidence in the Snares Zone (Collot et al., 1995; Lebrun et al., 1998; Gurnis et al., 2004). These topographic variations on the overriding plate are good constraints for the study of subduction initiation processes.

In Chapter 3, we use geodynamic models with a true free surface to track topographic changes and a model setup and boundary conditions tailored for PISZ to investigate subduction initiation. We test our hypothesis for the formation of the two-fault system at PISZ, while exploring the factors that control the transition in the force balance. We focus on the evolution of topography and state of stress.

1.3 Investigating the scaling between damage zone thickness and fault width with 3D dynamic rupture simulations

A typical fault zone architecture comprises a highly deformed core surrounded by a damage zone composed of rocks with higher fracture density and lower elastic moduli than the host rocks. In most mature faults, damage zones are 100 to 400 m wide and have between 20% and 60% wave velocity reductions relative to their country rock (e.g., Huang and Ampuero, 2011). Studying the formation of damage zones provides insight into the mechanical, hydraulic and seismic behavior of faults. Fault zone damage is in part inherited from the early process of fracture coalescence and strain localization that led to the formation of the fault, and in part results from damage during earthquakes (Mitchell and Faulkner, 2009). Damage zone thickness, defined as a characteristic scale of the cross-fault distribution of fracture density, varies from a few centimeters on small faults to a few hundred meters on large mature faults. Field observations indicate that damage zone thickness scales with accumulated fault displacement, which is a measure of fault maturity, but generally saturates at a few hundred meters for fault displacements larger than a few km (Mitchell and Faulkner, 2009; Savage and Brodsky, 2011).

In Chapter 4, we use 3D numerical simulations of dynamic rupture on strike-slip faults with large aspect ratios to study first-order aspects of the off-fault yielding pattern in long faults. In particular, we assess the role of seismogenic depth in limiting fault zone width. The ingredients of our model are intentionally minimalistic: material properties surrounding the fault are uniform, a linear slip-weakening friction law is assumed on the fault. Comparing results of simulations with different seismogenic depths, we find that the distribution of inelastic strain is controlled by the transition from crack-like to pulse-like rupture propagation associated with saturation of the seismogenic depth. The yielding zone reaches its maximum thickness when the rupture becomes a stable pulse-like rupture. We develop quantitative insight, from the perspective of fracture mechanics, on how the transition to pulse-like rupture in long faults explains the saturation of damage zone thickness with accumulated fault displacement. In particular, we show that seismogenic depth controls the upper limit of damage zone thickness on mature faults. We discuss how our results help to link dynamic rupture models with field observations, and contribute to a fundamental understanding of damage zone properties.

1.4 Mechanical strength and anisotropy of the lithosphere in continental collision region

The classic plate tectonic theory assumes that plate boundaries accommodate most of the plate deformation, generating large earthquakes in a relatively narrow zone, while the plate interior is rigid with little deformation. However, in the continents, large plates are divided into blocks and are connected with suture zones. Deformations often extend into the interior of a plate as suggested by large earthquakes within the plate (Zhang et al., 2003). At continental collision regions, the deformation zone is usually wide, sometimes even wider than 1000 km (Kreemer et al., 2003). These observations contradict the classic plate tectonic theory, and in order to explain these phenomena, study of the strength variation of continental plates and plate boundaries is needed. In addition to the important tectonic meaning, understanding the strength variation in the continents and its interaction with lithospheric deformation contributes to a better estimation of seismic hazards.

In Chapter 5, we study the variations of mechanical strength and anisotropy of the lithosphere at the Zagros-Himalaya belt and surrounding regions. The Zagros-Himalaya belt is one of the most active continental deformation region that is surrounded by relative stable continental blocks, which makes it a widely used region to investigate the interactions between lithospheric strength and deformation. We compare the variation of lithospheric strength with the distributions of plate boundaries, major faults, and intermediate and large earthquakes within the context of lithospheric strength and active deformations. The geophysical interpretations of the mechanical anisotropy of the lithosphere are discussed by comparing the weak direction of the mechanical anisotropy with the directions of surface displacements (from GPS), crustal stress, and SKS shear wave splitting.

References

Collot, Jean-Yves, Geoffroy Lamarche, Ray A Wood, Jean Delteil, Marc Sosson, Jean-Frédéric Lebrun, and Mike F Coffin (1995). Morphostructure of an incipient subduction zone along a transform plate boundary: Puysegur Ridge and Trench. *Geology*, 23(6):519–522. doi: 10.1130/0091-7613(1995)023<0519:MOAISZ>2.3.CO;2.

Gerya, Taras V, Bernhard Stöckhert, and Alexey L Perchuk (2002). Exhumation of high-pressure metamorphic rocks in a subduction channel: A numerical simulation. *Tectonics*, 21(6). doi: 10.1029/2002tc001406.

Gurnis, Michael, Chad Hall, and Luc Lavier (2004). Evolving force balance during

incipient subduction. *Geochemistry, Geophysics, Geosystems*, 5(7). doi: 10.1029/2003gc000681.

Hamburger, Michael W and Bryan L Isacks (1987). Deep earthquakes in the southwest Pacific: A tectonic interpretation. *Journal of Geophysical Research: Solid Earth*, 92(B13):13841–13854. doi: 10.1029/jb092ib13p13841.

Huang, Yihe and Jean-Paul Ampuero (2011). Pulse-like ruptures induced by low-velocity fault zones. *Journal of Geophysical Research: Solid Earth*, 116(B12). doi: 10.1029/2011jb008684.

Jiao, Wenjie, Paul G Silver, Yingwei Fei, and Charles T Prewitt (2000). Do intermediate-and deep-focus earthquakes occur on preexisting weak zones? An examination of the Tonga subduction zone. *Journal of Geophysical Research: Solid Earth*, 105(B12):28125–28138. doi: 10.1029/2000jb900314.

Kaus, Boris JP, Clare Steedman, and Thorsten W Becker (2008). From passive continental margin to mountain belt: insights from analytical and numerical models and application to taiwan. *Physics of the Earth and Planetary Interiors*, 171(1):235–251. doi: 10.1016/j.pepi.2008.06.015.

Kaus, Boris JP, Hans Mühlhaus, and Dave A May (2010). A stabilization algorithm for geodynamic numerical simulations with a free surface. *Physics of the Earth and Planetary Interiors*, 181(1):12–20. doi: 10.1016/j.pepi.2010.04.007.

Kreemer, Corné, William E Holt, and A John Haines (2003). An integrated global model of present-day plate motions and plate boundary deformation. *Geophysical Journal International*, 154(1):8–34. doi: 10.1046/j.1365-246x.2003.01917.x.

Lebrun, Jean-Frédéric, Garry D Karner, and Jean-Yves Collot (1998). Fracture zone subduction and reactivation across the Puysegur ridge/trench system, southern New Zealand. *Journal of Geophysical Research: Solid Earth*, 103(B4):7293–7313. doi: 10.1029/98JB00025.

Mitchell, TM and DR Faulkner (2009). The nature and origin of off-fault damage surrounding strike-slip fault zones with a wide range of displacements: A field study from the atacama fault system, northern chile. *Journal of Structural Geology*, 31(8):802–816. doi: 10.1016/j.jsg.2009.05.002.

Nikolaeva, K, TV Gerya, and FO Marques (2010). Subduction initiation at passive margins: numerical modeling. *Journal of Geophysical Research: Solid Earth*, 115(B3). doi: 10.1029/2009jb006549.

Okal, Emile A and Stephen H Kirby (1998). Deep earthquakes beneath the Fiji Basin, SW Pacific: Earth's most intense deep seismicity in stagnant slabs. *Physics of the Earth and Planetary Interiors*, 109(1-2):25–63. doi: 10.1016/s0031-9201(98)00116-2.

Regenauer-Lieb, Klaus, Dave A Yuen, and Joy Branlund (2001). The initiation of subduction: criticality by addition of water? *Science*, 294(5542):578–580. doi: 10.1126/science.1063891.

Richards, Simon, Robert Holm, and Grace Barber (2011). When slabs collide: A tectonic assessment of deep earthquakes in the Tonga-Vanuatu region. *Geology*, 39(8):787–790. doi: 10.1130/g31937.1.

Savage, Heather M and Emily E Brodsky (2011). Collateral damage: Evolution with displacement of fracture distribution and secondary fault strands in fault damage zones. *Journal of Geophysical Research: Solid Earth*, 116(B3). doi: 10.1029/2010jb007665.

Tackley, Paul J (2000). Mantle convection and plate tectonics: Toward an integrated physical and chemical theory. *Science*, 288(5473):2002–2007. doi: 10.1126/science.288.5473.2002.

Thielmann, Marcel and Boris JP Kaus (2012). Shear heating induced lithospheric-scale localization: Does it result in subduction? *Earth and Planetary Science Letters*, 359:1–13. doi: 10.1016/j.epsl.2012.10.002.

Toth, John and Michael Gurnis (1998). Dynamics of subduction initiation at pre-existing fault zones. *Journal of Geophysical Research: Solid Earth*, 103(B8): 18053–18067. doi: 10.1029/98jb01076.

Zhang, Peizhen, Qidong Deng, Guomin Zhang, Jin Ma, Weijun Gan, Wei Min, Fengying Mao, and Qi Wang (2003). Active tectonic blocks and strong earthquakes in the continent of China. *Science in China Series D: Earth Sciences*, 46 (2):13–24. doi: 10.1002/cjg2.699.

Zhong, Shijie and Michael Gurnis (1995). Mantle convection with plates and mobile, faulted plate margins. *Science*, 267(5199):838–843. doi: 10.1126/science.267.5199.838.

Chapter 2

PREDICTING SUBDUCTION ZONE TOPOGRAPHY WITH MULTIPHYSICS GEODYNAMIC MODELS

Topography is valuable data to investigate lithosphere and mantle dynamics and to constrain numerical studies. Topography prediction with forward models is well established at plate interiors, while it is still difficult to predict realistic topography at subduction zones. We use multiphysics geodynamic models to tackle this problem. Our models incorporate a true free surface, phase changes and elasto-visco-plastic rheology. We also include surface processes, water migration and water weakening. We study the influences of different geophysical, petrological and geochemical processes on topography prediction and subduction zone evolution and show that surface geometry, surface processes, elasticity and oceanic crust all strongly influence the stress state and deformation within plates, water weakening decouples the overriding plate and the subducting slab at the mantle wedge region and contributes to the initiation of overriding plate failure, and oceanic crust has a similar effect with sediments lubricating the subduction interface. Free slip surface topography and free surface topography have substantial differences, and free surface topography is influenced by different processes by adjusting the force balance. Application to the New Hebrides subduction zone suggests that deformation within a detached slab segment caused by the impact of the slab segment on the strong lower mantle explains the origin of the isolated deep earthquakes in the transition zone beneath the North Fiji Basin, and the difference in the seismic intensities between northern and southern deep earthquake clusters is caused by transition from strong deformation to weak deformation after the impact.

2.1 Introduction

Numerical studies play an important role in understanding subduction zone evolution and are constrained by different observations, including plate velocity, topography, internal slab deformation, and slab morphology. Among these observations, topography contains abundant information with little uncertainty. However, there are still substantial difficulties in the prediction of subduction zone topography with numerical models, which limit usage of this valuable data. We arrive at a multiphysics approach to this problem by reviewing the related geophysical, petrological, and

geochemical processes that are interconnected through the complex force balance at subduction zones.

A proper representation of the Earth's surface in numerical models is crucial for the prediction of subduction zone topography. Earth's surface is a stress free boundary that deforms freely in response to the motion of material below. Simultaneously, the development of topography and surface processes (erosion and sedimentation) generate loads that affect lithosphere and mantle dynamics (Kaus et al., 2008, 2010). Two kinds of boundary conditions, free slip surface and free surface, are commonly used to approximate Earth's surface. A free slip surface, where both the normal velocity and tangent stress at the surface are zero, has been used in mantle convection studies extensively since it does not require mesh update and is thought to be a good approximation of the Earth's surface for large scale mantle convections models (e.g., McKenzie et al., 1974; Zhong and Gurnis, 1995). However, a free slip surface does not satisfy the stress free nature of Earth's surface, and it may significantly influence the stress state within the lithosphere and slab dynamics (Gurnis et al., 1996; Kaus et al., 2010; Thielmann et al., 2015). Instantaneous topography can be derived via the normal stress at the free slip surface (e.g., Zhong and Gurnis, 1994; Andrews and Billen, 2009), while the accuracy of the stress-derived topography depends on lateral viscosity variations near the surface and topographic slopes and amplitudes (King, 2009; Crameri et al., 2017). On the other hand, a free surface, where both the normal and tangent stresses are zero at the surface, is a more natural approximation of Earth's surface, but needs frequent mesh updates to track its evolution. A common implementation of the free surface which avoids mesh update is through introducing a weak layer with low viscosity and usually zero density ('sticky air') between the lithosphere and the actual flat surface boundary (e.g., Gerya et al., 2004; Leng and Gurnis, 2011). Topography is defined by the material interface between the 'sticky air' and solid materials. Despite its simplicity, the sticky air method can approximate the free surface-like behavior of the lithosphere well and gives reasonable topographic predictions (Schmeling et al., 2008; Crameri et al., 2012a). However, a shortcoming of the 'sticky air' method is that it is hard to couple the surface processes with the lithosphere and mantle dynamics explicitly since the material interface is not an actual boundary of the model, where the coupling is usually defined (e.g., Avouac and Burov, 1996; Salles et al., 2017). A true free surface method, where a stress free boundary follows the motion of the material below, is capable of tracking accurate topographic evolution, including the interaction between surface processes and deeper dynamics. A drawback of this

approach is its computational expense as it requires frequent remeshing (e.g., Braun and Sambridge, 1994).

The force balance at subduction zone is also influenced by the complex petrological and geochemical processes in the subduction channel, oceanic crust, and mantle wedge, which are usually highly simplified or ignored in numerical models. In large scale, low resolution mantle convection models, the lithosphere is often treated as a high viscosity layer with homogeneous chemical composition, and only the first order phase changes are considered (e.g., the olivine-spinel phase change at 410 km and the spinel-perovskite phase change at 660 km) (e.g., Tackley et al., 1993; Zhong and Gurnis, 1995). These models give us a big picture of the pattern of mantle convection and show how plate tectonics interact with mantle convection, while they could have problems with generating self-consistent single-sided subduction, while their predicted topographies smooth out important details. Including a weak, low viscosity crust layer on top of the lithosphere helps to lubricate the decoupling process between the subducting and the overriding plates and to produce more realistic slab behaviors (e.g., Crameri et al., 2012b). The density difference between the oceanic crust and the lithospheric mantle may or may not be considered, and the basalt-eclogite phase transition can be incorporated as a change in the density at some depth or temperature and pressure condition (e.g., Hu et al., 2016; Liu and Currie, 2016). Fluid migration related to this phase change is usually neglected, while a large weak zone may be imposed in the mantle wedge to simulate the fluids weakening effects in this region and to further decouple the subducting and overriding plates (e.g., Manea and Gurnis, 2007; Liu and Stegman, 2011). These simple methods of including the oceanic crust and/or the related phase changes into a mantle convection model are able to generate realistic slab behaviors, while the inconsistency introduced by the constant low viscosity and the imposed weak zone could bring bias into model predictions, including topography. On the other hand, incorporating a number of material types and sophisticated phase changes into the subduction system can help to reproduce some complex and detailed geological phenomena, including the exhumation of high-pressure metamorphic rocks in subduction channel (Gerya et al., 2002; Li et al., 2010), and to predict realistic topography, while the relative importance of these processes needs to be discussed in order to understand the controlling mechanism.

The complex rheology of the lithosphere and mantle and the unclear relative importance of elasticity introduce some uncertainties in the prediction of subduction

zone topography. On geological time scales, the lithosphere and mantle behave like highly viscous fluids, and their viscosities are strongly temperature dependent, which results in a relatively low effective viscosity ($10^{18} - 10^{21}$ Pa s) in the mantle due to the high temperature and a high effective viscosity (generally $> 10^{23}$ Pa s, sometimes $\sim 10^{26}$ Pa s or even larger) in the lithosphere with the low temperature (e.g., Li et al., 2017; Mallard et al., 2016). Large viscosity variation in the mantle and in the lithosphere causes viscous and viscoelastic behaviors on geological time scales in these two regions respectively, while the influence of elasticity on subduction zone evolution is still unclear and often overlooked. Theoretical studies with numerical models suggest that the shape, the velocities, and the stress state of the subducting slab are significantly altered if a viscoelastic rheology is used instead of a viscous rheology (e.g., Moresi et al., 2002; Fourel et al., 2014; Farrington et al., 2014), while the model setups in these studies are usually too simple compared to real subduction zones, and some important parts of the rheology may be ignored (e.g., plasticity or temperature dependence of the viscosity). On the other hand, plate bending models that fit the trench and outer rise topography profiles show that various rheologic models, including purely elastic, purely viscous and elasto-plastic models, could give similar topography predictions (e.g., Caldwell and Turcotte, 1979; Bremaecker, 1977; Goetze and Evans, 1979). Geodynamic models with viscous rheologies are also able to reproduce the trench and outer rise topography, which indicates that the lithosphere may not retain any elastic strength within the subduction zone (e.g., Gurnis et al., 2000). Gravity measurements within the Kermadec trench show a large-magnitude decrease in the flexural rigidity from the outer rise to the trench axis, which also suggests that the plate has little or no elastic strength within the trench (Billen and Gurnis, 2005). The discrepancy on the importance of elasticity between theoretical and data-based studies may be related to the pervasive yielding and normal faults on the subducting plates that form when the slab enters the trench, strongly reducing lithospheric strength regionally. Again, this implies that the influence of elasticity cannot be isolated from other factors involved in the force balance at subduction zones.

To address the influences of various processes on the prediction of subduction zone topography, we treat it as a multiphysics problem and include most of the important geophysical, petrological, and geochemical processes that affect the force balance. However, full implementation of all these processes involves some physical models that are still under exploration and may be computationally expensive or even currently intractable for a fully coupled subduction zone system, e.g., the

long distance fluvial erosion and transport, the hydrous melting processes, and the separation between melts and solids (two phase flow problem). Nevertheless, we incorporate most of the currently tractable and potentially important processes into our model. The goal of this chapter is to introduce the method used to predict realistic high resolution topography for incipient subduction (Mao et al., 2017) and to discuss how the topography and lithosphere and mantle dynamics are influenced by different processes. To that end, we evaluate the model output sensitivity to different physical processes (e.g., free surface, surface processes, elasticity, ...) in small scale domains of dimensions 800 km x 300 km. In addition, we present a single full subduction zone model (2500 km x 1000 km) which is compatible to the New Hebrides subduction zone at last to show the realistic model predictions using our new method.

2.2 Method

Governing equations for lithosphere and mantle flow

Under the Boussinesq approximation for an incompressible fluid, the conservation equations of mass and momentum are

$$\nabla \cdot \boldsymbol{u} = 0 \tag{2.1}$$

$$\nabla \cdot \boldsymbol{\tau} - \nabla p = \boldsymbol{f}, \tag{2.2}$$

where $\boldsymbol{\tau}$ represents the deviatoric stress tensor, and its expression is given later since it depends on the visco-elastic model. Here, $\boldsymbol{u}$,p are the velocity and the pressure, respectively, $\boldsymbol{f}$ is the body force, and $\boldsymbol{f} = \rho \boldsymbol{g}$, where ρ is the density, and $\boldsymbol{g}$ is the acceleration of gravity. Through the body force term, density differences resulting from thermal anomalies, phase changes, and chemical heterogeneities provide the driving forces for mantle convection.

Equations (2.1) and (2.2) are closed with boundary conditions,

$$\boldsymbol{u}|_{\Gamma_D} = \bar{\boldsymbol{u}} \tag{2.3}$$

$$\boldsymbol{\sigma} \cdot \boldsymbol{n}|_{\Gamma_N} = \bar{\mathbf{T}}, \tag{2.4}$$

where $\boldsymbol{\sigma}$ is the total stress, $\boldsymbol{\sigma} = \boldsymbol{\tau} - p\boldsymbol{I}$, $\bar{\mathbf{T}}$ is the traction vector, and $\boldsymbol{n}$ is the outward pointing normal to the boundary $\partial\Omega$. Γ_D and Γ_N denote the regions along the boundary $\partial\Omega$ where the Dirichlet and Neumann boundary conditions are applied.

The conservation equation of energy is

$$\frac{\partial T}{\partial t} = -\boldsymbol{u} \cdot \nabla T + \kappa \nabla^2 T + H, \tag{2.5}$$

where T is the temperature, κ is the thermal diffusivity, and H is the heat source. We assume Dirichlet conditions for the temperature on the top and bottom, and no-flux conditions on the other (side) boundaries,

$$T|_{\Gamma_D} = \bar{T} \tag{2.6}$$

$$\nabla T \cdot \boldsymbol{n}|_{\partial\Omega\setminus\Gamma_D} = 0. \tag{2.7}$$

Rheology

The nonlinear visco-plastic rheology includes the influence of elasticity by modifying the viscosity and body force term of the Stokes equation. We consider the dislocation creep mechanism for the steady-state lithosphere and mantle flow. The reference viscosity is temperature, strain rate, and composition-dependent

$$\eta_0 = A^{-\frac{1}{n}} \dot{\varepsilon}_{\mathrm{II}}^{\frac{1-n}{2n}} exp\left(\frac{E}{nRT}\right), \tag{2.8}$$

where A is a material constant which differs greatly between assemblages, $\dot{\varepsilon}_{\mathrm{II}}$ is the second invariant of the strain rate tensor, E is the activation energy for the creep, R is the universal gas constant and n is the stress exponent. In the mantle, the viscosity is also influenced by water in olivine (Hirth and Kohlstedt, 1996)

$$\eta = \begin{cases} \frac{C_{OH}^0}{C_{OH}}\eta_0, & \text{if } C_{OH} > C_{OH}^0; \\ \eta_0, & \text{otherwise,} \end{cases} \tag{2.9}$$

where C_{OH} is the total water content, and C_{OH}^0 is the critical water content.

Plastic deformation of the material is included by enforcing the deviatoric stress within the yield stress limit by modifying the viscosity

$$\eta_y = \min\left(\frac{\tau_y}{2\sqrt{\dot{\varepsilon}_{\mathrm{II}}}}, \eta\right), \tag{2.10}$$

where τ_y is the yield stress based on the Drucker-Prager yield criterion (e.g., Lemiale et al., 2008), and

$$\tau_y = \min(\sin\varphi p + \cos\varphi C, \tau_{ymax}), \tag{2.11}$$

where φ is the material friction angle, C is the cohesion, and τ_{ymax} is the maximum yield stress. Linear softening respect to accumulated plastic strain, ε_p, is applied to the friction angle and the cohesion

$$\varphi = \varphi_f + (\varphi_0 - \varphi_f)\left(1 - \min\left(1, \frac{\varepsilon_p}{\varepsilon_0}\right)\right) \tag{2.12}$$

$$C = C_f + (C_0 - C_f)\left(1 - \min\left(1, \frac{\varepsilon_p}{\varepsilon_0}\right)\right), \tag{2.13}$$

where ε_0 is the reference plastic strain, and φ_0, φ_f, C_0 and C_f are the initial and final friction angles and cohesions, respectively. Plastic strain is recorded on the Lagrangian markers, and its evolution is governed by

$$\frac{D\varepsilon_p}{Dt} = \begin{cases} \dot{\varepsilon}_{\mathrm{II}}, & \text{if } \sqrt{\tau_{\mathrm{II}}} > \tau_y; \\ 0, & \text{otherwise,} \end{cases} \tag{2.14}$$

where D/Dt is the material derivative.

The final effective viscosity is obtained by applying the highest and lowest viscosity cutoffs

$$\eta_{eff} = \max\left(\eta_{min}, \min(\eta_{max}, \eta_y)\right), \tag{2.15}$$

where η_{min} and η_{max} are the minimum and maximum viscosities respectively. The rheological parameters we use are given in Table 2.1.

Table 2.1: Rheological parameters

Parameter	Value
maximum viscosity cutoff (η_{max})	10^{24} Pa s
minimum viscosity cutoff (η_{min})	10^{18} Pa s
critical water content in mantle (C^0_{OH})	100 ppm
[a]preexponential factor in mantle (A_m)	2.5 x 10^4 MPa^{-n} s^{-1}
[a]exponent in mantle (n_m)	3.2
[a]activation energy in mantle (E_m)	540 kJ mol^{-1}
[b]preexponential factor in crust (A_c)	3.3 x 10^{-4} MPa^{-n} s^{-1}
[b]exponent in crust (n_c)	3.2
[b]activation energy in crust (E_c)	238 kJ mol^{-1}
[c]preexponential factor in sediment (A_s)	7 x 10^{-6} MPa^{-n} s^{-1}
[c]exponent in sediment (n_s)	2.3
[c]activation energy in sediment (E_s)	154 kJ mol^{-1}
shear modulus (G)	50 GPa
maximum yield stress (τ_{ymax})	150 MPa
minimum yield stress (τ_{ymin})	3 MPa
initial cohesion in mantle and crust (C_0)	40 MPa
final cohesion for all materials (C_f)	3 MPa
initial friction angle in mantle and crust (φ_0)	0.6
final friction angle for all materials (φ_f)	0
reference plastic strain (ε_0)	0.4
constant yield stress in sediment	3 MPa

[a]dry olivine, [b]plagioclase, [c]quartz.

True free surface and surface processes

The true free surface is achieved by applying zero traction Neumann boundary condition (by setting the traction force $\bar{\mathbf{T}}$ to $\bar{\mathbf{0}}$ in equation (2.4)) on the top of the model domain to obtain the surface velocity from the Stokes equation and then in turn updating the surface. The evolution of the topography, H, with respect to the surface velocity is governed by

$$\frac{\partial H}{\partial t} = -\boldsymbol{u_h} \cdot \nabla H + u_v, \tag{2.16}$$

where $\boldsymbol{u_h}$ and u_v are horizontal and vertical components of the surface velocity respectively, and ∇H is the horizontal gradient of the topography.

The influence of surface processes are incorporated, by considering a simple law of topographic changes that simulate erosion and sedimentation at the scale of several tens of kilometers (Avouac and Burov, 1996; Jourdon et al., 2017). Assuming the rate of downslope transport of debris, $\boldsymbol{q_e}$, is proportional to the local slope, we have

$$\boldsymbol{q_e} = -\kappa_s \nabla H, \tag{2.17}$$

where κ_s is the mass diffusivity coefficient. From mass conservation law,

$$\frac{\partial H}{\partial t} = -\nabla \cdot \boldsymbol{q_e}. \tag{2.18}$$

With constant κ_s, equations (2.17) and (2.18) lead to the linear diffusion equation

$$\frac{\partial H}{\partial t} = \kappa_s \nabla^2 H. \tag{2.19}$$

Combining the effects of surface advection, uplift and diffusion, we have

$$\frac{\partial H}{\partial t} = -\boldsymbol{u_h} \cdot \nabla H + u_v + \kappa_s \nabla^2 H. \tag{2.20}$$

Phase changes and water migration

Changes in density and water content of the lithosphere and mantle are tracked by referring to pre-calculated phase maps and transporting free water within the system. Three-dimensional (temperature, pressure, and total water content) phase maps for density and free water content are calculated for different rock types using an efficient software Perplex (Connolly, 2005), which solves the classical non-linear free energy minimization problem of phase equilibria through linear programing by representing the continuous compositional variations of solutions phases with a series of discrete compositions. Chemical compositions for different rocks used are

given in Table 2.2 (Gerya et al. (2006) and reference therein), and different solution models are used for shallow and deeper mantle (Connolly and Petrini, 2002; Stixrude and Lithgow-Bertelloni, 2011). Melts are not considered in our petrological models due to the difficulties on the calculation of the related phase equilibria and the migration of melts within a deforming matrix.

Darcy's law is used to migrate free water, and the velocity separating water from the solid is simplified as

$$\boldsymbol{v}_{water} = -C_\phi \phi^{n_\phi - 1} \boldsymbol{g}, \tag{2.21}$$

where ϕ is the mean free water fraction, n_ϕ is a constant related to pore geometry, and C_ϕ is a blended constant that depends on several parameters, including the characteristic length of transport, the fluid viscosity, and the density difference between fluid and solids (Hebert et al., 2009).

Table 2.2: Rock compositions (weight %)

	pyrolite	altered basalt	sediment	harzburgite
SiO2	45.55	51.75	61.10	44.5
Al2O3	4.03	10.19	12.43	1.7
FeO	7.47	7.06	5.43	9.6
MgO	37.42	14.94	2.59	42.6
CaO	3.18	13.88	6.21	1.4
Na2O	0.33	2.18	2.54	0.1
K2O	0.03	0.15	1.0	0.03
H2O[a]	0.01	2.68	7.29	0.01

[a]Initial water content.

Elastic Viscous Stress Splitting

With a modified viscous flow code, elasticity is usually implemented by adjusting the effective viscosity and the right-hand-side of the Stokes equation (Moresi et al., 2002). We introduce the basic ideas and formulas of the elastic viscous stress splitting (EVSS) model (Keunings, 2000), and then show how we incorporate the EVSS model into the visco-plastic system presented in the rheology section to obtain the elasto-visco-plastic behaviors of the materials.

The primary reason that why we use an EVSS model instead of the traditional Maxwell model is because the stress evolution with a Maxwell model depends strongly on the time step. During the computations, time step varies considerably, causing a change in the stress state and leading to numerical instability. On the

other hand, the EVSS model could help to stabilize the stress evolution with the additional viscous term. The EVSS model is built upon the following deviatoric stress decomposition:

$$\boldsymbol{\tau} = 2\eta_v \dot{\boldsymbol{\varepsilon}} + \boldsymbol{\tau}_e, \tag{2.22}$$

where the $2\eta_v \dot{\boldsymbol{\varepsilon}}$ term denotes the contribution from the purely viscous component to the shear stress, and $\boldsymbol{\tau}_e$ is the contribution from the visco-elastic component. η_v is the viscosity of the purely viscous component (defined later with Eq. (2.27)), and $\dot{\boldsymbol{\varepsilon}}$ is the strain rate tensor defined as

$$\dot{\varepsilon}_{ij} = \frac{1}{2}\left(\frac{\partial u_i}{\partial x_j} + \frac{\partial u_j}{\partial x_i}\right). \tag{2.23}$$

The stress on the visco-elastic component, $\boldsymbol{\tau}_e$, is recorded on the marker and evolves according to the following:

$$\frac{\boldsymbol{\tau}_e}{2\eta_e} + \frac{1}{2G}\left(\frac{D\boldsymbol{\tau}_e}{Dt} + \boldsymbol{J}(\boldsymbol{u}, \boldsymbol{\tau}_e)\right) = \dot{\boldsymbol{\varepsilon}}, \tag{2.24}$$

where η_e and G are the viscosity (defined later with Eq. (2.28)) and shear modulus of the visco-elastic component respectively, and $\frac{D\boldsymbol{\tau}_e}{Dt} + \boldsymbol{J}(\boldsymbol{u}, \boldsymbol{\tau}_e)$ is the Jaumann corotational stress rate, where

$$\boldsymbol{J}(\boldsymbol{u}, \boldsymbol{\tau}_e) = \boldsymbol{\tau}_e \boldsymbol{W} - \boldsymbol{W}\boldsymbol{\tau}_e, \tag{2.25}$$

and $\boldsymbol{W}$ is the rotation tensor,

$$W_{ij} = \frac{1}{2}\left(\frac{\partial u_i}{\partial x_j} - \frac{\partial u_j}{\partial x_i}\right). \tag{2.26}$$

The partition of the total viscosity (η defined by Eq. (2.9)) into these two components is given by

$$\eta_v = (1 - \xi)\eta \tag{2.27}$$

$$\eta_e = \xi\eta, \tag{2.28}$$

where ξ is the partition coefficient, and

$$\xi \in [0, 1]. \tag{2.29}$$

In our models, ξ decreases linearly from close to 1 in the lithosphere to 0 in the asthenosphere with the increasing temperature, resulting in visco-elastic and viscous

behaviors in the two regions respectively. When ξ is set to 1, the EVSS formulation reverts back to the Maxwell model. The relationship between ξ and T is

$$\xi = \begin{cases} 1 - \frac{T}{T_m}, & \text{if } T \leq T_m; \\ 0, & \text{otherwise,} \end{cases} \tag{2.30}$$

where T_m is the mantle temperature and is set to be 1400 °C.

Numerical implementation

We study the long-term lithosphere and mantle dynamics as governed by a creeping flow in a domain Ω with boundary $\partial\Omega$ using an arbitrary Lagrangian Eulerian (ALE) finite element method (May et al., 2014, 2015). To facilitate large deformations, we use a hybrid spatial discretization ("mesh-marker" discretization) which couples mixed finite elements for the density driving flow problem ($\boldsymbol{u}$, p, T), with a Lagrangian marker-based discretization. The Lagragian markers track constitutive properties and material properties (e.g., plastic strain, density, water content). The domain Ω is partitioned using a structured mesh of hexahedral elements, and the mesh is updated following the evolution of topography. Over each element, we employ mixed $Q_2 - P_1^{disc}$ basis functions for ($\boldsymbol{u}$, p) and Q_1 basis functions for T. Markers are uniformly distributed in each element at the beginning of the simulation, and are updated with the flow velocity during the evolution. Markers can move across elements, and marker population control is performed over an element when it becomes underpopulation or overpopulation. Material properties are first evaluated at markers and then interpolated to mesh nodes or quadrature points.

To track the topography evolution, we solve Eq. (2.20) via operator splitting. We first update the surface mesh with respect to the surface velocity. The time step used to update the surface mesh is equal to the time step for the energy equation, subjected to the additional constraint that the vertical topographic change is smaller than 20 m to avoid topographic oscillation (Kaus et al., 2010). The updated topography, which is on a new surface mesh, is projected back to the surface nodes of the old mesh with Q_1 basis functions. The interior nodes are updated vertically with a distance proportional to the topographic changes of surface nodes above. The proportion decays linearly from 1 at the surface to 0 at the bottom of the domain. In this way, the advection and vertical movement of the topography are accurately recorded on the surface mesh, while the cost for remeshing is restricted (mesh nodes are updated vertically only). The mesh update is handled efficiently through interactions with the parallel PETSc object DMDA (data manager for distributed arrays) (Buschelman

et al., 2017), with which the mesh itself is defined. We then solve the surface diffusion equation on the surface mesh with no-flux boundary conditions. Topographic diffusion is applied to the free surface between time steps and after the topographic update related to subsurface dynamics. After topographyic diffusion, topography increases in the sedimentation region, and sedimentary markers are added into this increased region.

To update the density and water content in the phase assemblages, rock type and total water content are recorded on tracers, and temperature and pressure are obtained from the solutions of the governing equations. Linear interpolation is then used to obtain density and free water content between adjacent nodes of temperature, pressure, and total water content from phase maps for different phase assemblages. Free water is projected to mesh nodes and migrated with the velocity calculated from Eq. (2.21).

To implement the EVSS model, we discretize Eq. (2.24) in time similar to the traditional Maxwell model (Moresi et al., 2002)

$$\frac{\boldsymbol{\tau}_e^{t+\Delta t}}{2\eta_e^{t+\Delta t}} + \frac{1}{2G}\left(\frac{\boldsymbol{\tau}_e^{t+\Delta t} - \boldsymbol{\tau}_e^{t}}{\Delta t} + \boldsymbol{J}(\boldsymbol{u}^t, \boldsymbol{\tau}_e^t)\right) = \dot{\boldsymbol{\varepsilon}}^{t+\Delta t}, \tag{2.31}$$

and then we get

$$\boldsymbol{\tau}_e^{t+\Delta t} = \frac{\Delta t}{\lambda^{t+\Delta t} + \Delta t} 2\eta_e^{t+\Delta t}\dot{\boldsymbol{\varepsilon}}^{t+\Delta t} + \frac{\lambda^{t+\Delta t}}{\lambda^{t+\Delta t} + \Delta t}\boldsymbol{\tau}_e^t - \frac{\lambda^{t+\Delta t}\Delta t}{\lambda^{t+\Delta t} + \Delta t}\boldsymbol{J}(\boldsymbol{u}^t, \boldsymbol{\tau}_e^t), \tag{2.32}$$

where Δt is the time step, and $\lambda^{t+\Delta t}$ is the shear relaxation time ($\frac{\eta_e^{t+\Delta t}}{G}$). We define

$$\eta' = \eta_v^{t+\Delta t} + \frac{\Delta t}{\lambda^{t+\Delta t} + \Delta t}\eta_e^{t+\Delta t}, \tag{2.33}$$

and

$$\boldsymbol{\tau}_e'^t = \frac{\lambda^{t+\Delta t}}{\lambda^{t+\Delta t} + \Delta t}\boldsymbol{\tau}_e^t - \frac{\lambda^{t+\Delta t}\Delta t}{\lambda^{t+\Delta t} + \Delta t}\boldsymbol{J}(\boldsymbol{u}^t, \boldsymbol{\tau}_e^t). \tag{2.34}$$

Substituting the total stress into the momentum equation, we have

$$\nabla \cdot (2\eta'\dot{\boldsymbol{\varepsilon}}^{t+\Delta t}) - \nabla p^{t+\Delta t} = \boldsymbol{f}^{t+\Delta t} - \nabla \cdot \boldsymbol{\tau}_e'^t. \tag{2.35}$$

In this way, by modifying the viscosity and adding another force term, related to the stored stress from previous step into the body force term, our EVSS model is incorporated into the viscous system. The plastic behavior is also influenced by the stored stress, and we simply modify Eq. (2.10) with

$$\eta_y = \min\left(\frac{\max(\tau_y - \sqrt{(\boldsymbol{\tau}_e'^t)_{\mathrm{II}}}, \tau_{ymin})}{2\sqrt{\dot{\varepsilon}_{\mathrm{II}}}}, \eta'\right). \tag{2.36}$$

2.3 Influence of different processes

Previous studies (e.g., Gurnis et al., 1996; Kaus et al., 2010; Fourel et al., 2014; Farrington et al., 2014) often used simplified models to study the influences of different processes on subduction zone evolution, and they may not be suitable for addressing the complex force balance and the interactions between different processes at subduction zones. In this section, we document the influence of different geophysical, petrological, and geochemical characteristics through the systematic comparison of models with different parameters. We focus on the differences in model outcomes, including topography, the deformation pattern in the bending slab, and the stress state within the slab and plates.

Model setup

Due to the large computational cost for multiphysics subduction models with high resolution, we set the model size (length $\times$ width) to 800 km $\times$ 300 km and compare the differences in the early stage of subduction evolution. The initial condition has a plate with a thermal age of 80 Ma (using the half-space cooling model) that subducts below a young plate (thermal age of 20 Ma) with prescribed inflow and outflow at the right side boundary (Fig. 1). The left and bottom boundaries are free slip, while the top is a free surface. The initial topography is calculated from isostasy. A 45° dipping weak zone of 10 km width is set between the two plates to localize the initial deformation, and the weak zone is initialized with plastic strain of random value between 0 and 0.4, while other parameters remain unchanged. A 5 km thick crust with altered basalt and a 15 km thick harzburgite layer below the crust are placed on top of dry pyrolite. Initially, there are no sediments, but are subsequently generated with the surface processes algorithm within the sedimentation region. The finest resolution is 1 km $\times$ 1 km near the subduction zone, and the lowest is 3 km $\times$ 3 km in the asthenosphere. The model setup includes 384 $\times$ 192 elements in total.

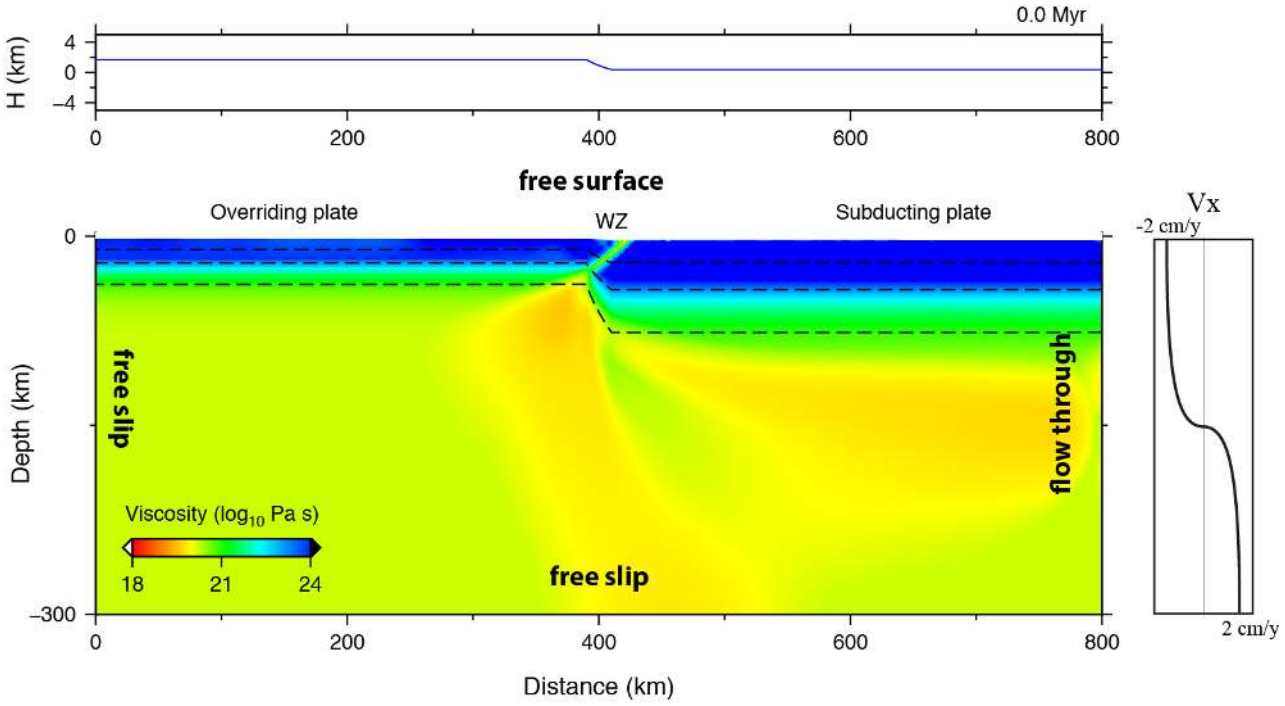

Figure 2.1: Setup for the test model. The initial topography is shown above the model domain and the imposed horizontal velocity is shown to the right. Black dashed lines represent the isotherm of 400 °C, 800 °C and 1200 °C respectively. WZ: weak zone. H: topography.

Free surface vs free slip surface

With evolutionary models, Kaus et al. (2010) compared free surface with free slip surface and show that the upper boundary condition has a significant influence on subduction dynamics. With their set up, the subducting plate can mechanically decouple from the upper boundary only with the incorporation of a free surface. However, they did not compare the changes in the stress state and deformation within plates that generate the final difference in slab morphology. Here, we address this by taking a time evolutionary model with free surface at 10.1 Myr and changing its upper boundary to a free slip surface for comparison (Fig. 2.2). During the boundary change, we keep materials below the trench depth and remove materials above that depth. In this way, only the surface geometry of the model is changed to be compatible with the free slip surface (topography removed), while the deep structure and material properties are kept constant. A new Stokes solve is then computed with the free slip surface to obtain the stress and deformation and the instantaneous topography with the surface normal stress. We use this comparison to

show how changes of surface geometry from free to free slip surface influence the stress state and deformation within plates, and to study the difference between the free surface topography and the stress-derived topography using a free slip surface.

For the free surface case (Fig. 2.2a), at 10.1 Myr, the subducted slab reaches ~170 km depth and is under extension due to its own negative buoyancy, although not sufficiently large to dominate the dynamics of the system, so that the system is controlled by the boundary push and the bending of the subducting plate. The bending of the subducting plate causes near-surface extension and deep compression of the lithosphere near the trench, as indicated by the plate perpendicular maximum principal stress in the upper part of the lithosphere and the along plate maximum principal stress in the lower part of the lithosphere. With bending, the subducting plate yields strongly in the extensional region near the surface and moderately in the compression region near the bottom of the lithosphere as shown with the reduced effective viscosities. Most of the overriding plate is in a nearly neutral stress state, while the overriding plate near the subduction interface is under compression. The trench depth is 4 km, and the fore bulge height at ~ 540 km distance is ~ 100 m.

Comparing the free slip surface case (Fig. 2.2b) to the free surface case (Fig. 2.2a), in the asthenosphere, the two cases are identical, but the near surface stress, deformation and topography have similaries and differences. The general patterns of the stress state and deformation in the plates of the two cases are similar, with some subtle differences. With a free slip surface, the compression in the subducting plate near the right boundary is smaller than in the free surface case, and, near the trench, the extensional area is divided into two parts with a kink in the maximum principal stress orientation at the trench, while the maximum principal stress orientation varies continuously in the this region with a free surface. Yielding within the bending region is limited to a narrower zone close to the subduction interface with the free slip surface, and the change in the yielding pattern occurs near the trench position. It is obvious that the change of the surface curvature on the subducting plate near the trench strongly influence the stress state and deformation at the bending region, and, with free slip surface, the transition of the stress and deformation near the surface are not as smooth as with a free surface. Topographic outcomes from the two cases are similar, e.g., position of trench and fore bulge and higher overriding plate than the subducting plate, but the relief is much larger with the free slip surface than with the free surface (~ 4× larger for trench depth and ~ 10× larger for the fore bulge height), and the free slip surface case shows more topographic variations, e.g.,

the depression on the overriding plate close to trench (at 320 km distance) and the depression near the right boundary, and some sharp topographical structures, e.g., the trench and the narrow peak at ~ 370 km distance.

To further investigate the origin of the large topographic variations with free slip, we reduced the maximum viscosity cutoffs (Fig. 2.2b and 2.S1). The topographic variations decrease with smaller plate viscosity, and with a weaker lithosphere, the topography approaches that of the free surface case (Fig. 2.3). Nevertheless, substantial differences between topography from free slip and free surface remain.

In addition, we conducted a time evolutionary case with free slip surface and starting at 0 Myr. We also found that the subducting plate cannot mechanically decouple from the upper boundary.

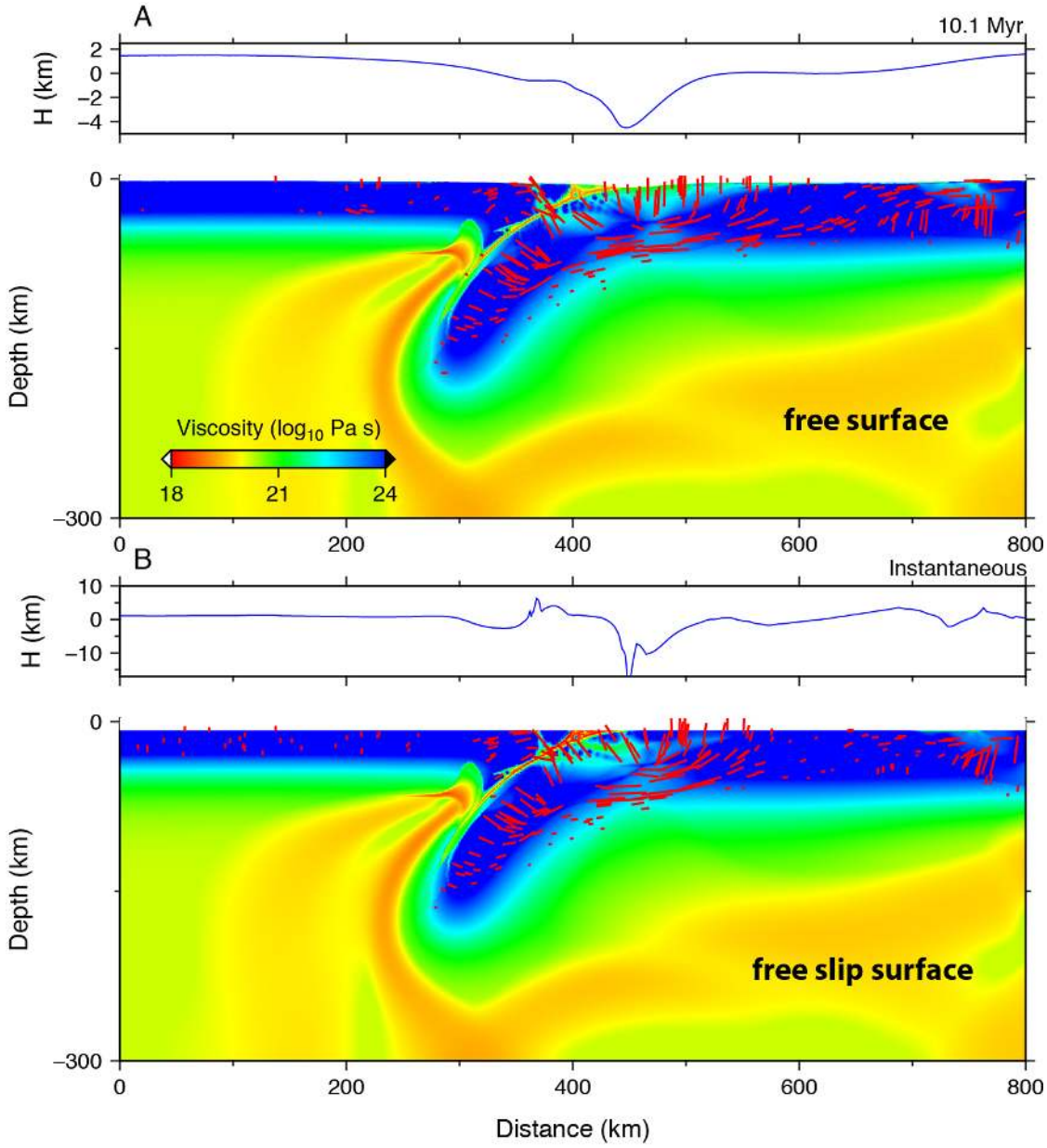

Figure 2.2: Comparison between (a) free surface and (b) free slip surface. Red lines show the direction and magnitude of the maximum principal stress. H is topography.

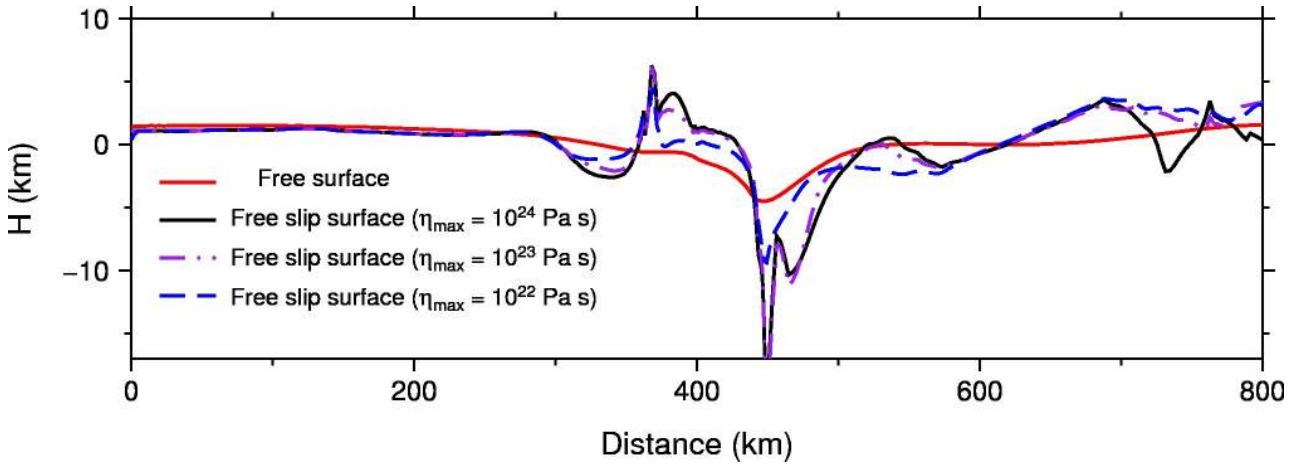

Figure 2.3: Topography comparison between free surface and free slip surface models at 10.1 Myr. H is topography.

Surface processes

Surface processes, i.e., erosion and sedimentation, are thought to influence the lithosphere and mantle dynamics mainly through redistributing surface loads (topography) (Avouac and Burov, 1996; Burov and Toussaint, 2007). In addition, subduction of weak and water rich sediments generated by surface processes could play some role in lubricating the subduction interface (Lamb, 2006). Here, we focus on how different sedimentation and erosion rates affect the dynamics of the system and model predictions through topographic changes while controlling the amount of weak material near the trench.

Surface diffusion influences the wavelength of topography and the amount of weak material near the trench. We vary the surface diffusion coefficient, κ_s, from 1×10^3 m^2/yr to 4×10^3 m^2/yr (Burov and Toussaint, 2007). With increasing erosion and sedimentation rates, the wavelength of the topography increases, the trench depth shallows, the size of the weak prism increases, and the yielding area on the subducting plate at the bending region widens slightly (Fig. 2.4, Fig. 2.S2 and Fig. 2.S3). Topography is controlled by two competing mechanisms: the deeper lithosphere and mantle dynamics that builds topographic variations and the surface processes that smoothen the variations. With larger diffusivity, there is more erosion and in turn more sediment, which leads to smoother topography with longer topographic wavelength and shallower trench depth. The averaged horizontal stress within the overriding plate is an indicator of the interaction between two plates. Initially, the stress levels within the overriding plate are similar for all four cases

(2 Myr), while larger κ_s leads to faster release of stress when the fault starts to decouple the plates (6 Myr) (Fig. 2.5a and Fig. 2.5b). However, when the fault matures, the averaged horizontal stress within the overriding plate is much higher for the case with the smallest κ_s. This indicates that κ_s influences plate coupling on the subduction interface and a transition in the plate coupling happens after some critical value of κ_s is reached. This transition in the plate coupling is likely caused by the amount of weak material near the trench as suggested by the change in the size of the weak prism (Fig. 2.4 and Fig. 2.S2). The change in yielding of the hinge zone is likely to be influenced by both the plate coupling at the subduction interface and surface curvature of the bending plate which are both adjusted by surface processes.

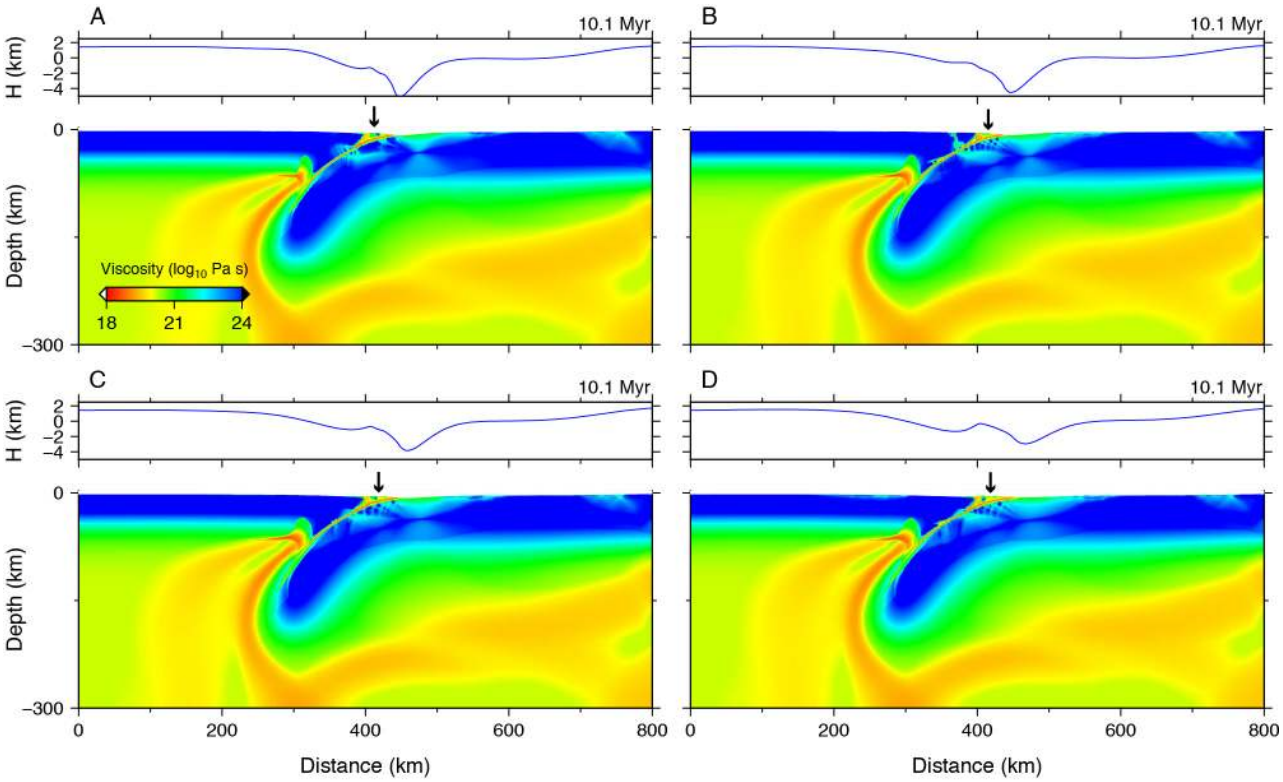

Figure 2.4: Comparison among models with increasing surface diffusion coefficient (a) 1×10^3 m^2/yr, (b) 2×10^3 m^2/yr (reference model), (c) 3×10^3 m^2/yr, and (d) 4×10^3 m^2/yr. H is topography. The black arrow shows the position of the weak prism. Zoom ins of the weak prism are shown in Fig. S2.3.

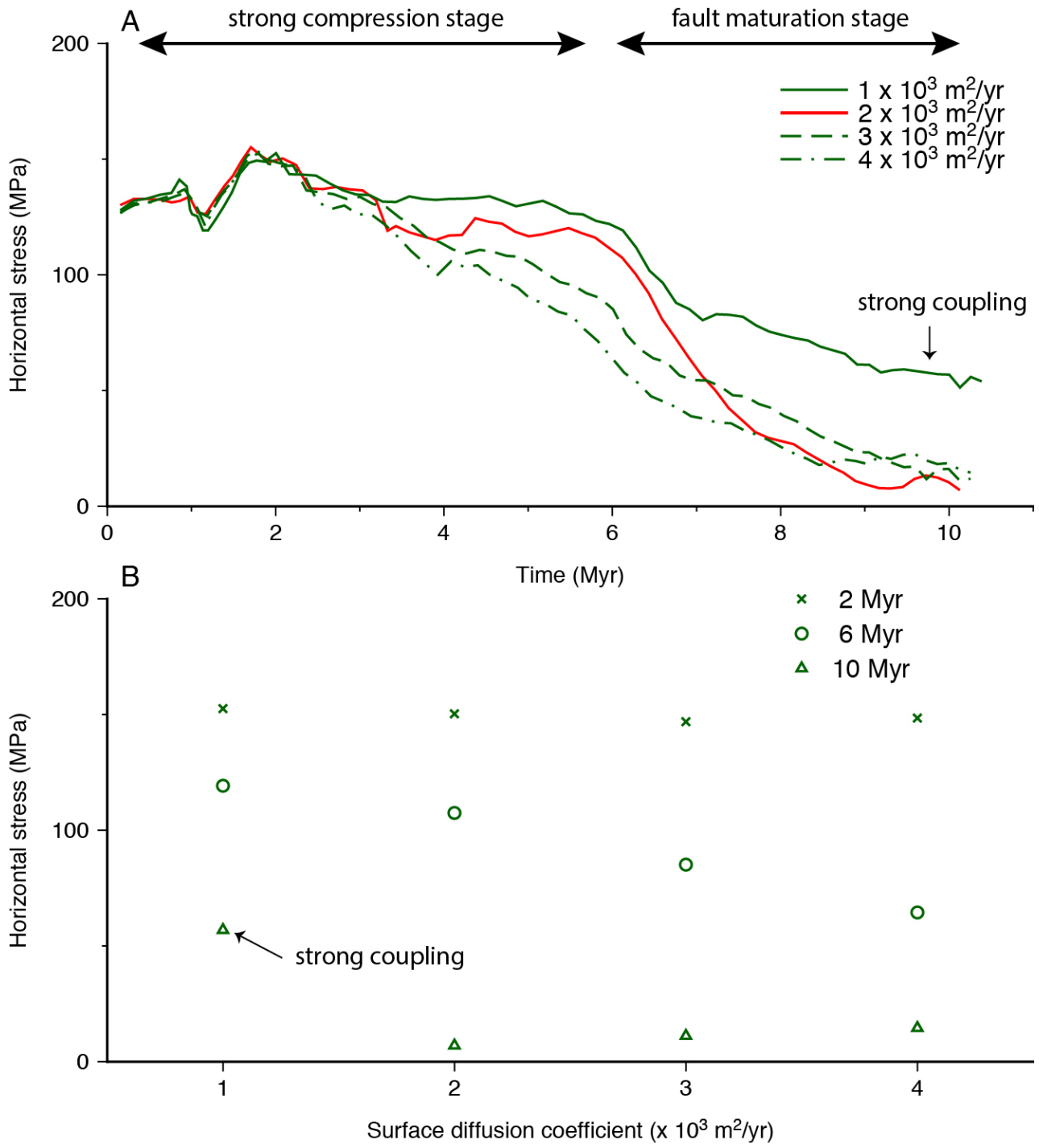

Figure 2.5: Averaged horizontal stresses within the overriding plate with different surface diffusion coefficients. (a) Stress evolution. (b) Stress vs surface diffusion coefficients. The averaging is performed within the region that spans from 100 km to 300 km distance with reference to the left side boundary and surface to 40 km depth.

Subduction of sediments and oceanic crust

Subduction of sediments and oceanic crust is important for several reasons. The subduction interface is generally thought to be composed of sediments and oceanic crust, and their strength and rheology influence plate coupling (Bebout, 2007). Fluids released from subducted sediments and oceanic crust reduce the frictional strength on the subduction interface through increasing pore pressure and weaken the mantle wedge (Kodaira et al., 2004; Audet et al., 2009). Subduction of sediments and oceanic crust also contributes to the geochemical heterogeneity of the deeper mantle (Hofmann and White, 1982). Here, we test the influence of the subduction of sediments and oceanic crust on plate coupling, the deformation on the subducting plate, and the weakening of the mantle wedge.

We first test a case without sediments (Fig. 2.6b and Fig. 2.S4b). The generated sediments during the surface processes near the upper boundary are replaced with weakened oceanic crust (with the rheology of plagioclase instead of quartz and less water content). Comparing the case without sediments (Fig. 2.6b) to the reference case (Fig. 2.6a), we do not observe obvious changes in the topography, intra-plate deformation, and the weakening in the mantle wedge. The stress evolutions on the overriding plate are also very similar (Fig. 2.7). The case without sediments suggests that the differences in rheology and water content between weakened oceanic crust and sediments do not seem to substantially influence the dynamics of the system, and weakened oceanic crust and sediments may have similar effects on lubricating the subduction interface. The weakening in the mantle wedge is not influenced by the removing of sediments since the weakening is dominated by water released from the crust, while sediments dehydrate mostly at shallower depths (before reaching the mantle wedge) (Fig. 2.S4). We then test another case without sediments or oceanic crust (Fig. 2.6c). In this case, only pyrolite is incorporated in the model. Comparing the case without sediments or crust (Fig. 2.6c) to the reference case (Fig. 2.6a) and the case without sediments (Fig. 2.6b), this case has a deeper trench depth and a further topographic depression on the overriding plate (300 km from the trench), and the yielding area is much narrower at the bending region than the other two cases. The case without sediments or crust has the largest average horizontal stress within the overriding plate during the fault maturation stage among all models (Fig. 2.6), which suggests that without the lubrication of sediments or crust, subducting and overriding plate remain strongly coupled. We test one more case by turning off the water weakening effect while keeping other parameters unchanged to test the influence plate coupling at the mantle wedge (Fig. 2.6d). With additional

coupling in the mantle wedge between two plates, the topographic depression on the overriding plate close to trench deepens (Fig. 2.6d), and the stress on the overriding plate increases (Fig. 2.7), while the differences are not large. However, we will show that water weakening initiates failure of the overriding plate with a full subduction zone model (Section 2.4).

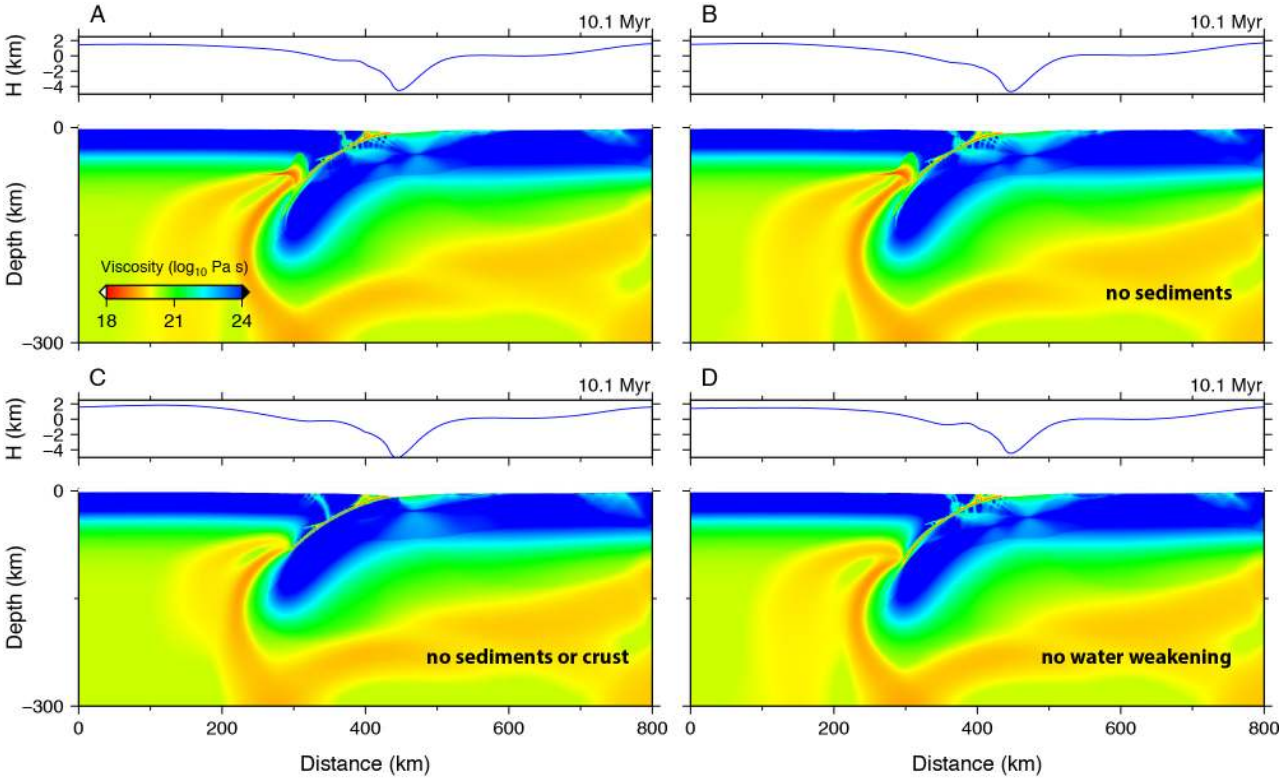

Figure 2.6: Comparison among (a) reference model, (b) model without sediments, (c) model without sediments or crust, and (d) model without water weakening. H is topography.

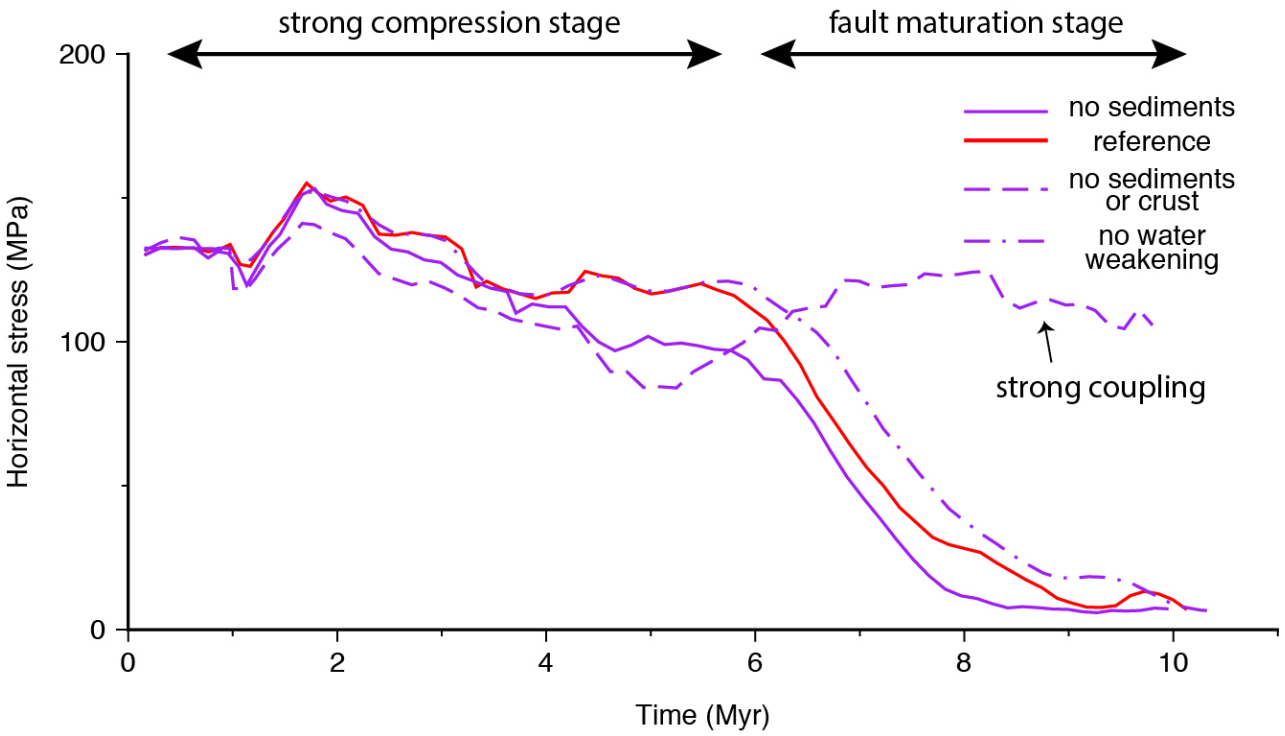

Figure 2.7: Averaged horizontal stresses within the overriding plate for cases related to sediments and crust. The averaging is performed within the region that spans from 100 km to 300 km distance with reference to the left side boundary and surface to 40 km depth.

Elasticity

The influence of elasticity on subduction zone evolution has been addressed previously, especially during the bending and unbending processes, with free subduction models (Capitanio et al., 2007; Fourel et al., 2014; Farrington et al., 2014). These models ignore the overriding plate and usually employ constant viscosity for the slab and mantle. However, these simplified models may not be compatible terrestrial subduction. Here, we compare two subduction zone models with or without elasticity to test the influence of elasticity on subduction zone evolution.

Comparing the case without elasticity (Fig. 2.8b) to the case with elasticity (Fig. 2.8a), the slab dips are almost the same after 10 Myr of convergence. The predicted topography profiles are similar except that there is a mild depression on the overriding plate close to trench (370 km in board) in the case with elasticity and is absent in the case without elasticity. However, deformation and strain localization on the subducting plate within the bending region (Fig. 2.8) and the stress level within

the overriding plate during compression are quite different (Fig. 2.9) between these two cases. Without elasticity, yielding within the extensional region during bending occurs within a relatively narrow zone near the trench, and no localized shear bands on the subducting plate have formed. With elasticity, stored stress within the bending region bring the subducting lithosphere closer to yield surface, and yielding extends to a much wider area in both directions away from the trench than the case without elasticity. Compression between the subducting plate and the overriding plate across the subduction interface is slightly stronger than the case without elasticity due to the unbending, which causes yieldings on both plates and gives rise to the formation of the mild topographic depression at 370 km distance. However, due to the existence of the overriding plate, the unbending process does not lead to appreciable shallowing of slab dip. This comparison implies that elasticity dose not affects the slab dip angle much in the presence of the overriding plate and plasticity. Its importance may lie in changing the stress level of the plates during the compression, and the deformation pattern and generating localized shear bands within the hinge zone.

We carry out two additional cases with different reference plastic strains (controling the weakening rate of yield stress). With a lower reference plastic strain ($\varepsilon_0 = 0.2$) (Fig. 2.8c), the stress within the overriding plate decreases faster than the reference case, and more localized shear bands develop on the subducting plate. With a higher reference plastic strain ($\varepsilon_0 = 0.6$) (Fig. 2.8d), yielding area on the subducting plate becomes narrower, and less localized shear bands develop than in the reference case. The plate coupling of the case with slow strain weakening when fault matures is much stronger than the other 3 cases. These two additional cases confirm that the generation of the localized shear bands is related to plastic parameters but is controlled by the interaction between elasticity and plasticity.

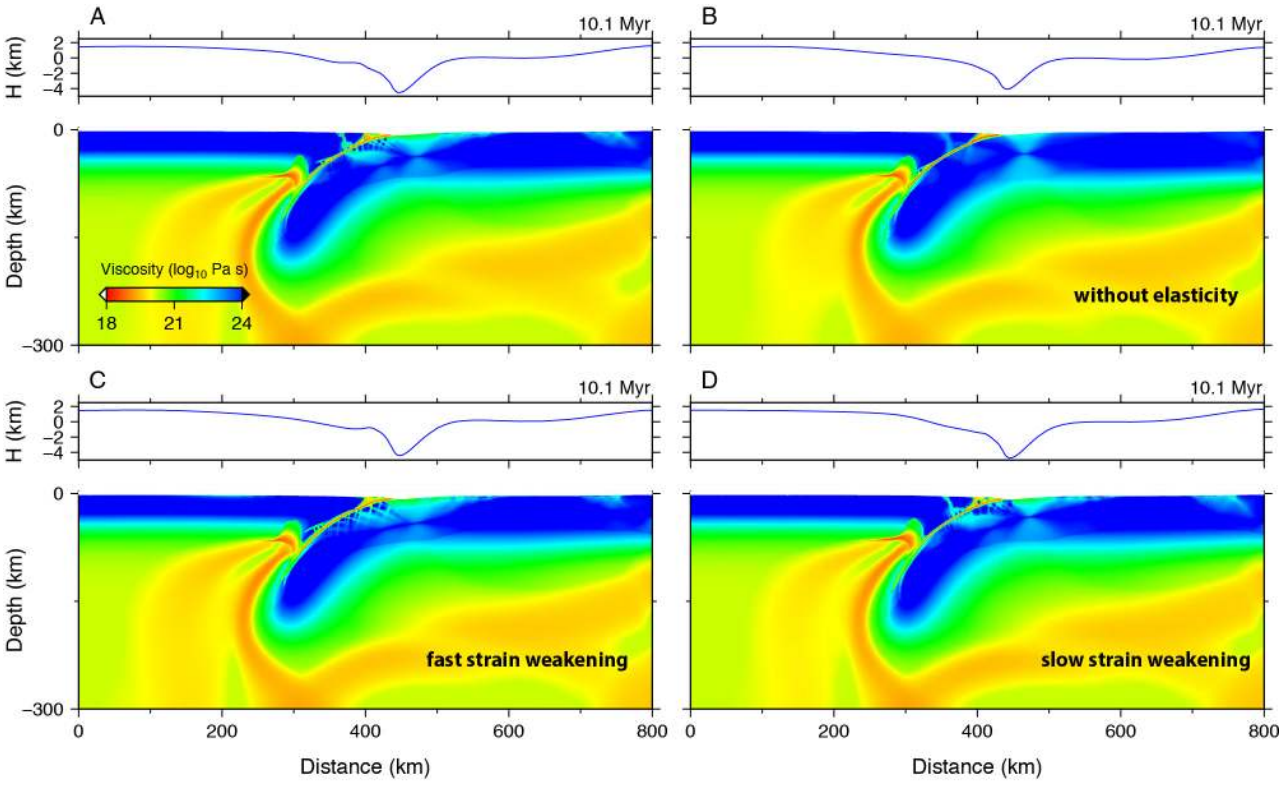

Figure 2.8: Comparison between (a) the reference, (b) without elasticity, (c) fast strain weakening, and (d) slow strain weakening. H is topography.

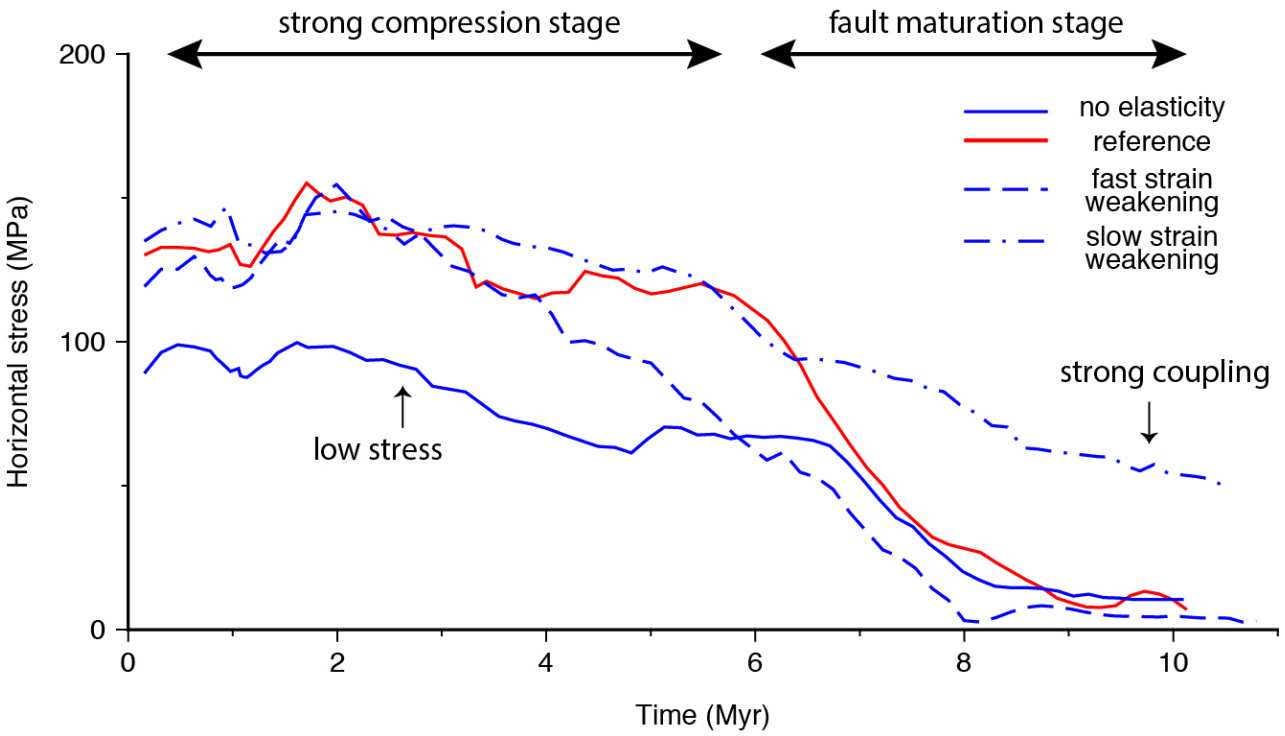

Figure 2.9: Averaged horizontal stresses within the overriding plate for cases related to elasticity and plasticity. The averaging is performed within the region that spans from 100 km to 300 km distance with reference to the left side boundary and surface to 40 km depth.

2.4 The New Hebrides Subduction Zone

We now turn our attention to a full subduction zone model, which generates self-consistent slab detachment during the early stage of subduction zone evolution for a young subducting plate connected to a large plate. The impact of the detached slab on the lower mantle causes strong deformation within the slab segment, which provides a possible context to understand the origin of the isolated deep earthquakes beneath the North Fiji Basin. We use the transition from strong to weak deformation in the detached slab with depth to explain the cause of the difference in seismic intensities between the northern and the southern deep earthquake clusters (Fig. 2.10). The model also produces other important outcomes, including overriding plate failure, back-arc spreading, and trench retreat. Topographic evolution is a constraint on the internal lithosphere and mantle dynamics.

Isolated deep earthquakes and motivation

Substantial seismicity near the bottom of the transition zone and isolated from active subduction occurs beneath the North Fiji Basin (Fig. 2.10a and 2.10b). These earthquakes can be divided into two clusters: a northern cluster has a high level of seismicity at the base of the transition zone and is clearly seperated from the shallow dipping Benioff zone; there is also a detached southern cluster which detached from both the northern cluster and the shallow slab, but is more poorly defined because there are much less earthquakes there. The deformation geometries revealed by the focal mechanisms of these earthquakes are complex (Okal and Kirby, 1998). These isolated deep earthquakes are interpreted to be within detached slab segments which might have originated from either the extinct Vitiaz subduction zone to the northeast (which had southward vergeing subducting from the Pacific Plate) or the New Hebrides Subduction Zone to the southwest (Hamburger and Isacks, 1987; Okal and Kirby, 1998; Richards et al., 2011). Three interesting questions were raised for these isolated deep earthquakes in detached slab segments: (1) where did these slab segments actually come from? (2) what triggers these deep earthquakes within the detached slab segments? (3) what causes the difference in the seismic intensities between the northern and the southern clusters? If the detached slab segments originated from the extinct Vitiaz Subduction Zone then they should be trapped within the transition zone for a long time and stagnant with little active deformation (Mann and Taira, 2004). On the other hand, if they were from the New Hebrides Subduction Zone then the question as to what caused slab detachment for this young subduction zone, while most previous studies suggest that slab detachment usually happens during subduction termination (e.g., Gerya et al., 2004; Andrews and Billen, 2009). Phase transformations related to metastable peridotite in the cold slab material are used to explain the seismicity in detached stagnant slab segments (Okal and Kirby, 1998), while this theory alone cannot account for the intensity difference if both clusters were related to detached slab segments (Richards et al., 2011). Reactivation of preexisting weak structures under deformation is another possible mechanism for deep earthquakes (e.g., Jiao et al., 2000), while it was not considered as a plausible explanation for these isolated deep earthquakes since it is not clear what drives the deformation in these detached slab segments.

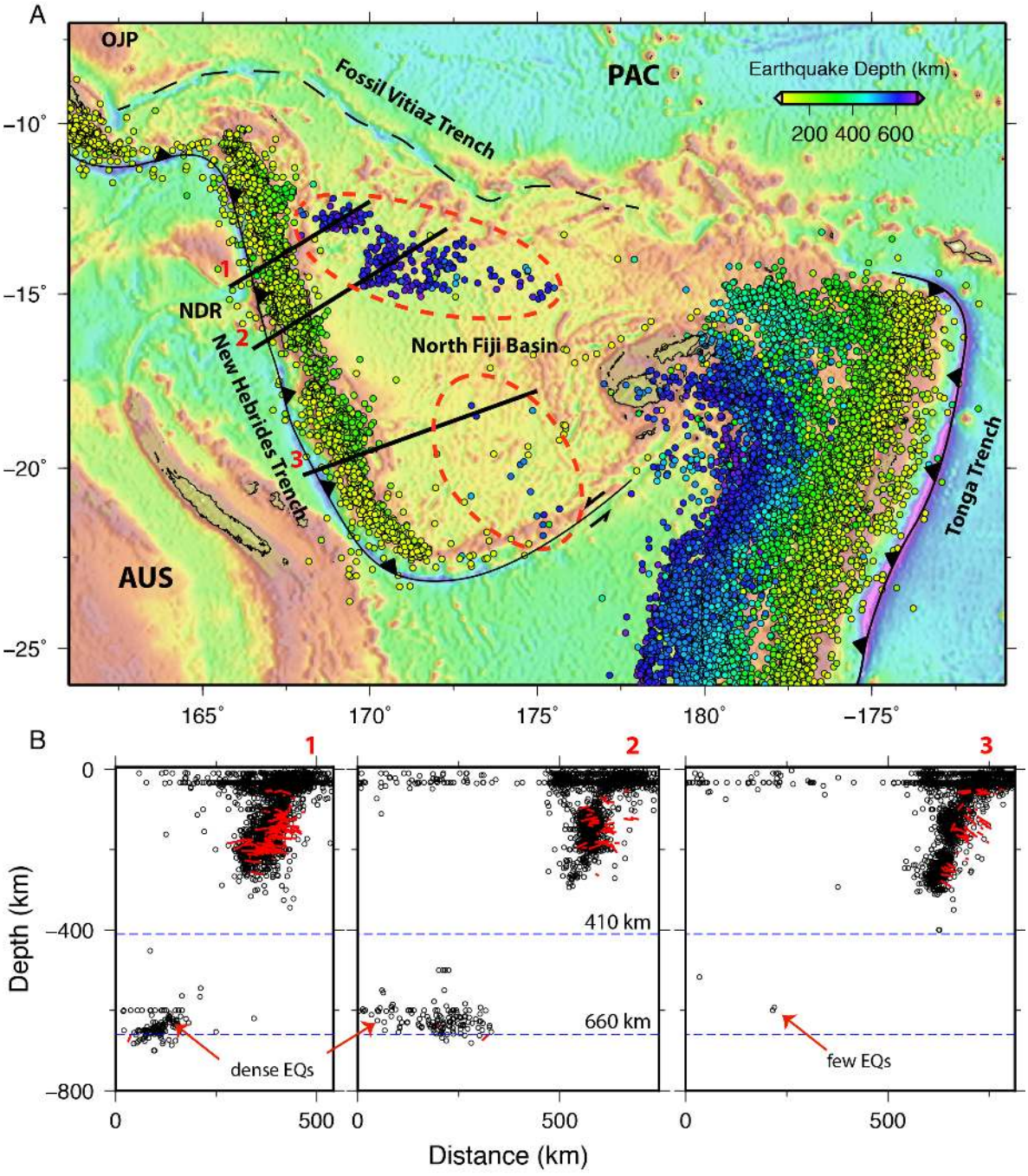

Figure 2.10: (a) Intermediate and deep earthquake distribution of the New Hebrides Trench and the Tonga Trench region. The two red dashed circles show the northern and the southern clusters of isolated deep earthquakes in the transition zone, respectively. AUS: Australia Plate; NDR: North D'Entrecasteaux Ridge; OJP: Ontong Java Plateau; PAC: Pacific Plate. (b) Cross-sections of vertical earthquake distribution. Red bars show the focal mechanisms. Surface positions of these three cross-sections correspond to the three thickened black lines in (a) from north to south. Earthquake location data are from ISC Bulletin (International Seismological Centre, 2014), and the focal mechanism solutions are form CMT catalog (Dziewonski et al., 1981).

Model description

The model consists of an old plate with a thermal age of 40 Ma subducting below a younger plate (thermal age of 10 Ma) under imposed velocity (Fig. 2.11). The imposed velocity influences the dynanics in different ways at early and later stages of the model evolution. The imposed velocity first provides the driving force needed for the convergence of the two plates during subduction initiation which is defined as a stage that the negative buoyancy of the subducted slab is insufficient to drive the convergence (Gurnis et al., 2004). The actual driving force for the initiation of the New Hebrides Subduction Zone might come from the collision of the Ontong Java Plateau and the Solomon Island Arc which started as early as ~ 20 Ma and caused subduction polarity reversal for several adjacent subduction zones including the extinct Vitiaz Subduction Zone (Mann and Taira, 2004). After subduction is initiated, the imposed velocity tends to hold back the subducted slab from sinking too fast into the mantle and consequently contribute to the back-arc spreading and the trench retreat, consistent with the initiation of the Izu-Bonin-Mariana subduction zone (Leng and Gurnis, 2011). In the case of IBM, only a fraction of the overall force on the rather large Pacific was modified. Here, we think that this holding back mechanism is also applicable considering that the size of New Hebrides subduction zone is far smaller compared to the size of the Australia Plate and the plate motion of the Australia Plate was not strongly influenced by the initiation of the New Hebrides subduction zone. A constant value for the imposed velocity is used here to avoid the influence of the imposed velocity change on the morphology of the slab. We set the imposed velocity to 2 cm/yr since this value results a similar time span of ~ 20 Myr for the model evolution from the initial compression.

Prescribed inflow and outflow velocity boundary conditions are frequently used in regional geodynamic models to provide the driving force and to conserve the model volume (or mass) at the same time, while the prescribed outflow at the deeper parts of side boundaries or at the bottom boundary could produce artifacts on the slab morphology. To avoid prescribed outflow, we applied the imposed velocity within the lithosphere on the subducting plate 600 km from the right boundary and introduced a ridge (thermal age of 0 Ma) at the right end of the model to decouple the subducting plate from the right side boundary. Free slip boundary condition is used at the side and the bottom boundaries, and true free surface boundary condition is applied on the upper boundary. For simplicity, we use a 45° dipping weak zone of 10 km width between two plates to localize the initial deformation. The initial weak zone is initialized with random plastic strain between 0 and 0.4, 1000 km

away from the left boundary and 900 km from the imposed velocity. Other than the initial weak zone, we do not incorporate any other heterogeneities. A 5 km thick crust with altered basalt and a 15 km thick harzburgite layer below the crust are placed on the top of dry pyrolite. Two viscosity discontinuities are introduced at the 410 km depth and 660 km depth respectively, where the rheology in the lower mantle is Newtonian (linear viscosity) and the rheology in the transition zone is non-Newtonian and similar to the upper part but about 5 times larger (e.g., Li et al., 2017). Resolution within the red box (Fig. 2.11) is highest and is 1 km x 1 km, and the lowest resolution in the transition zone and lower mantle is 3 km x 3 km. The model has 1024×512 elements in total.

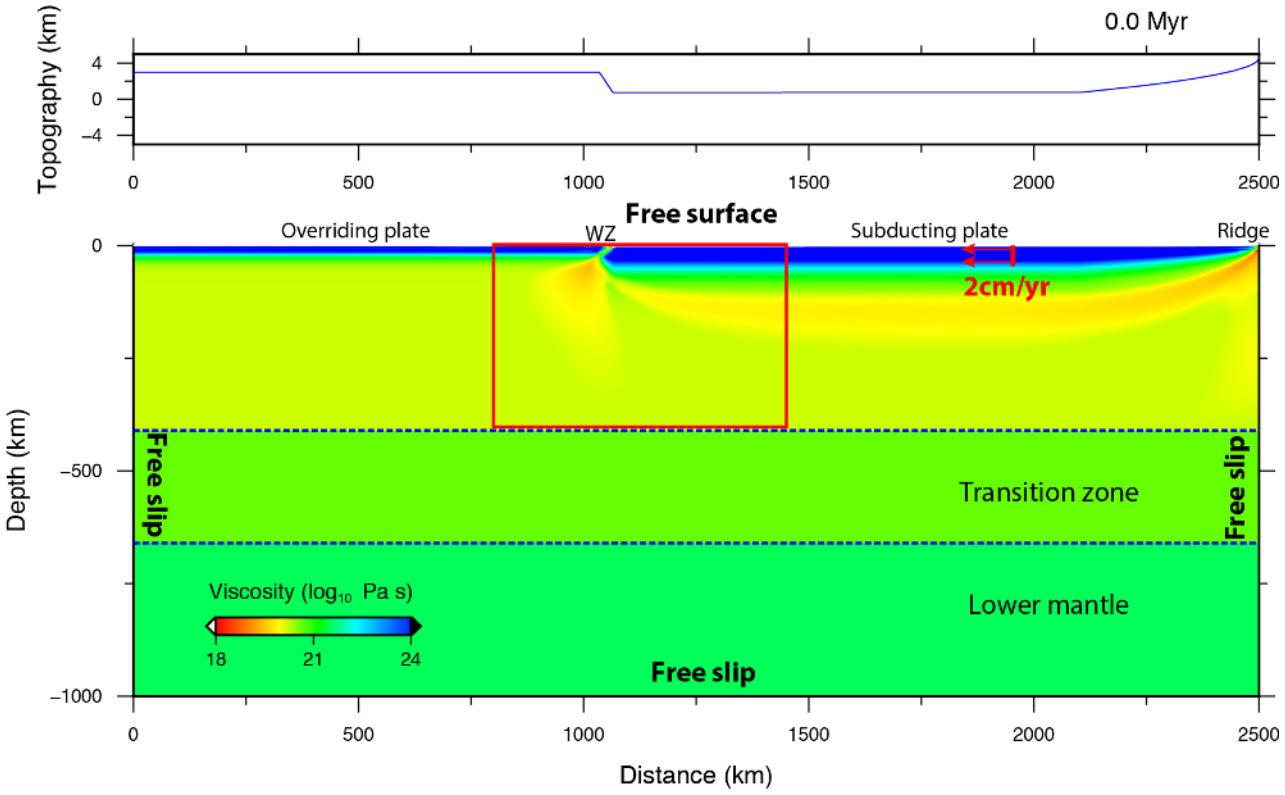

Figure 2.11: Model setup for the New Hebrides Subduction Zone. The red bar shows the position of the imposed velocity and the red arrows show the direction. The red box shows the regional refined region (with resolution 1 km x 1 km). WZ: weak zone.

Results

Overview of the model evolution

Here, we briefly introduce the evolution of the model, while we address important phenomena and their tectonic and geophysical implications. During subduction initiation (before 10.2 Myr), the system is dominated by two processes, development of the localized decoupling zone (subduction interface) and the accumulation of the negative buoyancy of the subducted slab (Fig. 2.12). By 2.1 Myr, resistance from the bending of the subducting plate and smoothing of the immature subduction interface causes strong compression within both overriding and subducting plates. Buckling of the lithosphere, manifested as topographic fluctuations of ~ 100 m at the surface (Fig. 2.13) and similar distance-separated yielding regions within the lithosphere (Fig. 2.12), occur on both plates, while the buckling is more obvious on the overriding plate and its wavelength is much shorter compared the subducting plate due to its younger thermal age. An antisymmetric topographic structure with uplift on the overriding plate close to the trench and depression at the trench, a transient feature for subduction initiation under compression, shows up with a amplitude of ~ 2 km (Fig. 2.13).

With the maturation of the subduction interface and the accumulation of the negative buoyancy on the subducted slab (by 10.2 Myr), compression fades, and extension resulted from the hanging subducted slab starts to dominate the dynamics of the system. The buckling in the lithosphere disappears, and the uplifted topography on the overriding plate close to trench releases. Pervasive normal faults develop in the upper part of the subducting lithosphere (the bending hinge zone, Fig. 2.12 and fine structure in Fig. 2.14). Such faults are weak structures that enter the mantle following subduction and could be reactivated under proper situations. Water released from the subducting slab raises up and weakens the mantle wedge and the overriding plate, which contributes to the localization of deformation in the overriding plate (Fig. 2.12 and Fig. 2.14). Trench depth increases due to the increasing negative buoyancy on the hanging slab (before the slab reaches the lower mantle, Fig. 2.13). By 15 Myr, more negative buoyancy accumulates on the hanging slab, which adds strong extensional forces to the subducting and overriding plates. Together with the constraint applied on the subducting plate by the imposed velocity and the developed weak structures on both the overriding and subducting plates around the trench region, both plates stretch regionally, which leads to the failure of the overriding plate and the formation of a localized weak zone penetrating through the subducting

slab (Fig. 2.12 and Fig. 2.14). The trench depth reaches its maximum value (~ 5 km), and a regional depression is found at the failure point on the overriding plate with slightly uplifted edges (Fig. 2.13). Upwelling in the asthenosphere is not yet developed beneath the failure region of the overriding plate.

With further extension (by 16 Myr), a slab segment of ~ 250 km length detaches from the subducting plate along the localized weak zone, and the failure of the overriding plate further develops (Fig. 2.12 and Fig. 2.14). Responding to the reduction of negative buoyancy, the trench depth shallows rapidly (Fig. 2.13). By 17 Myr, the detached slab segment sinks freely into the deeper part of the mantle and tilts clockwise slightly (Fig. 2.12). As a consequence of slab detachment, the trench depth becomes as shallow as ~ 2 km and an ~ 2 km uplift is also found in the forearc region. Upwelling in the asthenosphere beneath the failure region of the overriding plate causes an elevated topography (Fig. 2.13). The back-arc region starts to spread and the trench retreats (Fig. 2.12). By 18.1 Myr, the detached slab segment hits the upper surface of the lower mantle, which results in a strong deformation within the detached slab segment (Fig. 2.12 and Fig. 2.15). With the increasing of the negative buoyancy on the subducting slab, the trench depth is deepening again (Fig. 2.13). By 20.6 Myr, the sinking velocity of the detached slab segment becomes small, and the deformation within it almost vanishes (Fig. 2.15). Near the surface, the rate of the back-arc spreading and the trench retreat increases substantially with the fast subduction of a continuous slab (Fig. 2.12 and Fig. 2.16). Due to the large negative buoyancy on the subducting slab, the trench depth reaches as deep as ~ 5 km again (Fig. 2.13).

Trench position as a function of time is shown in Figure S2.6. Before the failure of the overriding plate (~ 15 Myr), trench advances slowly (with a velocity of ~ 0.1 cm/yr) under the imposed driving velocity. After the failure of the overriding plate, the trench retreats with a velocity of ~ 4 cm/yr and results in an ~ 200 km total retreating (by 20.6 Myr).

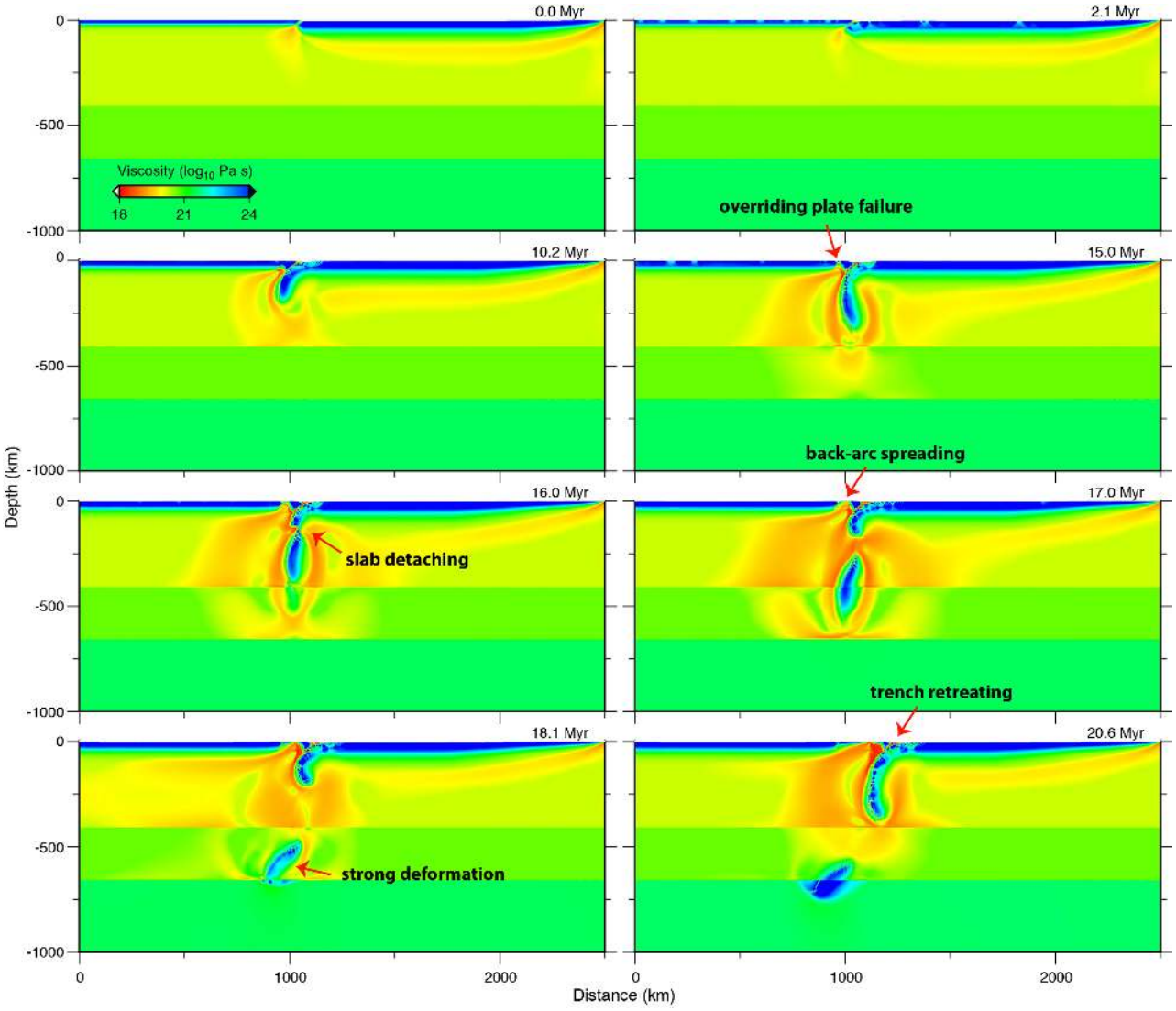

Figure 2.12: Model evolution shown with the effective viscosity.

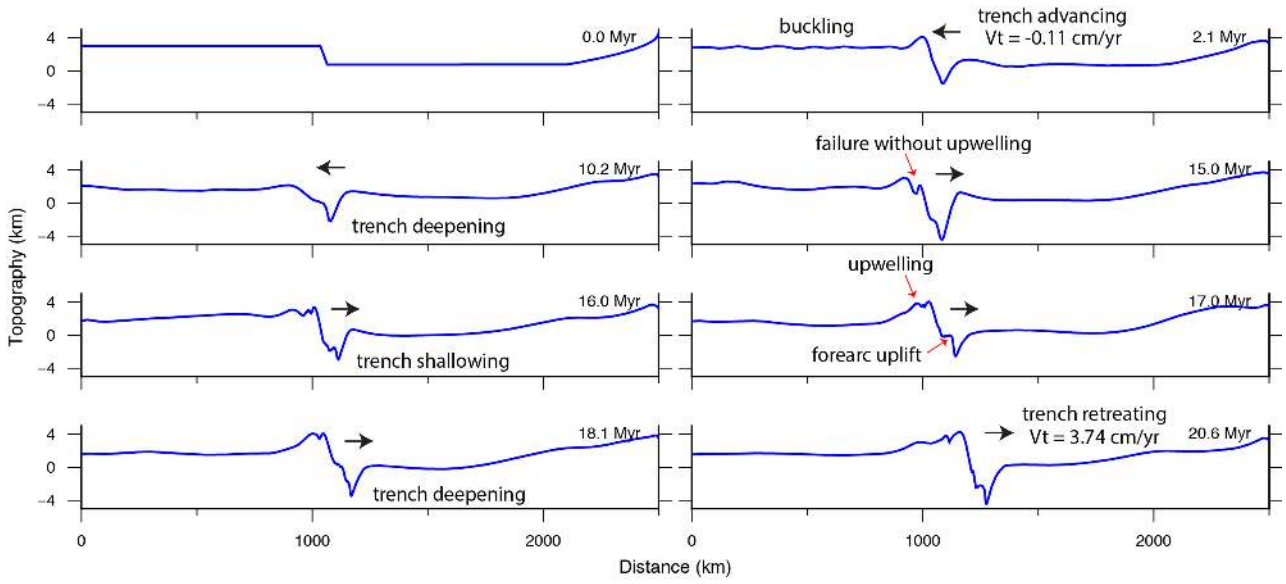

Figure 2.13: Topography evolution for the eight times shown in Figure 2.12 and labelled with a key outcome. Black arrows show the motion of the trench, and Vt is the average velocity of trench migration.

Overriding plate failure and slab detachment

Failure of the overriding plate is a prelude to back-arc spreading and may be facilitated from the water weakening in the mantle wedge and the adjacent lithosphere. Due to the nonlinearity in viscosity (shear thinning), the positive feedback between viscosity reduction and strain localization, the weakening effects of water are amplified. A 10× to 100× viscosity reduction is observed in the water weakening region in the lithosphere directly above the mantle wedge (Fig. 2.14a). The water weakening does not directly break the overriding plate, but leads to the concentration of deformation there. After the tip of the slab passes the 200 km depth (by 12 Myr), the large negative buoyancy on the slab pulls the overriding plate trench-wards, resulting in a large shear band connecting the water weakened region at the bottom of the lithosphere to the surface. At this stage, deformation on the overriding plate is largely concentrated within this shear band, but is not yet localized on faults (Fig. 2.14 a and b). With further extension (by 14 Myr), localized normal faults begin to appear near the edges of the shear band (Fig. 2.14 a and b), and deformation is much more localized on the normal faults. Coupled with the onset of the relative motion on the normal faults near the edges of the shear band, thinning of the lithosphere begins (Fig. 2.14a and b). With continuous extension (by 16 Myr), the overriding

plate eventually fails and leaves a ductile mantle in the deeper part of the original lithosphere and a brittle and weakly connected thin lithosphere near the surface with multiple pairs of active normal faults offsetting the extension (Fig. 2.14 a and b). Although water weakening contributes to the initiation of overriding plate failure, during the development of the failure, the breaking center migrates back to the overriding plate side (with respect to the trench), and at the time the overriding plate spreads, the spreading center is at the back-arc region.

During the evolution of the slab it detaches. After the subduction initiation and before the negative buoyancy on the subducted slab is too large (by 10.2 Myr), deformation on the subducting plate near the trench is mainly controlled by the bending of the plate. The characteristic stress state of plate bending with near-surface extension and compression at deeper part causes the development of pervasive normal faults at the bending region which move downward (Fig. 2.14). As long as the regional stress is below the yield strength on these weak structures, they remain inactive (as marked in Figure 2.14 at 12 Myr). By 14 Myr, with failure of the overriding plate not being well established and plate convergence being controlled by the imposed velocity of the subducting plate, the large volume of the hanging subducted slab causes strong extensional stress within the slab, and some weak structures within begin to reactivate, leading to the elongation of the slab (Fig. 2.14 a and b). By 15 Myr, strain localizes on a lithospheric-scale weak zone within the hanging slab at $\sim$ 100 km depth, and the weak zone develops by reactivation of one these subducted weak structures. Quickly, within 1 Myr (by 16 Myr), the deeper part of the slab detaches along the localized weak zone.

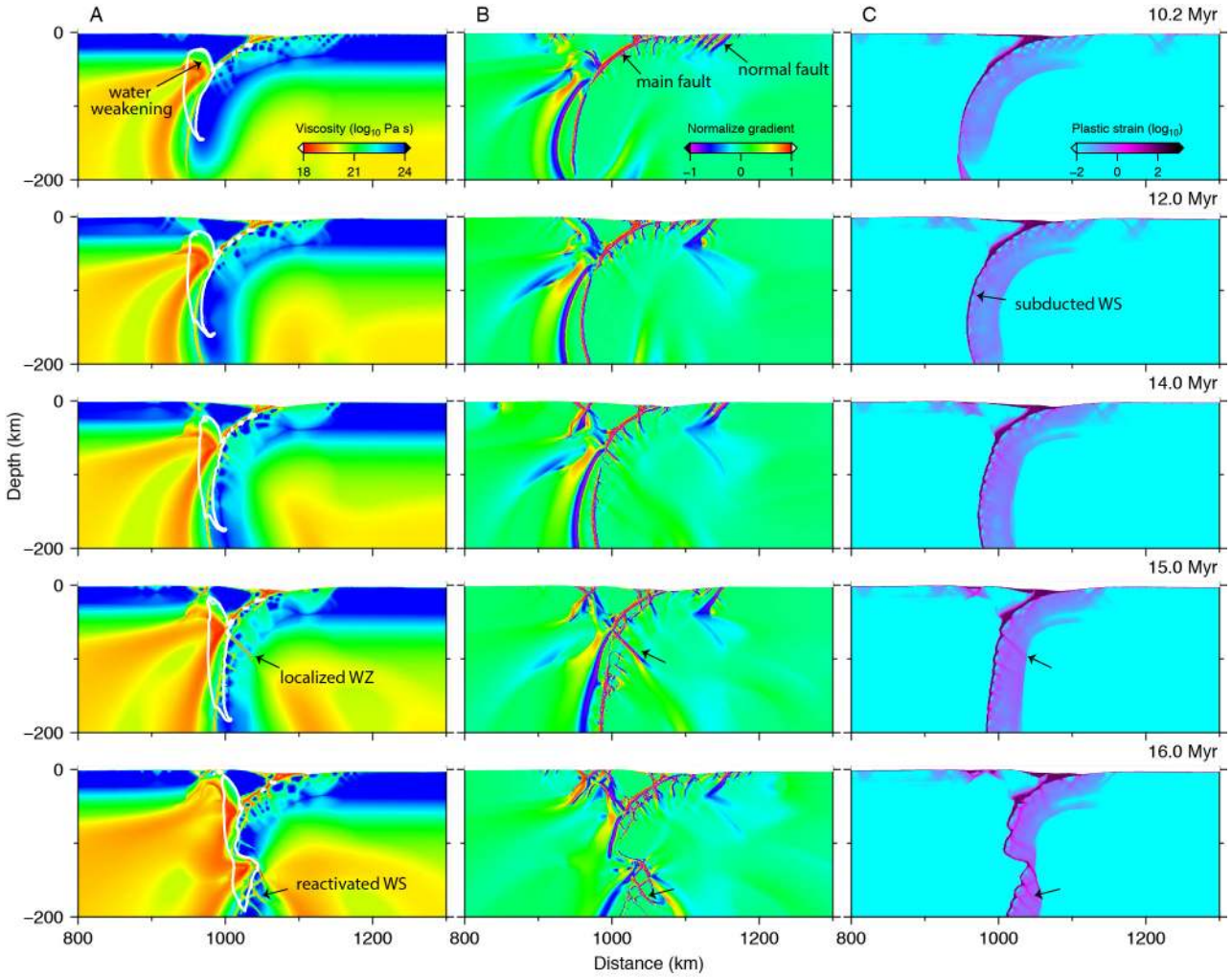

Figure 2.14: Development of the overriding plate failure and the slab detachment. (a) Effective viscosity. The white contour shows the free water content (120 ppm). (b) Normalized horizontal gradient of the second invariant of the strain rate tensor. This quantity basically shows how sharp the deformation region is, and therefore it is capable on the detection of active localized deformation. (c) Plastic strain. WS: weak structure; WZ: weak zone.

Deformation within detached slab

After detaching from the subducting slab (by 17 Myr), the sinking speed of the detached piece accelerates. Due to the shear thinning of the viscosity, the acceleration of the detached slab gives rise to a low viscosity shell around the detached slab, which in turn contributes to the acceleration. Deformation within the detached segment is moderate (Fig. 2.15b), with most of it under extension with some compression near the left edge of the segment (Fig. 2.15a). By 18.1 Myr, the detached segment

hits the lower mantle where the rheology is described by the diffusion law (linear) and the effective viscosity is much higher than the upper mantle. The strong lower mantle slows the sinking of the detached slab segment leading to strong compression within. Due to the preexisting weak structures within the detached slab segment, the apparent stress orientations are complex (Fig. 2.15a). Strong deformation (large strain rate) is revealed within the detached slab segment (Fig. 2.15b). About 1.8 Myr later, within the detached slab segment the deformation weakens. The detached slab segment sinks slowly into the lower mantle.

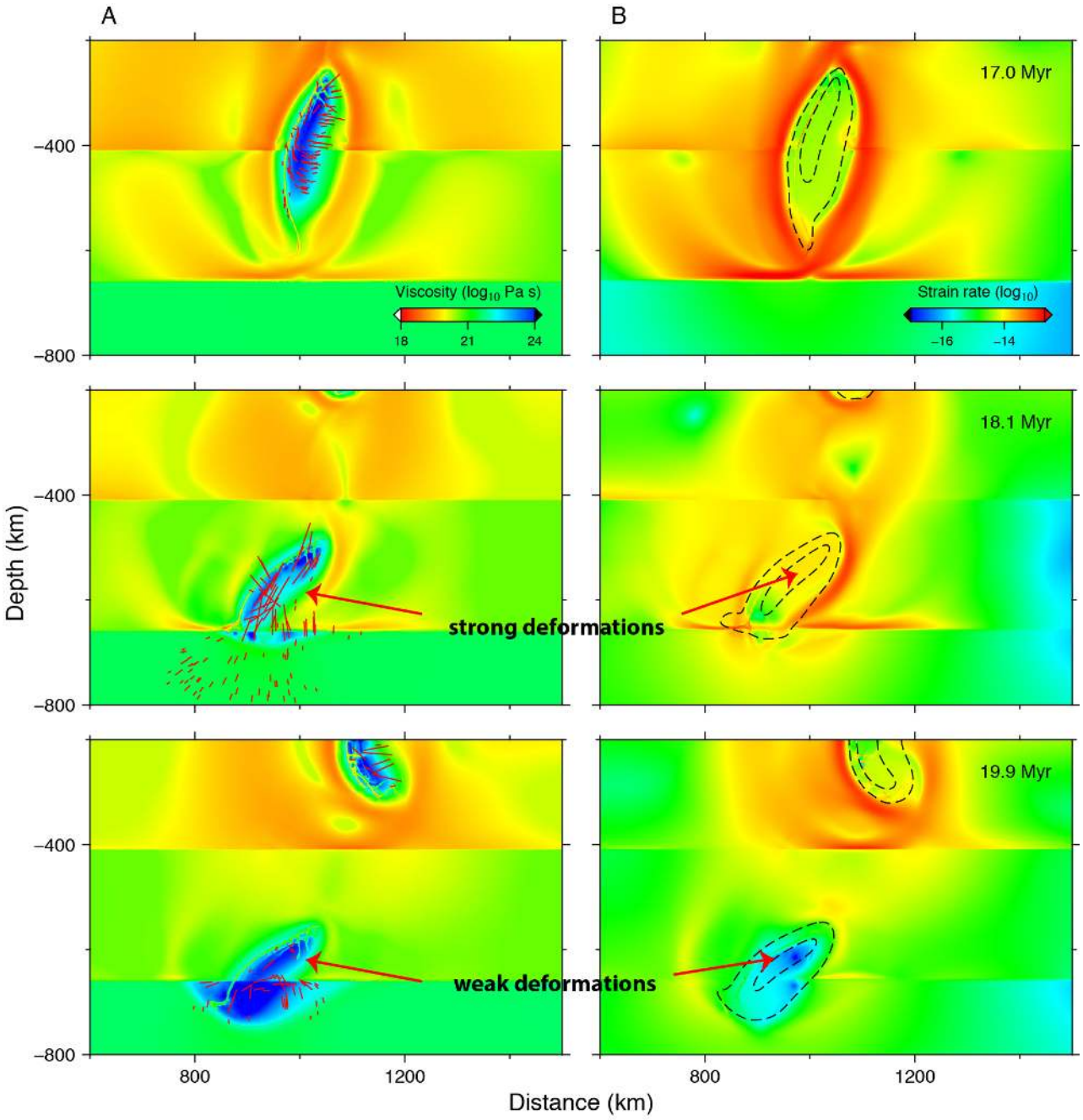

Figure 2.15: Evolution of the stress state and the deformation within the detached slab. (a) Effective viscosity. The red bar shows the direction and the amplitude of the maximum principle stress. (b) Second invariant of the strain rate tensor. The dashed black lines represent the isotherm of 800 °C and 1200 °C respectively.

Back-arc spreading and trench retreat

There are distinct aspects of the surface expression of fault structures during back-arc spreading and trench retreat (Fig. 2.16) Four tectonic features are recognized from the topography profiles from left to right: the spreading center, the arc region, the forearc region and the trench. The spreading center is at a regional topography low and corresponds to a velocity kink in the surface velocity profile. The velocity difference on the two sides of the kink defines the spreading rate (with full rates of $\sim$ 4 cm/yr at 17 Myr and $\sim$ 8 cm/yr at 20.6 Myr). The arc and forearc regions are separated with a set of steep faults, and their topographies and surface velocities are quite different. The arc region has a dome topography and uniform surface velocity. The convergence rate between the arc and the subducting plate is $\sim$ 6 cm/yr at 17 Myr and $\sim$ 10 cm/yr at 20.6 Myr. The forearc region usually has a relatively flat topography and a much larger convergence rate respect to subducting plate. Vertical offset between the trench and the forearc region is $\sim$ 2 km and remains invariant through its evolution. With the retreating and deepening of the trench, strong deformation occurs within the forearc, which explains the strong surface velocity variations in this region.

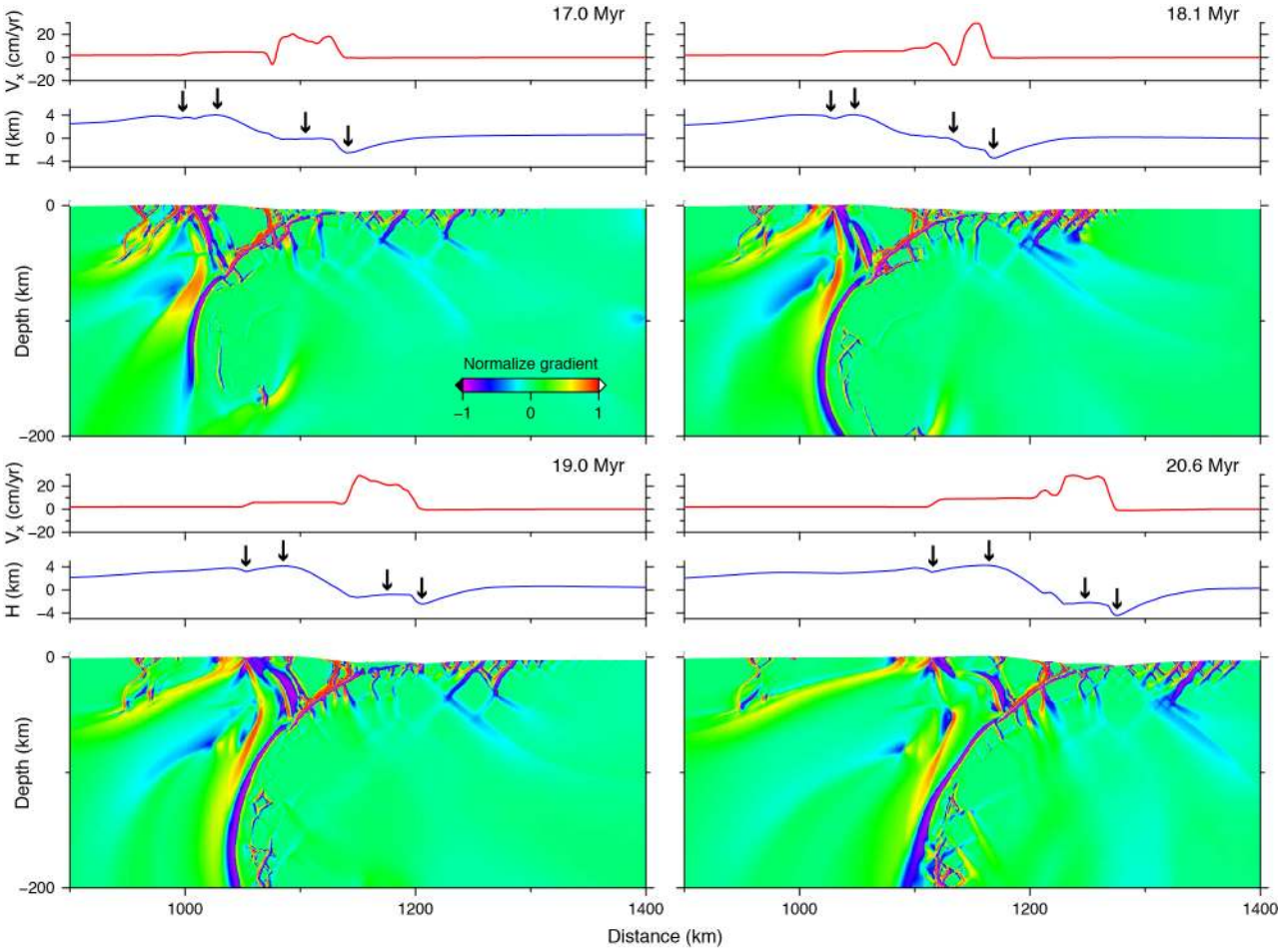

Figure 2.16: Evolution of back-arc spreading and trench retreat. The colored plots show active fault structures. The red lines (V_x) show the horizontal velocity at the surface with respect to the subducting plate. The blue lines (H) show the topography, and the black arrows above the topography represent the positions of the spreading center, the arc region, the forearc region, and the trench from left to right respectively.

2.5 Discussion and Conclusions

With our systematic comparison of models with different parameters during the early stage of subduction zone evolution, we determined the influence of different processes, and here discuss the implications of the coupled physical, chemical and surface processes.

With the comparison between models with free surface and free slip surface, we show that the change of surface geometry strongly influences the stress state and deformation pattern near the trench. With free slip surface, the transition of stress

and deformation near the surface are not as smooth as the case with free surface. These subtle changes in the stress and deformation illustrated in our models with different surface boundary conditions have long term influence on slab behavior and may lead to different evolutionary pathways of subduction zone in agreement with earlier work (Kaus et al., 2010). Free slip surface models with strong lithosphere (large viscosity) and plasticity are most likely to be influenced by these changes in stress and deformation when a strong plate bends. Adapting the curvature of the subduction interface near the surface to the flat top boundary (by either imposing a smooth fault geometry or adding a weak layer above the strong lithosphere) may help to make smoother transitions of the stress and plastic deformation and reduce the influence of the free slip boundary condition. With a lower maximum viscosity cutoff in models with no plastic failure, the influence of the free slip surface may also be reduced. Independent of lithospheric strength, the differences between the free surface topography and free slip surface topography at subduction zones are substantial. Free surfaces should be preferred for the prediction of subduction zone topography.

With the comparison among models with different erosion and sedimentation rates, we show that surface processes influence the magnitude and wavelength of topography variations and the size of the accretionary prism. The size of the accretionary prism has a strong influence on plate coupling at the subduction interface, and when the accretionary prism is small, plates may become strongly coupled. During subduction initiation, formation and maturation of the subduction interface control the evolution of the system. Our results suggest that the amount of weak materials near the trench strongly influences plate coupling and with more weak material, subduction initiation is more easily facilitated. This finding implies that with a continental or island arc overriding plate, the large amount of sedimentary inputs from the overriding plate may reduce the resistance on the subduction interface, favors subduction initiation. Sediments also increase the loading on the subducting plate, which may contribute to subduction initiation (e.g., Cloetingh et al., 1982). Extending to initiated subduction zones, if there is insuffcient weak material near the trench, the strong plate coupling may contribute to subduction erosion of the overriding plate.

With the comparison between models with or without sediments, we show that with the same amount of weak materials near the trench, the rheology and water content differences between sediments and crust do not substantially influence the evolution

of the system and model predictions. However, if both sediments and crustal material are absent, subduction evolution diverges from the original model, and the subducting and overriding plates remain strongly coupled during the entire evolution of the model. The decoupling in the mantle wedge resulting from water weakening does not substantially influence the stress state within the over-riding plate and the topography prediction, while water weakening contributes to the initiation of failure in the overriding plate. The crustal layer plays an important role in generating more realistic slab behaviors, and the incorporation of water weakening or similar weakening effects (e.g., serpentinization) on the overriding plate above the mantle wedge appears to be essential for the generation of back-arc spreading.

Comparison between models with and without elasticity shows that elasticity strongly influences the stress level within the plate during compression, while affecting the deformation and strain localization as the plate bends. Previous studies suggest that the importance of elasticity on subducting slab lies in its ability to shallow the slab dip via unbending, which may contribute to trench retreat (e.g., Fourel et al., 2014; Farrington et al., 2014). However, our results show that elasticity dose not affects the slab dip angle much with the existence of overriding plate and plasticity, while its importance may actually lie in changing the deformation pattern and generating localized shear bands on subducting plate at the bending region. Shear localization on the subducting plate occurs only in the case with elasticity as localization phenomena controlling self-regulation are thought to require a threshold value for energy input into the system, and the release of the stored energy contribute to localized weakening (Regenauer-Lieb et al., 2012). Subduction and reactivation of these localized weak structures formed at the bending region within the slab could influence the deformation and morphology of the slab as shown with the New Hebrides subduction zone model.

Most previous studies suggest that slab detachment usually occurs during subduction termination caused by the subduction of continental lithosphere or oceanic plateau which decreases the subduction rate (e.g., Gerya et al., 2004; Andrews and Billen, 2009). Leng and Gurnis (2011) show that with a fast strain weakening rate, slab detachment happens soon after subduction initiation, and the subducting plate continues to break after the onset of back-arc spreading (segmented subduction initiation). With a normal strain weakening rate and a constant subduction rate, we show that slab detachment can develop during the early stage of subduction zone evolution with the setting of a young subducting plate connected to a large plate

with moderate convergence rate, and the slab subducts continuously after the onset of back-arc spreading. The predicted size and position of the detached slab segment are compatible with the observations. A $\sim$ 2 km uplift in the forearc region and a rapid shallowing of the trench depth immediately after the slab detachment are suggested. Strong deformation happens within the detached slab segment when the accelerated segment hits the strong lower mantle. The deformation caused by the impact leads to the reactivation of preexisting weak structures within the detached slab segments, which may be able to generate large deep earthquakes near the bottom of the transition zone. After the impact, the deformation within the slab segment weakens. We suggest this transition from strong to weak deformation can be used to explain the difference in seismic intensities between northern and southern deep earthquake clusters. As suggested by the plate tectonic reconstruction of subducted slabs, detachments occurs earlier at the southern part of the New Hebrides subduction zone than in the north (Richards et al., 2011). We propose that the detached slab segment in the south has passed a transition from strong to weak deformation, while the detached slab segment in the north is still at the early stage of the transition. Therefore, few and dense earthquakes are recorded in the southern and the northern detached slab segments respectively. Although both the predicted topography and slab morphology are reasonable, some limitations exist for the full subduction zone model, including the $\sim$ 200 km trench retreat, which is shorter than the observed length at the southern part of the New Hebrides subduction zone and may be related to the simplifications we made for the overriding plate. The slab detachment may also be influenced by plastic parameters and the value of the imposed velocity on the subducting plate. However, a full investigation of the geological setting and model parameter spaces is out the scope of this chapter and currently impractical due to the large computational cost. Nevertheless, it is worthwhile for future work to explore more along these parameters with full subduction zone models.

In conclusion, we developed a multiphysics approach to simulate subduction zone evolution and to predict subduction zone topography. We discussed the influence of different geophysical, petrological and geochemical processes at subduction zones. Our model of the New Hebrides subduction zone explains the origin of isolated deep earthquakes and the difference in the seismic intensities between the northern and southern deep earthquake clusters. With the multiphysics approach, we are able to predict subduction zone topography as well as realistic slab behavior. We show that multiphysics geodynamic models is powerful approach to simulate subduction zone evolution, although computationally expensive. Some further work is needed

in order to make it more efficient, e.g., including adaptive mesh refinement to reduce the computation involved for high resolution model.

Acknowledgements

X. M. and M. G. were supported by the National Science Foundation through awards EAR-1247022, EAR-1645775, and OCE-1654766. D. A. M. acknowledges financial support from the European Research Council under the European Union's Seventh Framework Programme (FP7/2007-2013)/ERC Grant Agreement Number 279925 and the Alfred P. Sloan Foundation through the Deep Carbon Observatory (DCO) 'Modeling and Visualization'. Computations carried out on the NSF XSEDE systems were supported by TG-EAR160027. The simulations presented in this chapter were computed using a modified version of the open-source code pTatin3D, which can be obtained at https://bitbucket.org/ptatin/ptatin3d.

2.6 Appendix: Supplementary materials for the Chapter 2

Table S2.1: Table of models.

Model	Surface boundary condition	η_{max} (Pa s)	κ_s (m^2/yr)	Sediments or crust	Water weakening/ Elasticity	ε_0	Position
Case1	free surface	10^{24}	2×10^3	with both	Yes/Yes	0.4	Fig. 2.2a, 2.4b, 2.6a, 2.8a, S2.2b and S2.4a
Case2	free slip surface	10^{24}	2×10^3	with both	Yes/Yes	0.4	Fig. 2.2b
Case3	free slip surface	10^{23}	2×10^3	with both	Yes/Yes	0.4	Fig. S2.1a
Case4	free slip surface	10^{22}	2×10^3	with both	Yes/Yes	0.4	Fig. S12.b
Case5	free surface	10^{24}	1×10^3	with both	Yes/Yes	0.4	Fig. 2.4a and S2.2a
Case6	free surface	10^{24}	3×10^3	with both	Yes/Yes	0.4	Fig. 2.4c and S2.2c
Case7	free surface	10^{24}	4×10^3	with both	Yes/Yes	0.4	Fig. 2.4d and S2.2d
Case8	free surface	10^{24}	2×10^3	no sediments	Yes/Yes	0.4	Fig. 2.6b and S2.4b
Case9	free surface	10^{24}	2×10^3	no sediments or crust	Yes/Yes	0.4	Fig. 2.6c and S2.4c
Case10	free surface	10^{24}	2×10^3	with both	No/Yes	0.4	Fig. 2.6d and S2.4d
Case11	free surface	10^{24}	2×10^3	with both	Yes/No	0.4	Fig. 2.8b
Case12	free surface	10^{24}	2×10^3	with both	Yes/No	0.2	Fig. 2.8c
Case13	free surface	10^{24}	2×10^3	with both	Yes/No	0.6	Fig. 2.8d
Case14	free slip surface (time evolutionary)	10^{24}	2×10^3	with both	Yes/Yes	0.4	

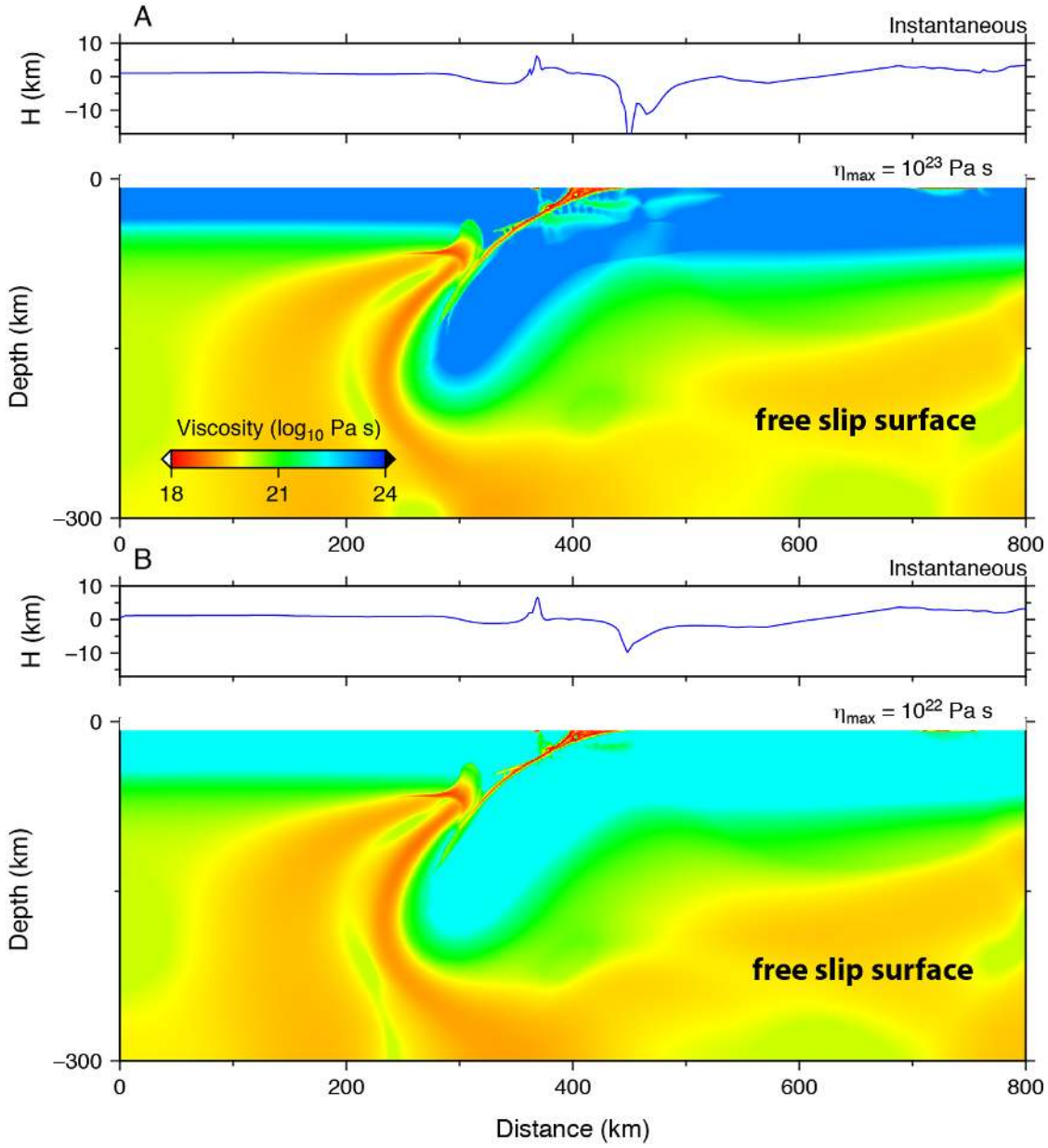

Figure S2.1: Two more cases with free slip surface and lower maximum viscosity cutoffs: (a) η_{max}=10^{23} Pa s and (b) η_{max}=10^{22} Pa s.

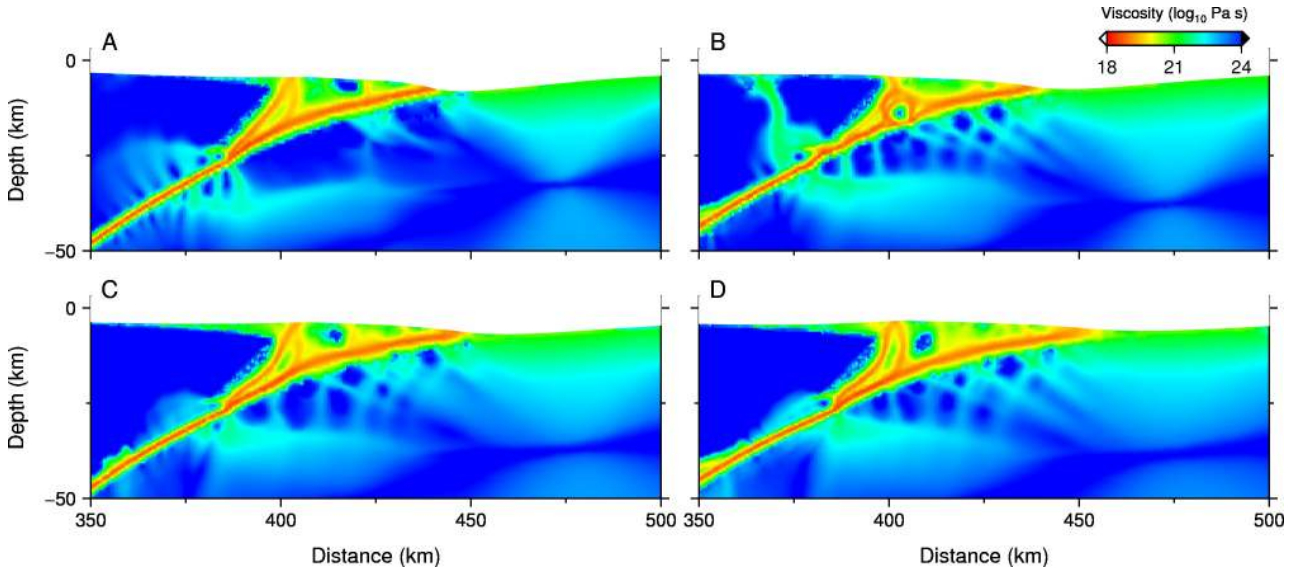

Figure S2.2: Zoom ins show the size of weak prism for cases with different surface diffusion coefficients (a) 1×10^3 m^2/yr, (b) 2×10^3 m^2/yr (reference model), (c) 3×10^3 m^2/yr, and (d) 4×10^3 m^2/yr.

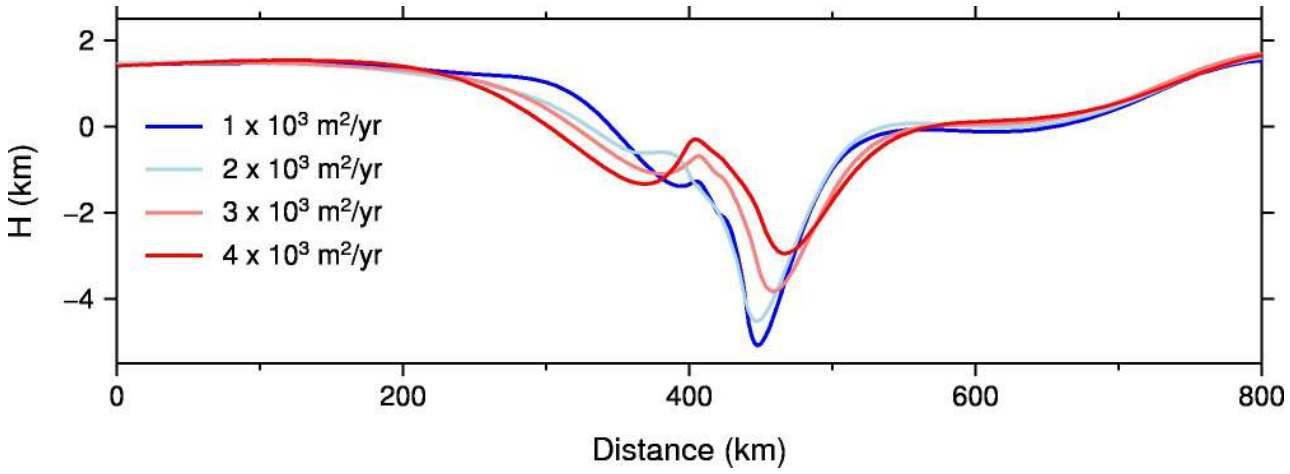

Figure S2.3: Topography profiles for cases with different surface diffusion coefficients.

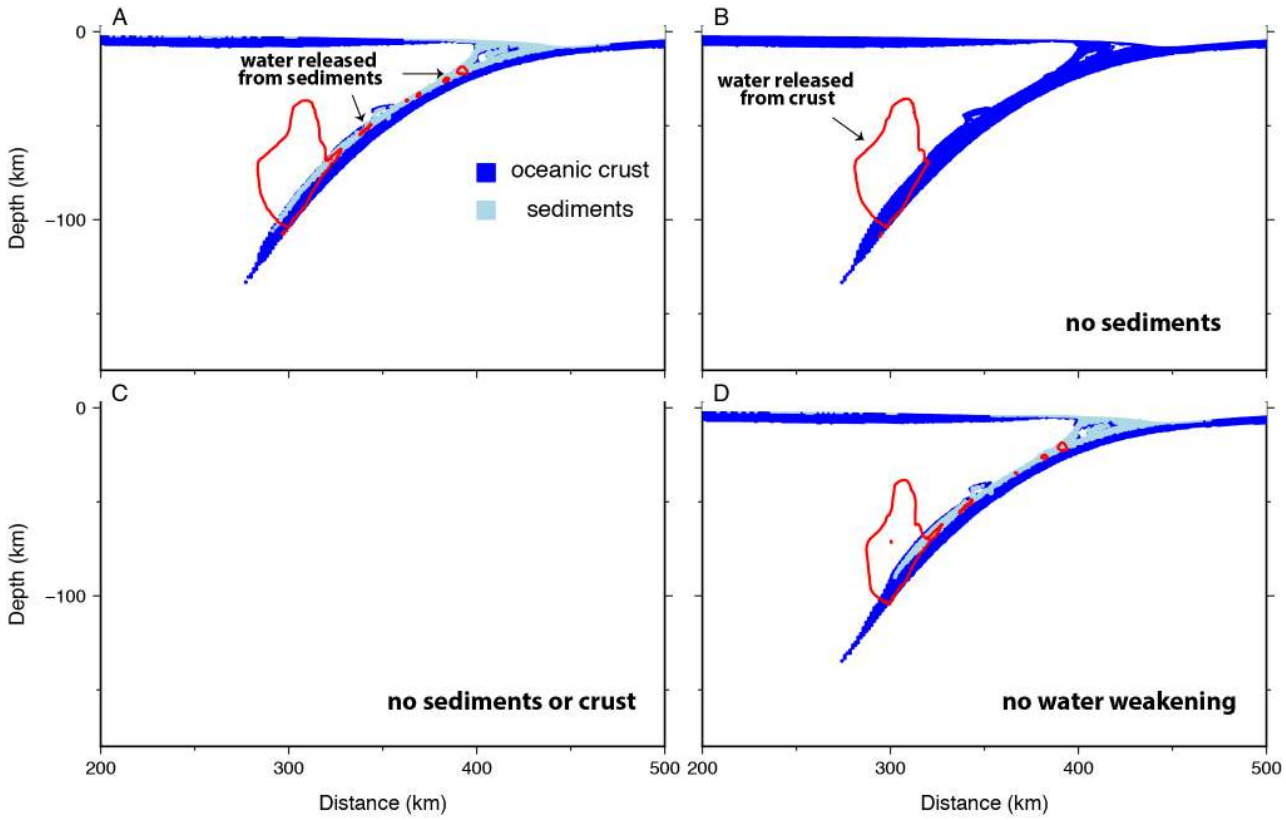

Figure S2.4: Zoom-ins show the distributions of sediments and oceanic crust: (a) reference model, (b) model without sediments, (c) model without sediments or crust, and (d) model without water weakening. The red contour shows the free water content (120 ppm).

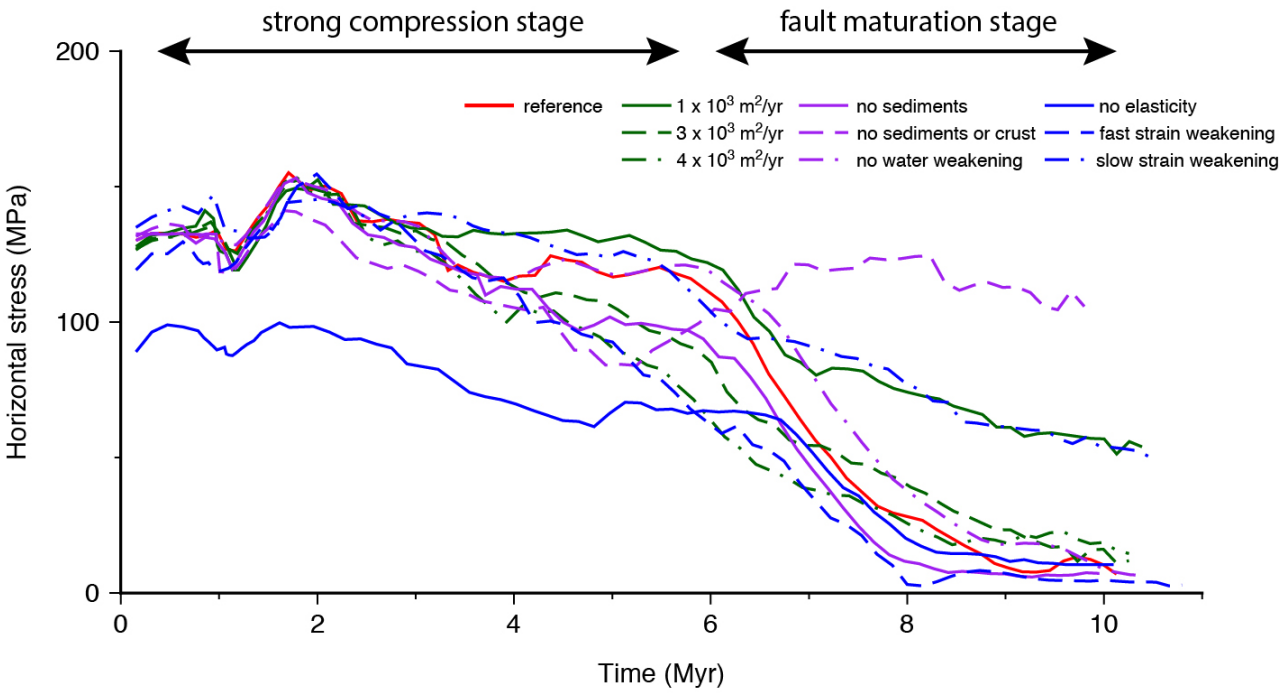

Figure S2.5: Compilation of averaged horizontal stresses within overriding plate for different models. The averaging is performed within the region that spans from 100 km to 300 km distance and surface to 40 km depth

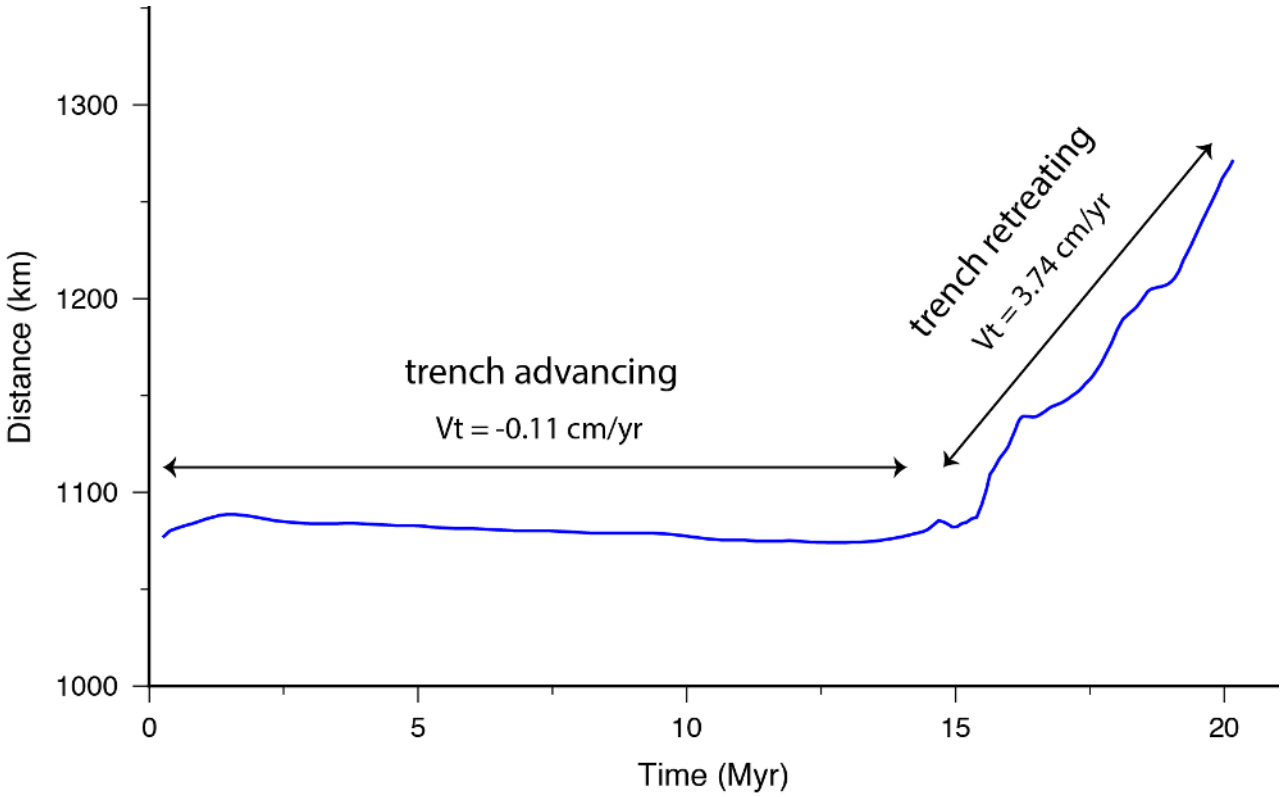

Figure S2.6: Trench position as a function of time. Vt denotes the velocity of trench migration.

References

Andrews, Erin R and Magali I Billen (2009). Rheologic controls on the dynamics of slab detachment. *Tectonophysics*, 464(1-4):60–69. doi: 10.1016/j.tecto.2007.09.004.

Audet, Pascal, Michael G Bostock, Nikolas I Christensen, and Simon M Peacock (2009). Seismic evidence for overpressured subducted oceanic crust and megathrust fault sealing. *Nature*, 457(7225):76. doi: 10.1038/nature07650.

Avouac, J-Ph and EB Burov (1996). Erosion as a driving mechanism of intracontinental mountain growth. *Journal of Geophysical Research: Solid Earth*, 101 (B8):17747–17769. doi: 10.1029/96JB01344.

Bebout, Gray E (2007). Metamorphic chemical geodynamics of subduction zones. *Earth and Planetary Science Letters*, 260(3-4):373–393. doi: 10.1016/j.gca.2006.06.196.

Billen, Magali I and Michael Gurnis (2005). Constraints on subducting plate strength within the Kermadec trench. *Journal of Geophysical Research: Solid Earth*, 110 (B5). doi: 10.1029/2004jb003308.

Braun, Jean and Malcolm Sambridge (1994). Dynamical Lagrangian Remeshing (dlr): a new algorithm for solving large strain deformation problems and its application to fault-propagation folding. *Earth and Planetary Science Letters*, 124(1-4):211–220. doi: 10.1016/0148-9062(95)90210-4.

Bremaecker, Jean-Claude (1977). Is the oceanic lithosphere elastic or viscous? *Journal of Geophysical Research*, 82(14):2001–2004. doi: 10.1029/jb082i014p02001.

Burov, Evgenii and G Toussaint (2007). Surface processes and tectonics: forcing of continental subduction and deep processes. *Global and Planetary Change*, 58 (1-4):141–164. doi: 10.1016/j.gloplacha.2007.02.009.

Buschelman, Kris, Lisandro Dalcin, Victor Eijkhout, William D. Gropp, Dinesh Kaushik, Matthew G. Knepley, Dave A. May, Lois Curfman McInnes, Karl Rupp, Barry F. Smith, Stefano Zampini, Hong Zhang, and Hong Zhang. PETSc Web page. 2017. URL http://www.mcs.anl.gov/petsc.

Caldwell, JG and DL Turcotte (1979). Dependence of the thickness of the elastic oceanic lithosphere on age. *Journal of Geophysical Research: Solid Earth*, 84 (B13):7572–7576. doi: 10.1029/jb084ib13p07572.

Capitanio, FA, G Morra, and S Goes (2007). Dynamic models of downgoing plate-buoyancy driven subduction: Subduction motions and energy dissipation. *Earth and Planetary Science Letters*, 262(1-2):284–297. doi: 10.1016/j.epsl.2007.07.039.

Cloetingh, Sierd Auke Pieter Leonard, MJR Wortel, and NJ Vlaar (1982). Evolution of passive continental margins and initiation of subduction zones. *Nature*, 297 (5862):139. doi: 10.1038/297139a0.

Connolly, JAD and K Petrini (2002). An automated strategy for calculation of phase diagram sections and retrieval of rock properties as a function of physical conditions. *Journal of Metamorphic Geology*, 20(7):697–708. doi: 10.1046/j.1525-1314.2002.00398.x.

Connolly, James AD (2005). Computation of phase equilibria by linear programming: a tool for geodynamic modeling and its application to subduction zone decarbonation. *Earth and Planetary Science Letters*, 236(1):524–541. doi: 10.1016/j.epsl.2005.04.033.

Crameri, F, H Schmeling, GJ Golabek, T Duretz, R Orendt, SJH Buiter, DA May, BJP Kaus, TV Gerya, and PJ Tackley (2012a). A comparison of numerical surface topography calculations in geodynamic modelling: an evaluation of the 'sticky air' method. *Geophysical Journal International*, 189(1):38–54. doi: 10.1111/j.1365-246x.2012.05388.x.

Crameri, F, CR Lithgow-Bertelloni, and PJ Tackley (2017). The dynamical control of subduction parameters on surface topography. *Geochemistry, Geophysics, Geosystems*. doi: 10.1002/2017gc006821.

Crameri, Fabio, PJ Tackley, Irena Meilick, TV Gerya, and BJP Kaus (2012b). A free plate surface and weak oceanic crust produce single-sided subduction on earth. *Geophysical Research Letters*, 39(3). doi: 10.1029/2011gl050046.

Dziewonski, AM, T-A Chou, and JH Woodhouse (1981). Determination of earthquake source parameters from waveform data for studies of global and regional seismicity. *Journal of Geophysical Research: Solid Earth*, 86(B4):2825–2852. doi: 10.1029/JB086iB04p02825.

Farrington, RJ, L-N Moresi, and FA Capitanio (2014). The role of viscoelasticity in subducting plates. *Geochemistry, Geophysics, Geosystems*, 15(11):4291–4304. doi: 10.1002/2014gc005507.

Fourel, Loic, Saskia Goes, and Gabriele Morra (2014). The role of elasticity in slab bending. *Geochemistry, Geophysics, Geosystems*, 15(11):4507–4525. doi: 10.1002/2014gc005535.

Gerya, Taras V, Bernhard Stöckhert, and Alexey L Perchuk (2002). Exhumation of high-pressure metamorphic rocks in a subduction channel: A numerical simulation. *Tectonics*, 21(6). doi: 10.1029/2002tc001406.

Gerya, Taras V, David A Yuen, and Walter V Maresch (2004). Thermomechanical modelling of slab detachment. *Earth and Planetary Science Letters*, 226(1): 101–116. doi: 10.1016/j.epsl.2004.07.022.

Gerya, Taras V, James AD Connolly, David A Yuen, Weronika Gorczyk, and Allison M Capel (2006). Seismic implications of mantle wedge plumes. *Physics of the Earth and Planetary Interiors*, 156(1-2):59–74. doi: 10.1016/j.pepi.2006.02.005.

Goetze, Christopher and Brian Evans (1979). Stress and temperature in the bending lithosphere as constrained by experimental rock mechanics. *Geophysical Journal International*, 59(3):463–478. doi: 10.1111/j.1365-246x.1979.tb02567.x.

Gurnis, Michael, Christophe Eloy, and Shijie Zhong (1996). Free-surface formulation of mantle convection–II. Implication for subduction-zone observables. *Geophysical Journal International*, 127(3):719–727. doi: 10.1111/j.1365-246X.1996.tb04050.x.

Gurnis, Michael, Shijie Zhong, and John Toth (2000). On the competing roles of fault reactivation and brittle failure in generating plate tectonics from mantle convection. *The History and Dynamics of Global Plate Motions*, pages 73–94. doi: 10.1029/gm121p0073.

Gurnis, Michael, Chad Hall, and Luc Lavier (2004). Evolving force balance during incipient subduction. *Geochemistry, Geophysics, Geosystems*, 5(7). doi: 10.1029/2003gc000681.

Hamburger, Michael W and Bryan L Isacks (1987). Deep earthquakes in the southwest Pacific: A tectonic interpretation. *Journal of Geophysical Research: Solid Earth*, 92(B13):13841–13854. doi: 10.1029/jb092ib13p13841.

Hebert, Laura Baker, Paula Antoshechkina, Paul Asimow, and Michael Gurnis (2009). Emergence of a low-viscosity channel in subduction zones through the coupling of mantle flow and thermodynamics. *Earth and Planetary Science Letters*, 278(3-4):243–256. doi: 10.1016/j.epsl.2008.12.013.

Hirth, Greg and David L Kohlstedt (1996). Water in the oceanic upper mantle: implications for rheology, melt extraction and the evolution of the lithosphere. *Earth and Planetary Science Letters*, 144(1-2):93–108. doi: 10.1016/0012-821x(96)00154-9.

Hofmann, Albrecht W and William M White (1982). Mantle plumes from ancient oceanic crust. *Earth and Planetary Science Letters*, 57(2):421–436. doi: 10.1016/0012-821x(82)90161-3.

Hu, Jiashun, Lijun Liu, Armando Hermosillo, and Quan Zhou (2016). Simulation of late Cenozoic South American flat-slab subduction using geodynamic models with data assimilation. *Earth and Planetary Science Letters*, 438:1–13. doi: 10.1016/j.epsl.2016.01.011.

International Seismological Centre (2014). *On-line Bulletin*. Internatl. Seismol. Cent., Thatcham, United Kingdom. http://www.isc.ac.uk.

Jiao, Wenjie, Paul G Silver, Yingwei Fei, and Charles T Prewitt (2000). Do intermediate-and deep-focus earthquakes occur on preexisting weak zones? An examination of the Tonga subduction zone. *Journal of Geophysical Research: Solid Earth*, 105(B12):28125–28138. doi: 10.1029/2000jb900314.

Jourdon, Anthony, Laetitia Le Pourhiet, Carole Petit, and Yann Rolland (2017). The deep structure and reactivation of the kyrgyz tien shan: Modelling the past to better constrain the present. *Tectonophysics*. doi: 10.1016/j.tecto.2017.07.019.

Kaus, Boris JP, Clare Steedman, and Thorsten W Becker (2008). From passive continental margin to mountain belt: insights from analytical and numerical models and application to taiwan. *Physics of the Earth and Planetary Interiors*, 171(1):235–251. doi: 10.1016/j.pepi.2008.06.015.

Kaus, Boris JP, Hans Mühlhaus, and Dave A May (2010). A stabilization algorithm for geodynamic numerical simulations with a free surface. *Physics of the Earth and Planetary Interiors*, 181(1):12–20. doi: 10.1016/j.pepi.2010.04.007.

Keunings, R (2000). Advances in the computer modeling of the flow of polymetric liquids. *Computational Fluid Dynamics Journal*, 9(1):449–458.

King, Scott D (2009). On topography and geoid from 2-D stagnant lid convection calculations. *Geochemistry, Geophysics, Geosystems*, 10(3). doi: 10.1029/2008gc002250.

Kodaira, Shuichi, Takashi Iidaka, Aitaro Kato, Jin-Oh Park, Takaya Iwasaki, and Yoshiyuki Kaneda (2004). High pore fluid pressure may cause silent slip in the nankai trough. *Science*, 304(5675):1295–1298. doi: 10.1126/science.1096535.

Lamb, Simon (2006). Shear stresses on megathrusts: Implications for mountain building behind subduction zones. *Journal of Geophysical Research: Solid Earth*, 111(B7). doi: 10.1029/2005jb003916.

Lemiale, V, H-B Mühlhaus, Louis Moresi, and J Stafford (2008). Shear banding analysis of plastic models formulated for incompressible viscous flows. *Physics of the Earth and Planetary Interiors*, 171(1-4):177–186. doi: 10.1016/j.pepi.2008.07.038.

Leng, Wei and Michael Gurnis (2011). Dynamics of subduction initiation with different evolutionary pathways. *Geochemistry, Geophysics, Geosystems*, 12(12). doi: 10.1029/2011gc003877.

Li, Dunzhu, Michael Gurnis, and Georg Stadler (2017). Towards adjoint-based inversion of time-dependent mantle convection with nonlinear viscosity. *Geophysical Journal International*, 209(1):86–105. doi: 10.1093/gji/ggw493.

Li, ZH, TV Gerya, and J-P BURG (2010). Influence of tectonic overpressure on P–T paths of HP–UHP rocks in continental collision zones: thermomechanical modelling. *Journal of Metamorphic Geology*, 28(3):227–247. doi: 10.1111/j.1525-1314.2009.00864.x.

Liu, Lijun and Dave R Stegman (2011). Segmentation of the Farallon slab. *Earth and Planetary Science Letters*, 311(1-2):1–10. doi: 10.1016/j.epsl.2011.09.027.

Liu, Sibiao and Claire A Currie (2016). Farallon plate dynamics prior to the Laramide orogeny: Numerical models of flat subduction. *Tectonophysics*, 666:33–47. doi: 10.1016/j.tecto.2015.10.010.

Mallard, Claire, Nicolas Coltice, Maria Seton, R Dietmar Müller, and Paul J Tackley (2016). Subduction controls the distribution and fragmentation of Earth's tectonic plates. *Nature*, 535(7610):140. doi: 10.1038/nature17992.

Manea, Vlad and Michael Gurnis (2007). Subduction zone evolution and low viscosity wedges and channels. *Earth and Planetary Science Letters*, 264(1-2):22–45. doi: 10.1016/j.epsl.2007.08.030.

Mann, Paul and Asahiko Taira (2004). Global tectonic significance of the Solomon Islands and Ontong Java Plateau convergent zone. *Tectonophysics*, 389(3-4): 137–190. doi: 10.1016/j.tecto.2003.10.024.

Mao, Xiaolin, Michael Gurnis, and Dave A May (2017). Subduction initiation with vertical lithospheric heterogeneities and new fault formation. *Geophysical Research Letters*, 44(22). doi: 10.1002/2017gl075389.

May, Dave A, Jed Brown, and Laetitia Le Pourhiet (2014). pTatin3d: High-performance methods for long-term lithospheric dynamics. In *Proceedings of the International Conference for High Performance Computing, Networking, Storage and Analysis*, pages 274–284. IEEE Press. doi: 10.1109/SC.2014.28.

May, David A, Jed Brown, and Laetitia Le Pourhiet (2015). A scalable, matrix-free multigrid preconditioner for finite element discretizations of heterogeneous Stokes flow. *Computer Methods in Applied Mechanics and Engineering*, 290: 496–523. doi: 10.1016/j.cma.2015.03.014.

McKenzie, Dan P, Jean M Roberts, and Nigel O Weiss (1974). Convection in the Earth's mantle: towards a numerical simulation. *Journal of Fluid Mechanics*, 62 (3):465–538. doi: 10.1017/s0022112074000784.

Moresi, Louis, Frédéric Dufour, and H-B Mühlhaus (2002). Mantle convection modeling with viscoelastic/brittle lithosphere: Numerical methodology and plate tectonic modeling. *Pure and Applied Geophysics*, 159(10):2335–2356. doi: 10.1007/s00024-002-8738-3.

Okal, Emile A and Stephen H Kirby (1998). Deep earthquakes beneath the Fiji Basin, SW Pacific: Earth's most intense deep seismicity in stagnant slabs. *Physics of the Earth and Planetary Interiors*, 109(1-2):25–63. doi: 10.1016/s0031-9201(98)00116-2.

Regenauer-Lieb, Klaus, Roberto F Weinberg, and Gideon Rosenbaum (2012). The role of elastic stored energy in controlling the long term rheological behaviour of the lithosphere. *Journal of Geodynamics*, 55:66–75. doi: 10.1016/j.jog.2011.08.003.

Richards, Simon, Robert Holm, and Grace Barber (2011). When slabs collide: A tectonic assessment of deep earthquakes in the Tonga-Vanuatu region. *Geology*, 39(8):787–790. doi: 10.1130/g31937.1.

Salles, Tristan, Nicolas Flament, and D Müller (2017). Influence of mantle flow on the drainage of eastern Australia since the Jurassic Period. *Geochemistry, Geophysics, Geosystems*, 18(1):280–305. doi: 10.1002/2016gc006617.

Schmeling, H, AY Babeyko, A Enns, C Faccenna, F Funiciello, T Gerya, GJ Golabek, S Grigull, BJP Kaus, G Morra, et al. (2008). A benchmark comparison of spontaneous subduction models–Towards a free surface. *Physics of the Earth and Planetary Interiors*, 171(1-4):198–223. doi: 10.1029/2008gc002250.

Stixrude, Lars and Carolina Lithgow-Bertelloni (2011). Thermodynamics of mantle minerals–II. Phase equilibria. *Geophysical Journal International*, 184(3):1180–1213. doi: 10.1111/j.1365-246x.2010.04890.x.

Tackley, Paul J, David J Stevenson, Gary A Glatzmaier, and Gerald Schubert (1993). Effects of an endothermic phase transition at 670 km depth in a spherical model of convection in the earth's mantle. *Nature*, 361(6414):699. doi: 10.1038/361699a0.

Thielmann, Marcel, Boris JP Kaus, and Anton A Popov (2015). Lithospheric stresses in Rayleigh–Bénard convection: effects of a free surface and a viscoelastic Maxwell rheology. *Geophysical Supplements to the Monthly Notices of the Royal Astronomical Society*, 203(3):2200–2219. doi: 10.1093/gji/ggv436.

Zhong, Shijie and Michael Gurnis (1994). Controls on trench topography from dynamic models of subducted slabs. *Journal of Geophysical Research: Solid Earth*, 99(B8):15683–15695. doi: 10.1029/94jb00809.

Zhong, Shijie and Michael Gurnis (1995). Mantle convection with plates and mobile, faulted plate margins. *Science*, 267(5199):838–843. doi: 10.1126/science.267.5199.838.

Chapter 3

SUBDUCTION INITIATION WITH VERTICAL LITHOSPHERIC HETEROGENEITIES AND NEW FAULT FORMATION

Mao, Xiaolin, Michael Gurnis, and Dave A May (2017). Subduction initiation with vertical lithospheric heterogeneities and new fault formation. *Geophysical Research Letters*, 44(22). doi: 10.1002/2017GL075389.

How subduction initiates with mechanically unfavorable lithospheric heterogeneities is important and rarely studied. We investigate this with a geodynamic model for the Puysegur Incipient Subduction Zone (PISZ) south of New Zealand. The model incorporates a true free surface, elasto-visco-plastic rheology and phase changes. Our predictions fit the morphology of the Puysegur Trench and Ridge and the deformation history on the overriding plate. We show how a new thrust fault forms and evolves into a smooth subduction interface, and how a preexisting weak zone can become a vertical fault inboard of the thrust fault during subduction initiation, consistent with two-fault system at PISZ. The model suggests that the PISZ may not yet be self-sustaining. We propose that the Snares Zone (or Snares Trough) is caused by plate coupling differences between shallower and deeper parts, that the tectonic sliver between two faults experiences strong rotation, and that low density material accumulates beneath the Snares Zone.

3.1 Introduction

Subduction initiation is a vital phase of the plate tectonic cycle since it fundamentally alters the global force balance on tectonic plates. Numerical studies have advanced our understanding of under what circumstances and with what physical processes a new subduction zone can develop (Toth and Gurnis, 1998; Regenauer-Lieb et al., 2001; Gurnis et al., 2004; Nikolaeva et al., 2010; Thielmann and Kaus, 2012), but uncertainty still exists and key parameters related to subduction initiation remain poorly quantified mainly due to the lack of good constraints on numerical models. Subduction initiation can be either induced or spontaneous: induced subduction initiation begins with strong compression and uplift (Gurnis et al., 2004), whereas spontaneous initiation begins with rifting and subsidence (Stern, 2004). Therefore, topographic changes that result from subduction initiation can be used to distinguish

different initiation modes and can potentially be used to quantify parameters that control the initiation process. While the importance of topographic change in subduction initiation has been noticed previously (Gurnis et al., 2004), applying topographic changes as a constraint on subduction initiation process at a specific subduction zone has not been addressed, as most of the early record needed to constrain the dynamics is over-printed by later deformation and volcanism for mature subduction zones, like the well known examples of the Eocene initiation of Izu-Bonin-Marianas and Tonga-Kermadec subduction zones (Sutherland et al., 2006). On the other hand, some possible incipient subduction zones are so young (Gorringe Bank, the Owen Ridge, the Hjort Trench, Mussau Trench) that the slab may not have yet started to bend into the mantle (Gurnis et al., 2004).

Luckily, one subduction zone overcomes these limitations: the Puysegur Incipient Subduction Zone (PISZ). The Puysegur Trench and Ridge form the northern end of the Macquarie Ridge Complex (MRC) defining the Australian-Pacific plate margin south of New Zealand (Fig. 3.1a). Since about 20 Ma, highly oblique convergence beneath the Puysegur Ridge results in a maximum total convergence of 150-200 km at Puysegur as suggested by a Benioff zone with seismicity down to 150 km depth (Fig. 3.1c) (Sutherland et al., 2006). Subduction related igneous rocks, especially adakite, which is formed by the partial melting of young oceanic crust under eclogitic facies conditions, are sparsely distributed on the overriding plate at Solander Island (Reay and Parkinson, 1997). This confirms that the slab enters the mantle. The morphology of the Puysegur Ridge (Fig. 3.1b) shows a characteristic change from uplift in the southern part, where the total convergence is less, and subsidence in the northern part, the Snares Zone (or Snares Trough), where the total convergence is largest, and is roughly consistent with geodynamic models of induced subduction initiation (Gurnis et al., 2004). Discrete flat-topped segments, which are interpreted as the results of subaerial exposure and erosion, are also evident at both northern and southern parts of the Puysegur Ridge (Fig. 3.1d). The southernmost segment is close to sea level (-120 m), while a peak subsidence of $\sim$ 1800 m is found in the Snares Zone in the north, suggesting that the southern part has only experienced uplift, while there was uplift followed by subsidence in the Snares Zone (Collot et al., 1995; Lebrun et al., 1998; Gurnis et al., 2004). The width of the Puysegur ridge also widens northwards from less than 50 km at 49.5° S to $\sim$ 80 km at 47.5° S . A confined strike slip fault zone is found near the peak of the ridge in the south, while a splayed fault zone structure is suggested in the trough of the Snares Zone (Fig. 3.1d). Together, they show that the overriding plate close to the trench is

under compression in the south and potentially in extension in the north (Collot et al., 1995; Lamarche and Lebrun, 2000). The corresponding trench depth in the south is about 1 km shallower than in the north (Collot et al., 1995). These spatial variations in structure along the PISZ are thought to represent different time periods in the evolution, and a space-for-time substitution can be made to compare the time evolution from 2D models with the spatial variation along the PISZ.

The two-fault system at PISZ, with a thrust fault at the trench and a vertical fault inboard of the thrust fault, is recognized through the dual rupture mode for large earthquakes and interpretations of multibeam bathymetric, sonar imagery, seismic reflection and geopotential data (Ruff et al., 1989; Collot et al., 1995). However, how this two-fault structure formed is still open to debate. Ruff et al. (1989) propose that the thrust interface formed through the propagation and connection of disconnected small thrust faults behind the vertical fault, while this hypothesis preceded the mapping of these two faults. Collot et al. (1995) propose that it developed through progressive adjustments of two adjacent vertical weak zones under compression, which requires the development of the ridge and differential uplift of the crustal block at one weak zone, and the rotation of the other. Here, we propose that the two-fault system formed through developing a new thrust fault near the preexisting vertical fault during subduction initiation. Previous studies suggest that there is a transition in the force balances from being forced externally to a state of self-sustaining subduction under its own negative buoyancy for induced subduction initiation (Gurnis et al., 2004; Leng and Gurnis, 2011). However, it is not clear whether PISZ is self-sustaining, or if the along strike variation in the uplift and subsidence of the Puysegur Ridge represents this transition. Here we use 2D geodynamic models, which have a true free surface to track topographic changes, and model setup and boundary conditions tailored for PISZ, to test our hypothesis for the formation of the two-fault system at PISZ, and to explore the factors that control the transition in the force balance, while focusing on the evolution of topography and state of stress.

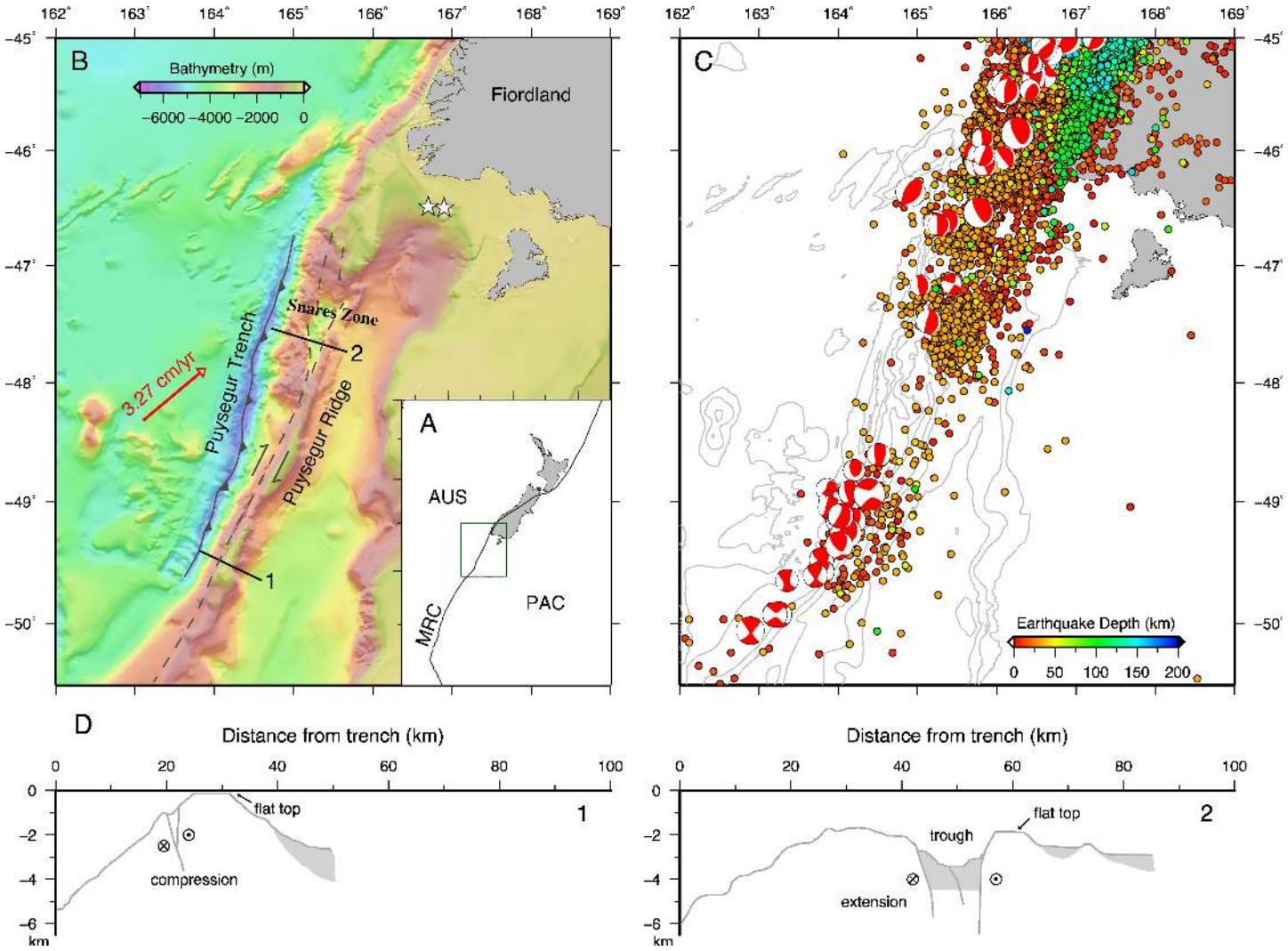

Figure 3.1: (a) Tectonic outline of the Puysegur region. AUS: Australian Plate; PAC: Pacific Plate; MRC: Macquarie Ridge Complex. (b) Bathymetry of the Puysegur Incipient Subduction Zone. The red vector is the relative velocity of AUS to PAC (DeMets et al., 1994). Stars show the location of young volcanic features (Sutherland et al., 2006), and black lines show position of cross sections in d. Dashed lines show possible position of the Puysegur Fault. (c) Filled circles are earthquakes with magnitude between 2 to 5 from the ISC Bulletin (International Seismological Centre, 2014), and the focal mechanism solutions are from CMT catalog (Dziewonski et al., 1981). (d) Bathymetry cross sections and inferred fault structures (modified from Lebrun et al. (1998)).

3.2 Method

Although a number of studies have tracked the topography in subduction zone models (e.g., Zhong and Gurnis, 1994; Billen and Gurnis, 2001; Kaus et al., 2008; Gerya and Meilick, 2011), predicting reliable topographic evolution in subduction zone remains a challenge. By reliable topography, we mean that not only is the predicted topography consistent with that observed, but the model should also be able to include most of the important geophysical, petrological and geochemical processes that affect the force balance, and the model setup, boundary conditions and the evolution of material properties need to be self-consistent and properly constrained. During subduction initiation, the driving forces must overcome the resisting forces from the friction on the sliding interface, the bending of lithosphere and the buoyancy of oceanic crust (before the basalt-to-eclogite phase change) (e.g., McKenzie, 1977; Toth and Gurnis, 1998). With the subduction of the down-going slab, phase changes in the crust lead to an increasing crustal density, and this part of the resisting force evolves to drive subduction. Fluids released from the subducting crust contribute to the decoupling between subducting and overriding plates, which may reduce the resisting force. Also influencing the force balance is the development of topography and surface process, which generate loads that affect lithospheric and mantle dynamics (Kaus et al., 2008, 2010).

A true free surface is tracked in pTatin3D (May et al., 2014, 2015), based on the Arbitrary Lagrangian Eulerian (ALE) finite element method, and is used to follow the dynamic mantle-surface interactions and the topographic evolution. Initial topography is calculated from isostasy (Fig. 3.2), and topography is updated between time steps with surface velocity under the constraint that the vertical topographic change is smaller than 20 meters to avoid topographic oscillation (Kaus et al., 2010). A simplified surface process model, based on linear topographic diffusion, is implemented (e.g., Avouac and Burov, 1996). A 5 km thick altered basaltic crust is placed on the top of dry pyrolite, and sediments are generated at the surface with our surface process. Density and free water content for different phase assemblages are gained by referring to precalculated 4D (temperature, pressure, rock type and total water content) phase maps using Perplex (Connolly, 2005). Darcy's law is used to migrate free water, and a linear water weakening is applied to the mantle material (Hirth and Kohlstedt, 1996). The Drucker-Prager yield criteria with a maximum yield stress is employed for material plasticity, and the accumulated plastic strain is recorded on tracers and used to reduce the material friction coefficient and cohesion. Elasticity alters the stress within the slab, and we include a new visco-

elastic formulation called the Elastic Viscous Stress Splitting (EVSS) method (e.g., Keunings, 2000) in our model. Energy change with shear heating is treated as heat source terms and stored on tracers. Thermal and rheological parameters are given in Table S3.1.

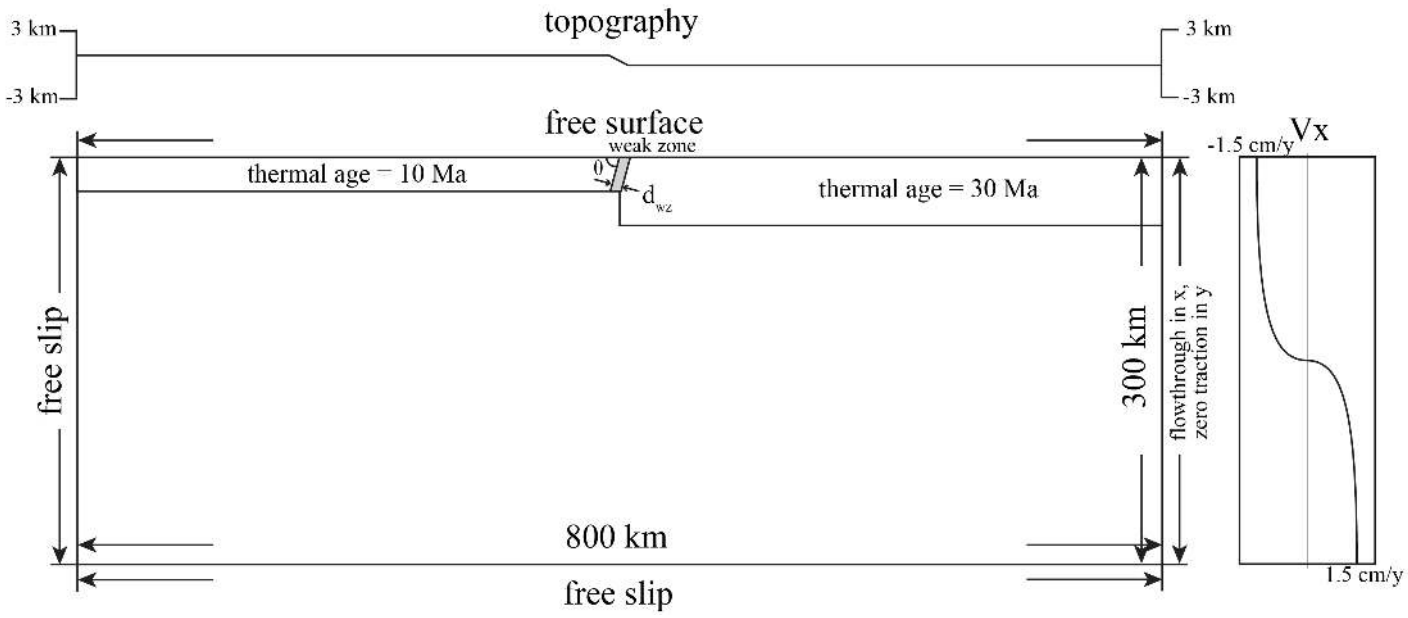

Figure 3.2: Model setup. The gray area show the shape of the weak zone, with dip angle, θ, and width, d_{wz}. The weak zone is initialized with random plastic strain within 0-0.4, while other material properties remain unchanged. The finest resolution is 1 km x 1 km near the subduction zone, and the lowest is 3 km x 3 km in the asthenosphere.

3.3 Results

The models we run are given in Table S3.2. We first show the detailed evolution of a subduction initiation case (SI1) that starts with a vertical weak zone with imposed far field plate velocities (Fig. 3.3), which are key aspects of PISZ. Initially (by 2.26 Myr), both the overriding and subducting plates are in a strong sense of compression, and the first lithospheric scale fault forms at the top of the initial weak zone with a high dip angle (fine structures shown in Fig. 3.4a). Displacement on this new fault is small, and wide spread shear bands together with buckling of the lithosphere develop within the overriding plate. The buckling and shear bands absorb a considerable amount of the convergence. Some strain begins to localize at a shear band on the subducting plate side, and this shear band connects to the deeper part of the initial weak zone (Fig. 3.4a). Responding to strong compression,

a topographic pair of uplift adjacent to subsidence appear near the plate boundary at the overriding and subducting sides respectively, and amplitudes of both are around 1.5 km (Fig. 3.3d). Topographic fluctuation on the order of a hundred meters is predicted due to the lithospheric buckling in the overriding plate (Fig. 3.3d). By 3.87 Myr, the shear band on the subducting plate side evolves into a new fault which later becomes the subduction interface. A $\sim$ 30 km wide triangular lithospheric block which was on the subducting plate attaches to the overriding plate with the formation of the new plate boundary. A two-fault system, with the main thrust fault at the subduction interface and a vertical fault inboard of the thrust fault, starts to appear and dominate the deformation and structure of the overriding plate close to the trench. A sharp topographic signal is manifest with the uplift and rotation of the triangular block. The rough subduction interface is slowly smoothed by continuous tectonic erosion and plate bending from 3.87 to 11.65 Myr. With smoothing, the compressive stress in the overriding plate decreases (Fig. 3.3c and Fig. 3.4c), and shear bands in the overriding plate become inactive (Fig. 3.3a). Topography of the overriding plate close to the trench changes from uplift to subsidence, and the trench depth deepens (Fig. 3.3d). The bending of the subducting plate causes near surface extension and compression deeper within the subducting lithosphere near the trench, which leads to development of the forebulge topography and normal faults in the upper part of the lithosphere. Interestingly, these normal faults become temporarily inactive after they pass the bending region and enter the subduction zone (Fig. 3.3a). Basalt transitions to eclogite at 70-80 km depth resulting in a density jump in the oceanic crust, and decoupling occurs between the overriding and subducting plates in the mantle wedge caused by released fluids. Both tend to bend the subducted slab to a higher dipping angle. A trough forms at the overriding plate close to the trench region when the slab reaches $\sim$ 200 km depth (Fig. 3.3d), and weak material consisting of sediments and crustal and lithospheric components (scrapped off along the interface) accumulate beneath the trough (Fig. 3.4a).

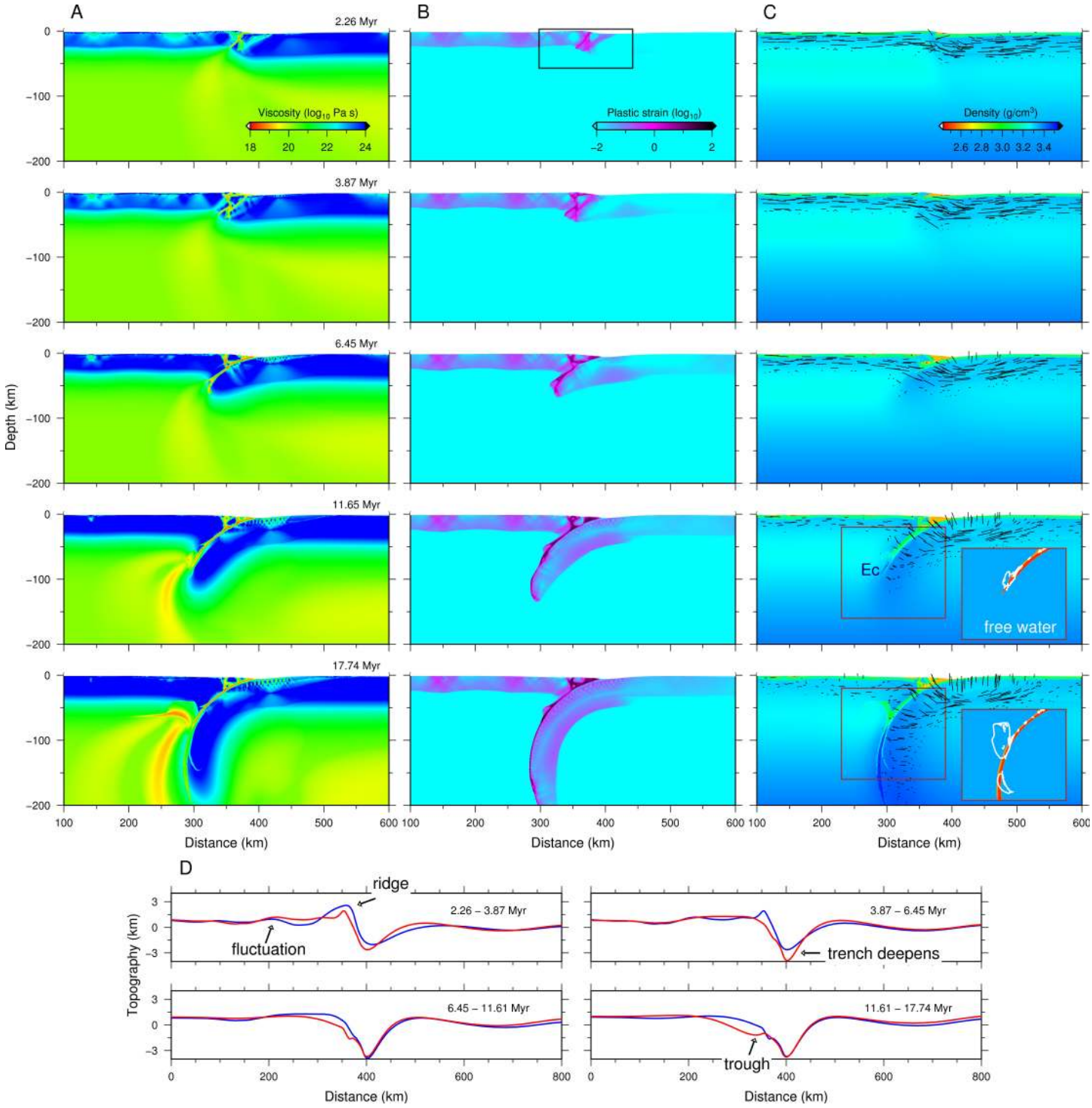

Figure 3.3: Model results (case SI1). (a) Effective viscosity evolution. (b) Accumulation of plastic strain. The black box shows the corresponding region for Figure 4a. (c) Density evolution. Black lines show direction and magnitude of maximum principal stress. Rock types and free water contents are shown in the insets with different colors and white contours. (d) Topography changes. Blue and red lines show initial and final topography for each time interval.

We compare this case with one with a 30° dip angle weak zone (Fig. S3.1). Initially, the subduction interface develops easily within the weak zone, and strain localizes to this thrust fault efficiently. The shape of the fault is favorable for subduction, and compression within the overriding plate decreases much faster compared to the case with a vertical weak zone. Only one fault develops during the entire subduction initiation process, and few shear bands appear during the early stage of compression. Lithospheric buckling of the overriding plate is absent in this case. The overriding plate close to the trench experiences uplift and subsidence during the initiation, while no trough-like structure develops. Unlike the vertical weak zone case, where the whole overriding plate is under weak compression or at a nearly neutral stress state after the smoothing of the subduction interface, the stress state in the overriding plate transitions into the extension phase quickly (Fig. 3.4c).

To fill the gap between the two end members of shallow and steep dipping weak zones, we computed three additional cases with dip angles of 45°, 60°, and 75° (Fig. S3.2-S3.4). These models can be divided into two categories: one starts with high dip angles and evolves to a two-fault system (Fig. 3.4a), while the other starts with a shallow dip and converges to a single-fault system (Fig. 3.4b). During initiation, resisting forces in the two-fault system are at higher stress level, and the compression in the overriding plate can last much longer compared to the single-fault system (Fig. 3.4c).

To test the other geometrical parameter that may influence the fault structure during subduction initiation, we conduct two more cases, varying the width of the weak zone with a 90° dip angle (Fig. S3.5-S3.6). With a wider weak zone, the evolution pathway is generally similar to case SI1. The main differences are the triangular block between the thrust and vertical faults becomes smaller and the compressive stress within the overriding plate is at a slightly lower level. With half the width of the initial weak zone, the model fails to localize the deformation near the plate boundary. These two models confirm that once the weak zone is wide enough to localize the initial deformation, the dip angle plays a more important role in determining if a new fault is needed to initiate subduction.

In the previous cases, we focus on the influence of weak zone geometry on fault structure and stress state within the lithosphere during subduction initiation under compression, and we ignore a harzburgite layer in our density structure for simplicity (Fig. S3.7). However, harzburgite has a slightly lower density compared to the undepleted mantle, and could increase resisting forces for slab subduction (e.g.,

Oxburgh and Parmentier, 1977; Arrial and Billen, 2013). Therefore, we compare another case that incorporates a 15 km thick harzburgite layer beneath the crust (Fig. S3.8) to case SI1 to test how this simplification affects our results. As we can see, these two cases give very similar model predictions on fault structure and topographic evolution (Fig. 3.3 and Fig. S3.8), while the transition from compression to extension happens later with the addition of harzburgite (Fig. 3.4c). This additional case suggests that during induced subduction initiation, early resistance mainly comes from friction on the plate interface and bending of the plates, while when slab approaches the transition threshold, positive buoyancy from chemical heterogeneities becomes important.

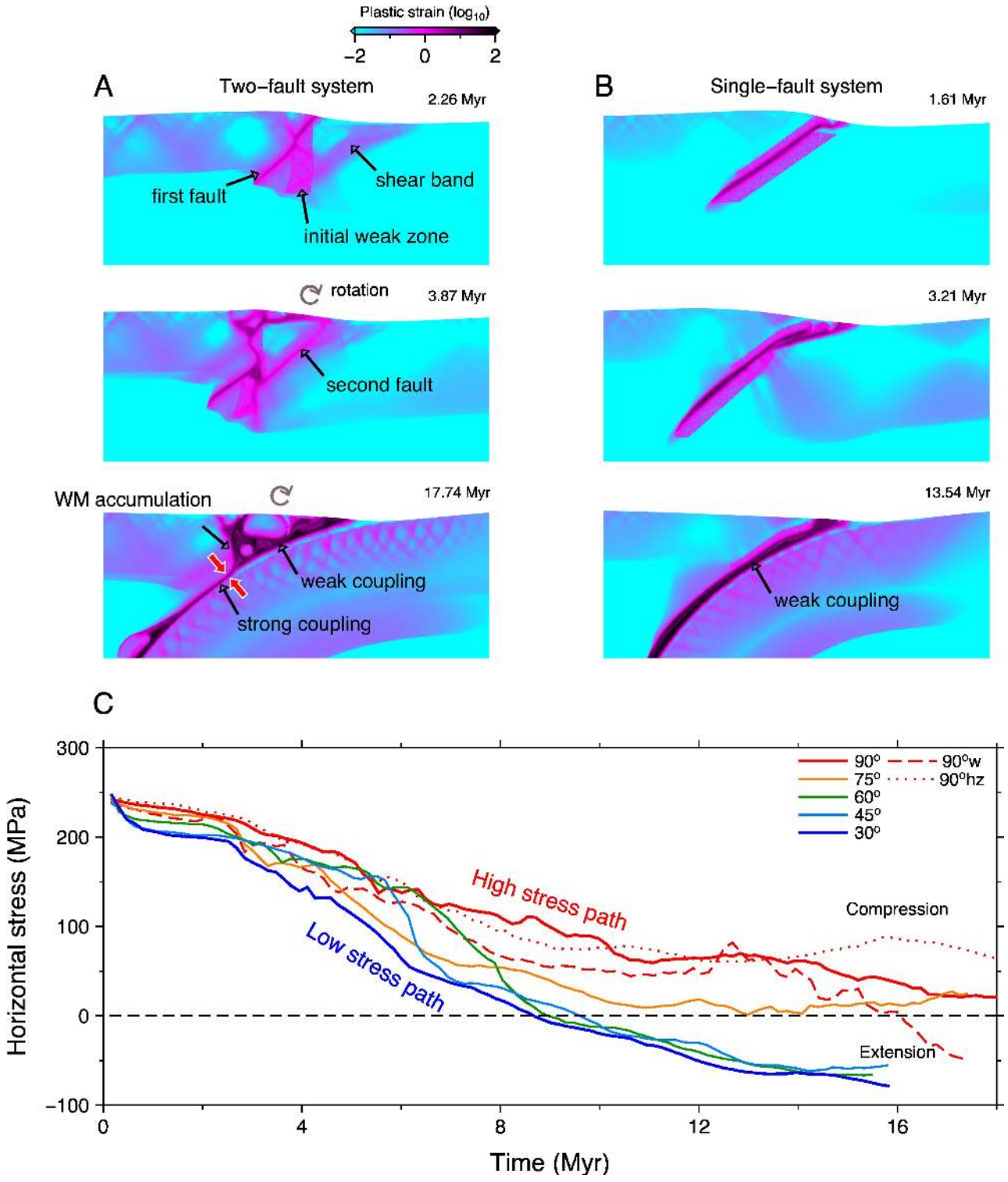

Figure 3.4: Model summary. (a), (b) are zoomed in plastic strains for case SI1 and SI2 respectively. WM: weak material. (c) Averaged horizontal stresses within overriding plate for different cases. The averaging is performed within the region that spans from 100 km to 300 km distance and from surface to 25 km depth.

3.4 Discussion and Conclusions

Although the strike-slip motion on the Puysegur Fault is ignored in our 2D model, our model predictions from case SI1 are generally consistent with field observations at PISZ. The uplift and subsidence of the topography on the overriding plate close to the trench agree with the uplift of the Puysegur Ridge in the south and uplift followed by subsidence in the north. The predicted trough has the similar distance to the trench as in the Snares Zone. The trench depth increase during the smoothing and maturation of the new thrust fault fits the depth difference between the southern and northern parts of the Puysegur Trench (~1000 m). The buckling and shear bands that develop during the new fault formation are consistent with the renewed folding and reverse faulting on structures subparallel to the plate boundary on the overriding plate in the PISZ (Sutherland et al., 2006). More importantly, the predicted two-fault system, where a main thrust fault at the subduction interface and a vertical fault inboard of the thrust fault, is consistent with the Puysegur Trench and Fault structure.

Previous studies (Gurnis et al., 2004; Leng and Gurnis, 2011) suggest that the transition in the force balances from being forced externally to a state of self-sustaining subduction happens after a critical convergence is reached for induced subduction initiation, and the critical value is influenced by plastic parameters. Our results show that this transition is also affected by fault structures in two ways: one is through the development of the two-fault system, which absorbs some convergence and delays the transition; the other is more complex and related to the plate coupling difference between shallower and deeper parts. The rotation of the tectonic sliver between two faults causes the accumulation of weak materials beneath it, which results in a wider weak zone and a weaker plate coupling in the shallower part and a narrower weak zone and a stronger plate coupling in the deeper part. This coupling difference leads to a weak compression at the deeper part of the slab interface, which also contributes to a delay in the transition. We suggest that the PISZ may have not yet reached a state of self-sustaining subduction, and the subsidence at the overriding plate close to the trench may not be a direct proxy for the transition in the force balances. The Snares Zone may form through an isostatic response to tectonic erosion of a crustal root or pull by negative slab buoyancy, or both (Sutherland et al., 2006). Here, we suggest the opening of the trough maybe caused by the surficial extension resulting from the combined effects of the deeper compression between two plates and the rotation of the tectonic sliver. Our prediction of low density material beneath the trough also helps to explain the strong (-110 mGal) localized

low gravity anomaly at the Snares Zone, which is difficult to explain by subsidence alone (Lamarche and Lebrun, 2000).

In conclusion, our model motivated from the geological setting (Collot et al., 1995) requires a simpler initial condition, one weak zone instead of two, and gives more detailed explanation for the formation of the two-fault system at PISZ. Our model also provides important insights into how subduction initiates at fracture zones and transform faults, where the initial weak zone may have mechanically unfavorable dip angles.

Acknowledgements

X. M. and M. G. were supported by the National Science Foundation through awards EAR-1247022, EAR-1645775, and OCE-1654766. D. A. M. acknowledges financial support from the European Research Council under the European Union's Seventh Framework Programme (FP7/2007-2013)/ERC Grant Agreement 279925. Computations carried out on the NSF XSEDE systems, made possible by TG-EAR160027.

3.5 Appendix: Supplementary materials for Chapter 3

Table S3.1: Thermal and rheological parameters

Parameter	Value
surface temperature	0 °C
bottom temperature	1400 °C
thermal diffusivity (κ)	10^{-6} m^2 s^{-1}
maximum viscosity cutoff (η_{max})	10^{24} Pa s
minimum viscosity cutoff (η_{min})	10^{18} Pa s
shear modulus (G)	30 GPa
maximum yield stress (τ_{yield})	150 MPa
initial water content in mantle	100 ppm
preexponential factor in mantle (A_m)	1.6 x 10^{-15} Pa^{-n} s^{-1}
exponent in mantle (n_m)	3.2
activation energy in mantle (E_m)	540 kJ mol^{-1}
initial water content in crust	2.68%
preexponential factor in crust (A_c)	2 x 10^{-23} Pa^{-n} s^{-1}
exponent in crust (n_c)	3.2
activation energy in crust (E_c)	238 kJ mol^{-1}
initial water content in sediment	7.29%
preexponential factor in sediment (A_s)	5 x 10^{-21} Pa^{-n} s^{-1}
exponent in sediment (n_s)	2.3
activation energy in sediment (E_s)	154 kJ mol^{-1}

Table S3.2: Table of models. WZ is short for weak zone.

Model	WZ dip angle	WZ width	Harzburgite layer
SI1	90°	10 km	No
SI2	30°	10 km	No
SI3	45°	10 km	No
SI4	60°	10 km	No
SI5	75°	10 km	No
SI6	90°	15 km	No
SI7	90°	5 km	No
SI8	90°	10 km	15 km

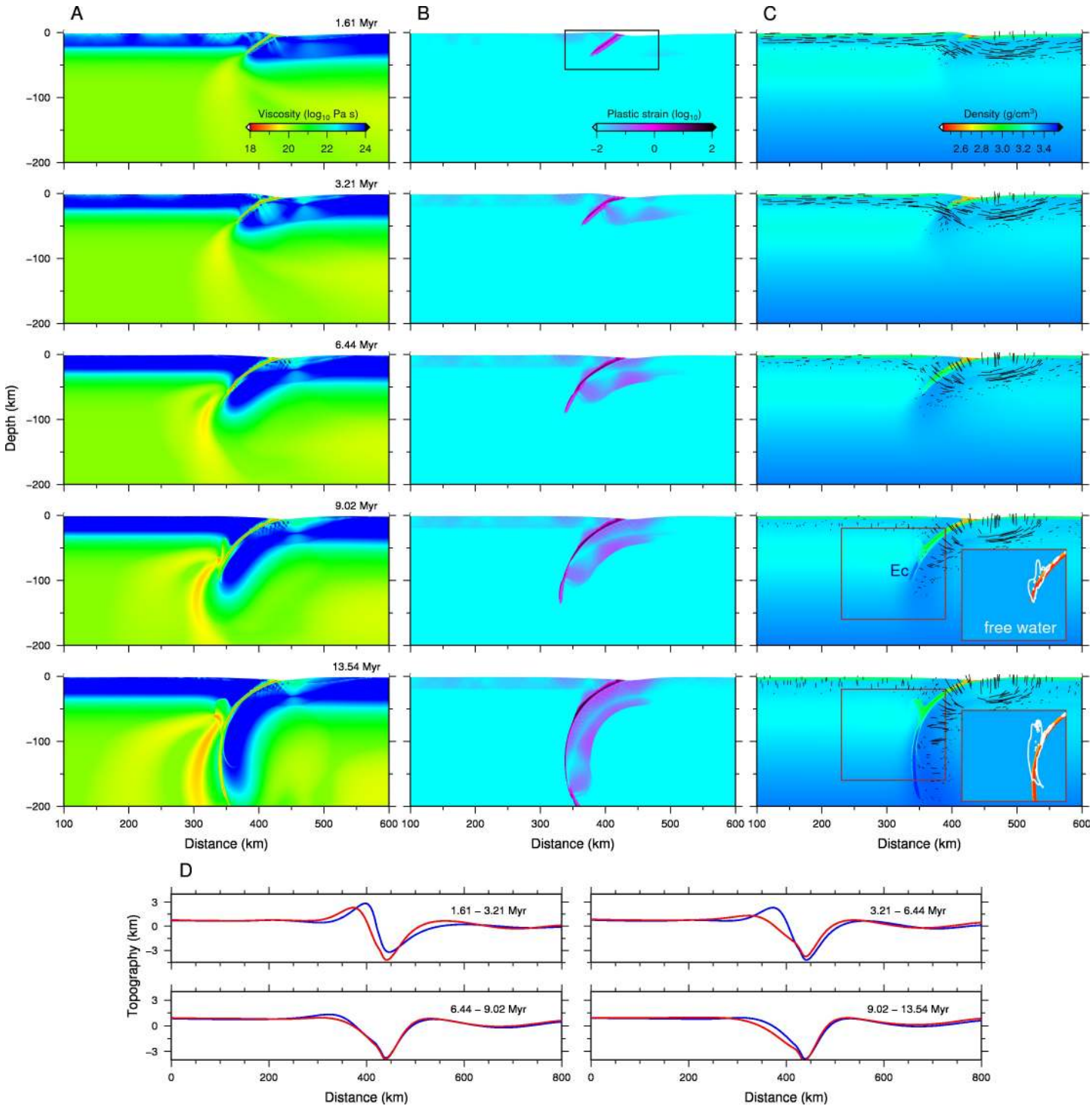

Figure S3.1: Model results (case SI2). (a) Effective viscosity evolution. (b) Accumulation of plastic strain. The black box shows the corresponding region for Figure 4b. (c) Density evolution. Black lines show direction and magnitude of maximum principal stress. Rock types and free water contents are shown in the insets with different colors and white contours. (d) Topography changes. Blue and red lines show initial and final topography for each time interval.

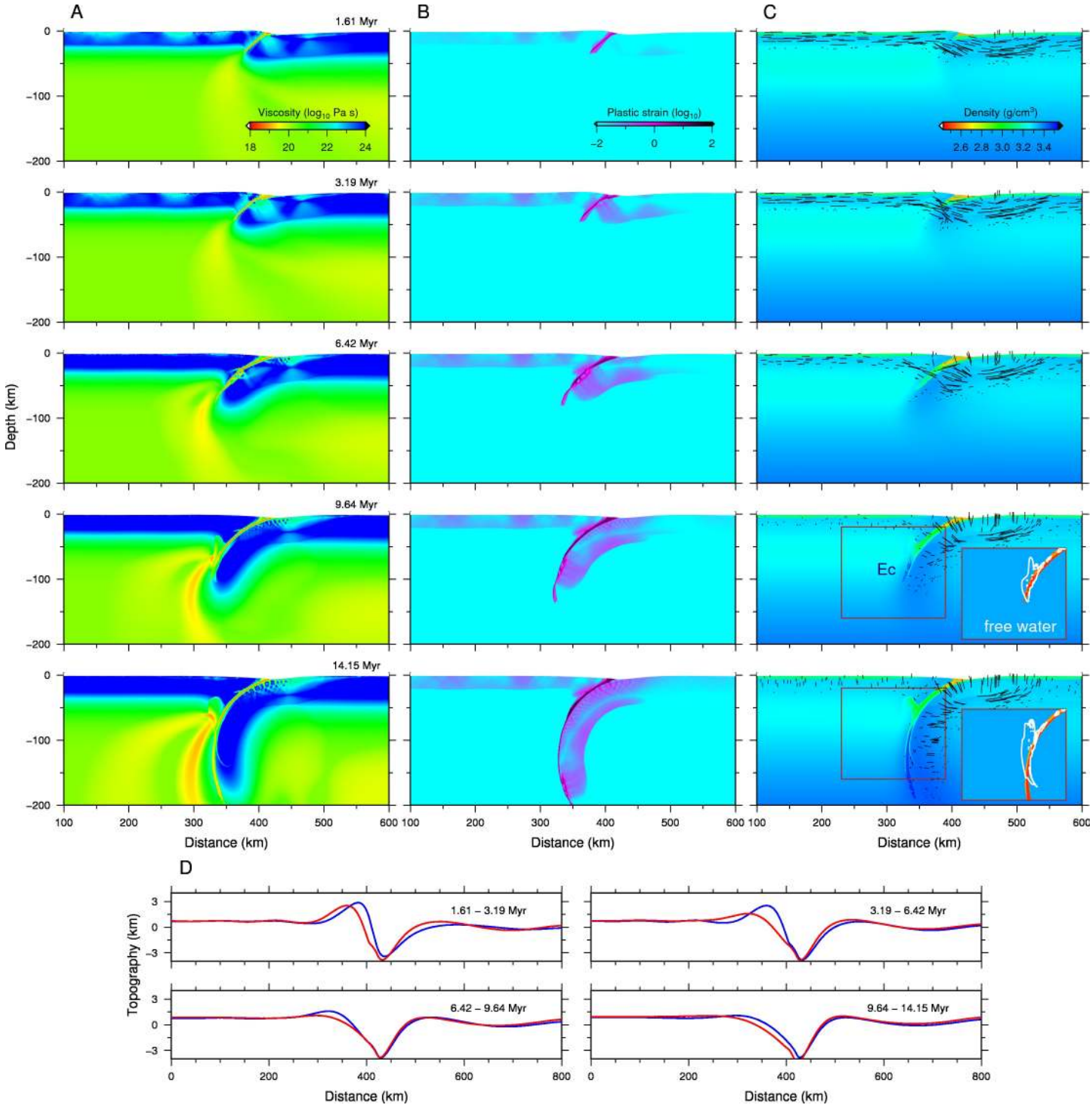

Figure S3.2: Model results (case SI3). (a) Effective viscosity evolution. (b) Accumulation of plastic strain. (c) Density evolution. Black lines show direction and magnitude of maximum principal stress. Rock types and free water contents are shown in the insets with different colors and white contours. (d) Topography changes. Blue and red lines show initial and final topography for each time interval.

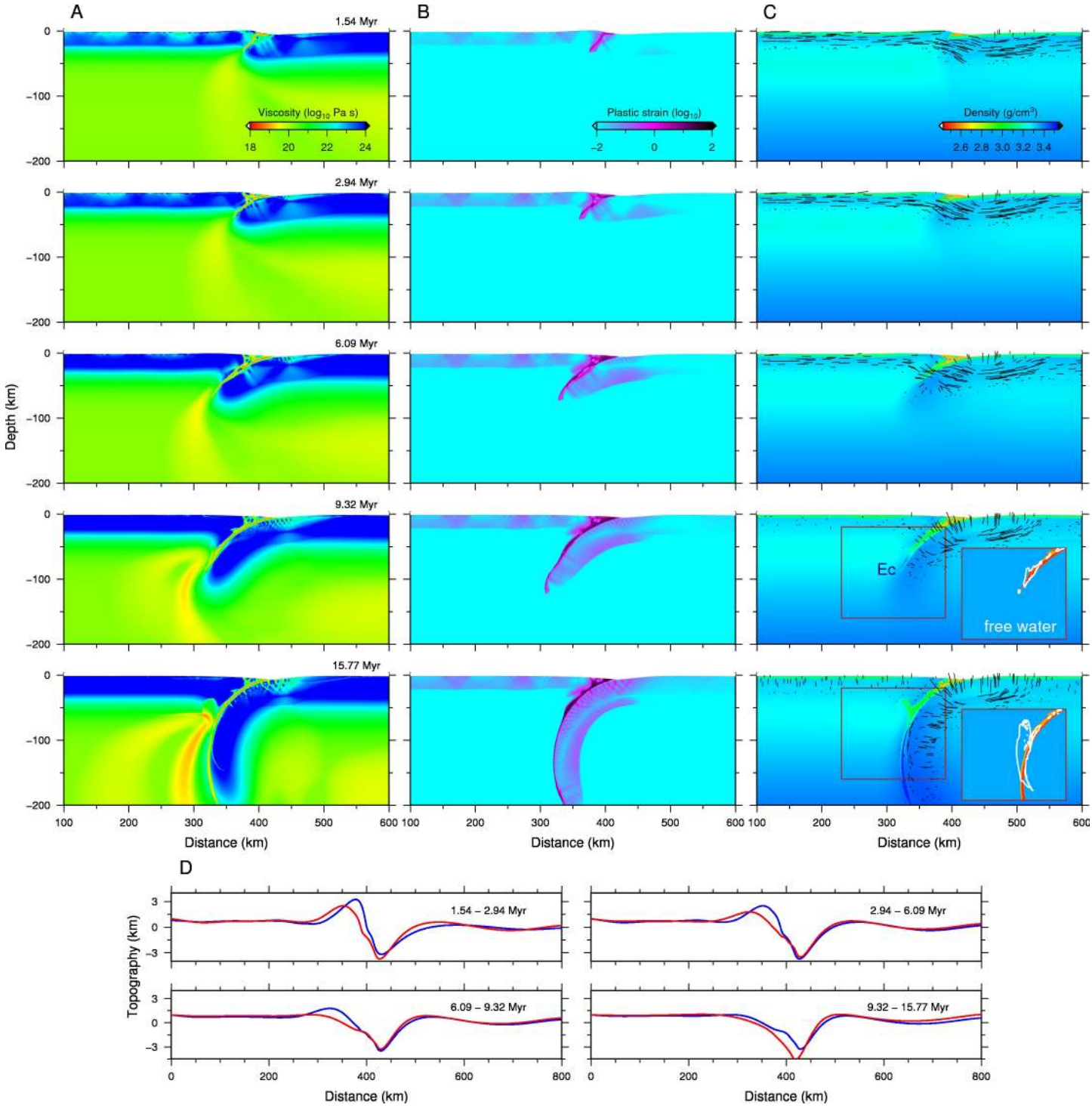

Figure S3.3: Model results (case SI4). (a) Effective viscosity evolution. (b) Accumulation of plastic strain. (c) Density evolution. Black lines show direction and magnitude of maximum principal stress. Rock types and free water contents are shown in the insets with different colors and white contours. (d) Topography changes. Blue and red lines show initial and final topography for each time interval.

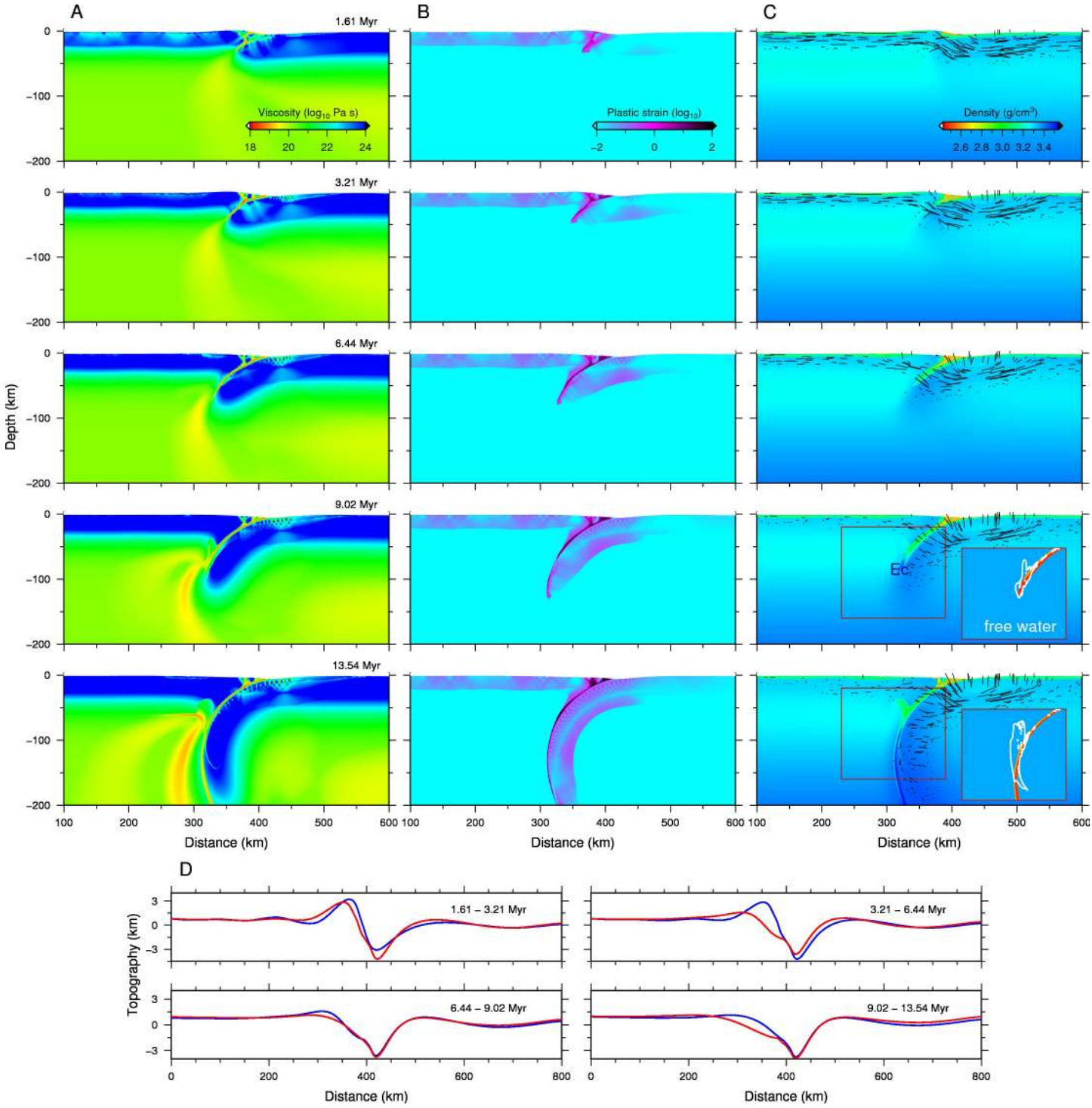

Figure S3.4: Model results (case SI5). (a) Effective viscosity evolution. (b) Accumulation of plastic strain. (c) Density evolution. Black lines show direction and magnitude of maximum principal stress. Rock types and free water contents are shown in the insets with different colors and white contours. (d) Topography changes. Blue and red lines show initial and final topography for each time interval.

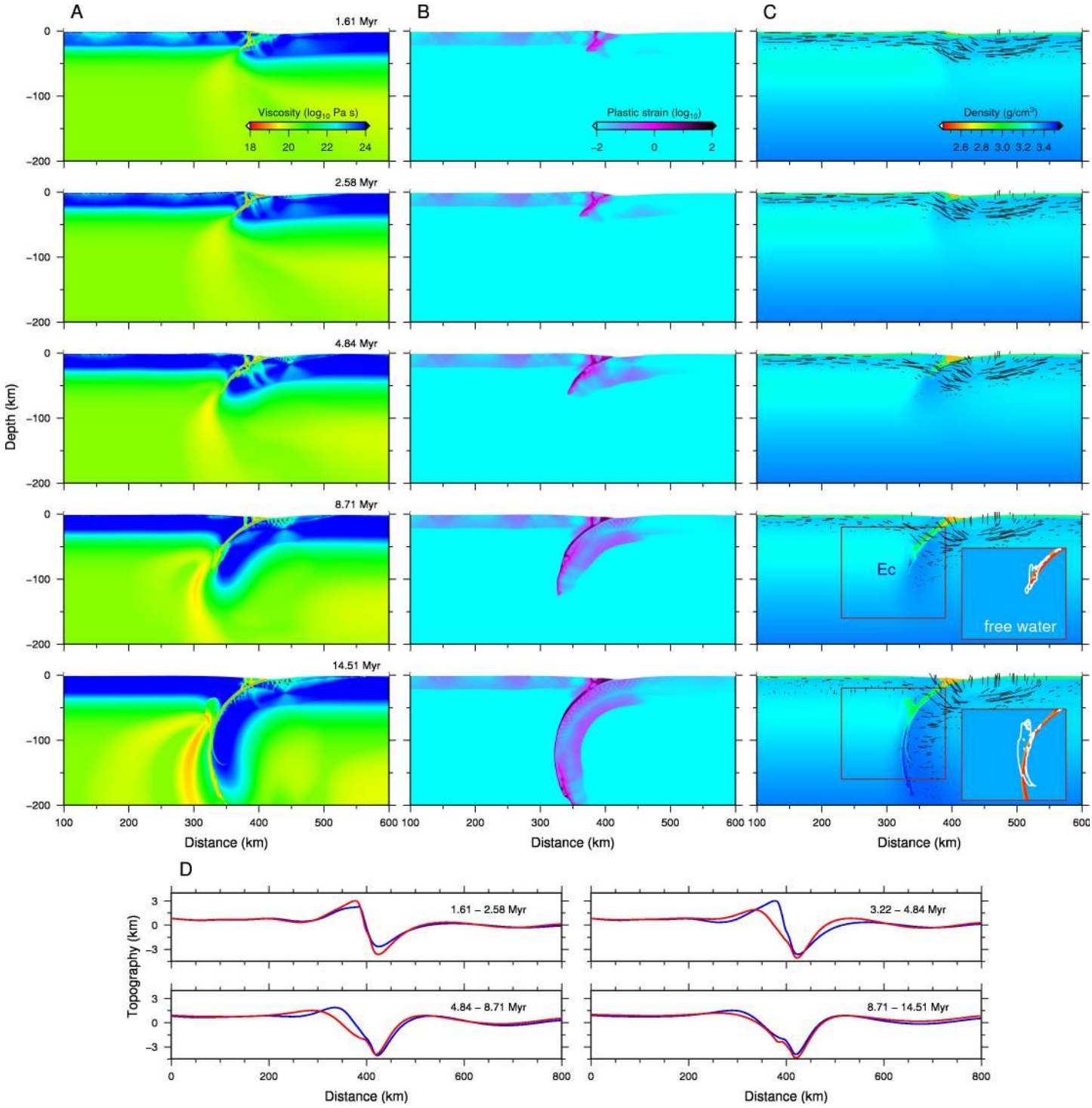

Figure S3.5: Model results (case SI6). (a) Effective viscosity evolution. (b) Accumulation of plastic strain. (c) Density evolution. Black lines show direction and magnitude of maximum principal stress. Rock types and free water contents are shown in the insets with different colors and white contours. (d) Topography changes. Blue and red lines show initial and final topography for each time interval.

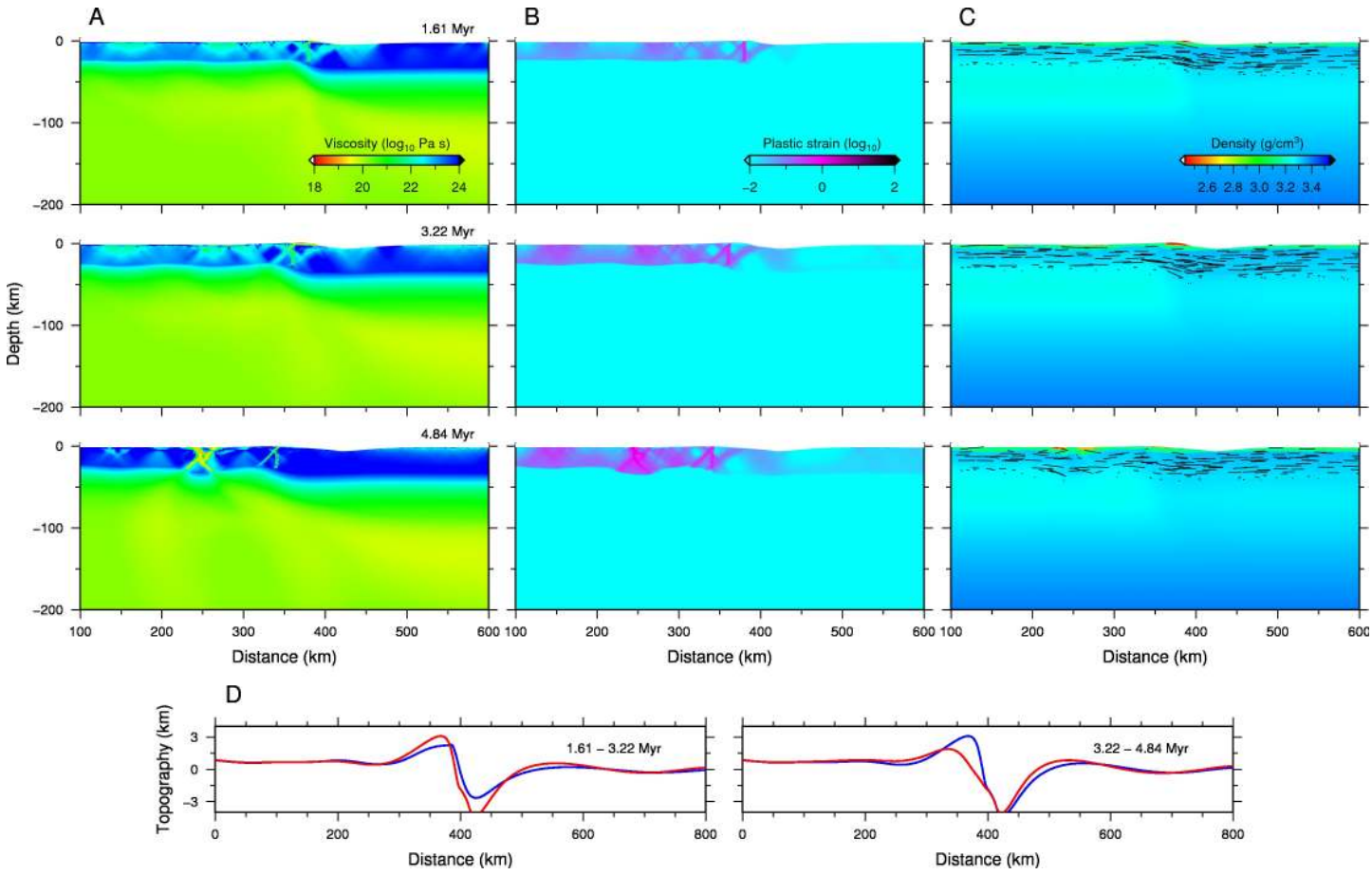

Figure S3.6: Model results (case SI7). (a) Effective viscosity evolution. (b) Accumulation of plastic strain. (c) Density evolution. Black lines show direction and magnitude of maximum principal stress. (d) Topography changes. Blue and red lines show initial and final topography for each time interval.

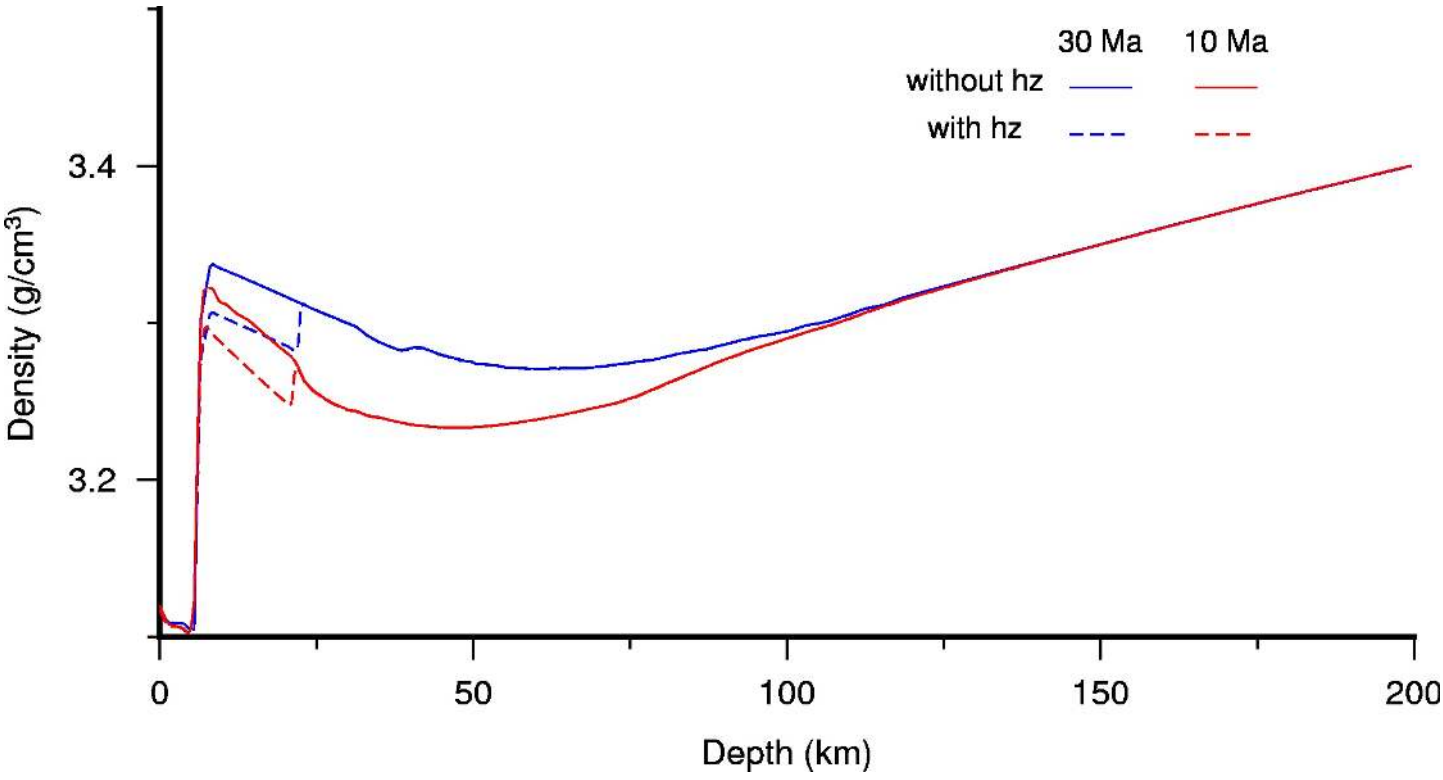

Figure S3.7: Along depth variation of initial density structure. hz: harzburgite.

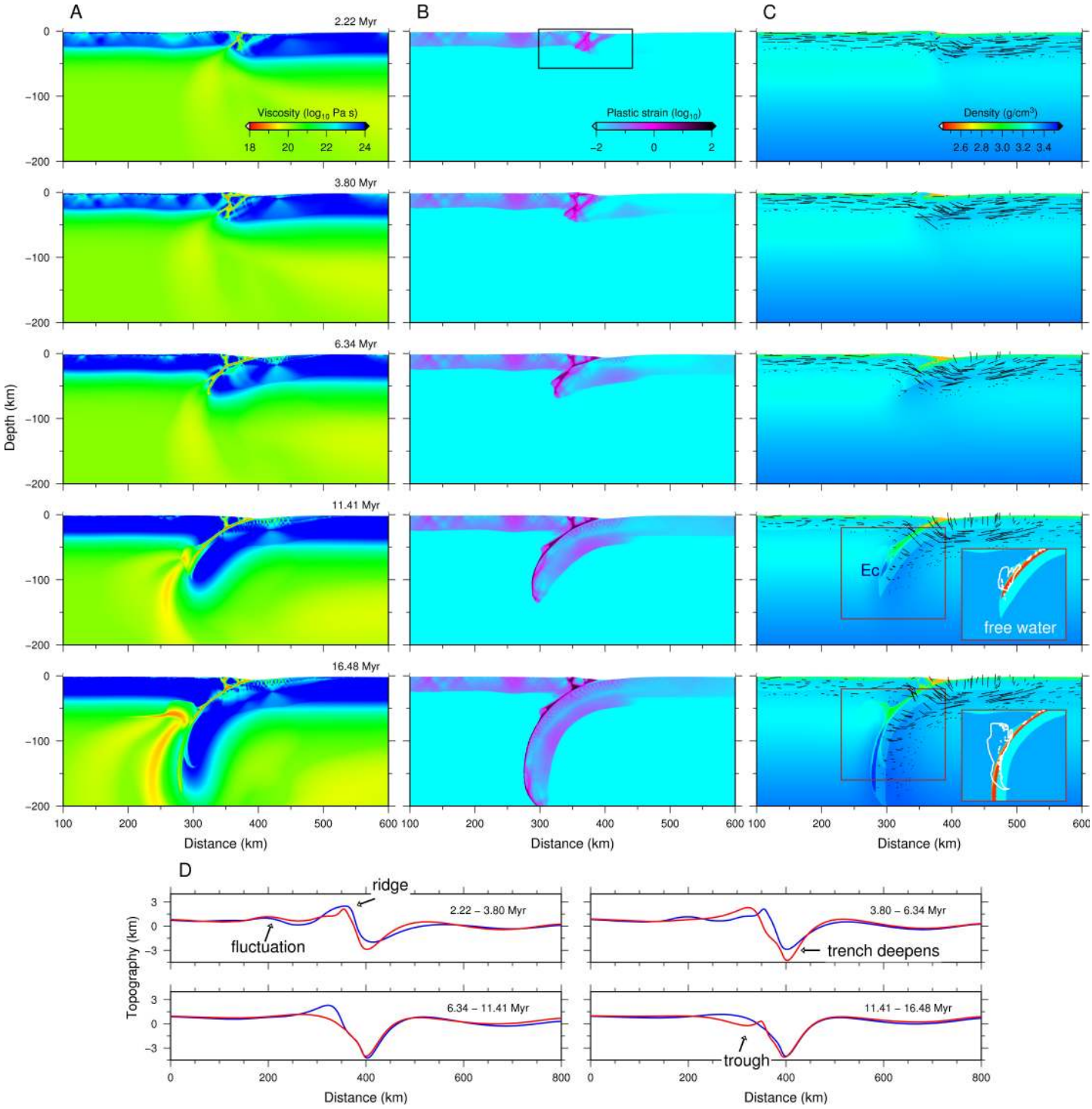

Figure S3.8: Model results of a case with a 15 km Harzburgite layer (case SI8). (a) Effective viscosity evolution. (b) Accumulation of plastic strain. (c) Density evolution. Black lines show direction and magnitude of maximum principal stress. (d) Topography changes. Blue and red lines show initial and final topography for each time interval.

References

Arrial, Pierre-André and Magali I Billen (2013). Influence of geometry and eclogitization on oceanic plateau subduction. *Earth and Planetary Science Letters*, 363:34–43.

Avouac, J-Ph and EB Burov (1996). Erosion as a driving mechanism of intracontinental mountain growth. *Journal of Geophysical Research: Solid Earth*, 101 (B8):17747–17769. doi: 10.1029/96JB01344.

Billen, Magali I and Michael Gurnis (2001). A low viscosity wedge in subduction zones. *Earth and Planetary Science Letters*, 193(1):227–236. doi: 10.1016/S0012-821X(01)00482-4.

Collot, Jean-Yves, Geoffroy Lamarche, Ray A Wood, Jean Delteil, Marc Sosson, Jean-Frédéric Lebrun, and Mike F Coffin (1995). Morphostructure of an incipient subduction zone along a transform plate boundary: Puysegur Ridge and Trench. *Geology*, 23(6):519–522. doi: 10.1130/0091-7613(1995)023<0519:MOAISZ>2.3.CO;2.

Connolly, James AD (2005). Computation of phase equilibria by linear programming: a tool for geodynamic modeling and its application to subduction zone decarbonation. *Earth and Planetary Science Letters*, 236(1):524–541. doi: 10.1016/j.epsl.2005.04.033.

DeMets, Charles, Richard G Gordon, Donald F Argus, and Seth Stein (1994). Effect of recent revisions to the geomagnetic reversal time scale on estimates of current plate motions. *Geophysical research letters*, 21(20):2191–2194. doi: 10.1029/94GL02118.

Dziewonski, AM, T-A Chou, and JH Woodhouse (1981). Determination of earthquake source parameters from waveform data for studies of global and regional seismicity. *Journal of Geophysical Research: Solid Earth*, 86(B4):2825–2852. doi: 10.1029/JB086iB04p02825.

Gerya, Taras V and FI Meilick (2011). Geodynamic regimes of subduction under an active margin: effects of rheological weakening by fluids and melts. *Journal of Metamorphic Geology*, 29(1):7–31. doi: 10.1111/j.1525-1314.2010.00904.x.

Gurnis, Michael, Chad Hall, and Luc Lavier (2004). Evolving force balance during incipient subduction. *Geochemistry, Geophysics, Geosystems*, 5(7). doi: 10.1029/2003GC000681.

Hirth, Greg and David L Kohlstedt (1996). Water in the oceanic upper mantle: implications for rheology, melt extraction and the evolution of the lithosphere. *Earth and Planetary Science Letters*, 144(1-2):93–108. doi: 10.1016/0012-821X(96)00154-9.

International Seismological Centre (2014). *On-line Bulletin*. Internatl. Seismol. Cent., Thatcham, United Kingdom. http://www.isc.ac.uk.

Kaus, Boris JP, Clare Steedman, and Thorsten W Becker (2008). From passive continental margin to mountain belt: insights from analytical and numerical models and application to Taiwan. *Physics of the Earth and Planetary Interiors*, 171(1):235–251. doi: 10.1016/j.pepi.2008.06.015.

Kaus, Boris JP, Hans Mühlhaus, and Dave A May (2010). A stabilization algorithm for geodynamic numerical simulations with a free surface. *Physics of the Earth and Planetary Interiors*, 181(1):12–20. doi: 10.1016/j.pepi.2010.04.007.

Keunings, R (2000). Advances in the computer modeling of the flow of polymetric liquids. *Computational Fluid Dynamics Journal*, 9(1):449–458.

Lamarche, Geoffroy and Jean-Frédéric Lebrun (2000). Transition from strike-slip faulting to oblique subduction: active tectonics at the Puysegur Margin, South New Zealand. *Tectonophysics*, 316(1):67–89. doi: 10.1016/S0040-1951(99)00232-2.

Lebrun, Jean-Frédéric, Garry D Karner, and Jean-Yves Collot (1998). Fracture zone subduction and reactivation across the Puysegur ridge/trench system, southern New Zealand. *Journal of Geophysical Research: Solid Earth*, 103(B4):7293–7313. doi: 10.1029/98JB00025.

Leng, Wei and Michael Gurnis (2011). Dynamics of subduction initiation with different evolutionary pathways. *Geochemistry, Geophysics, Geosystems*, 12(12). doi: 10.1029/2011GC003877.

May, Dave A, Jed Brown, and Laetitia Le Pourhiet (2014). ptatin3d: High-performance methods for long-term lithospheric dynamics. In *Proceedings of the International Conference for High Performance Computing, Networking, Storage and Analysis*, pages 274–284. IEEE Press. doi: 10.1109/SC.2014.28.

May, David A, Jed Brown, and Laetitia Le Pourhiet (2015). A scalable, matrix-free multigrid preconditioner for finite element discretizations of heterogeneous Stokes flow. *Computer Methods in Applied Mechanics and Engineering*, 290:496–523. doi: 10.1016/j.cma.2015.03.014.

McKenzie, DP (1977). The initiation of trenches. *Island arcs, deep sea trenches and back-arc basins*, pages 57–61. doi: 10.1029/ME001p0057.

Nikolaeva, K, TV Gerya, and FO Marques (2010). Subduction initiation at passive margins: numerical modeling. *Journal of Geophysical Research: Solid Earth*, 115(B3). doi: 10.1029/2009JB006549.

Oxburgh, ER and EM Parmentier (1977). Compositional and density stratification in oceanic lithosphere-causes and consequences. *Journal of the Geological Society*, 133(4):343–355.

Reay, A and D Parkinson (1997). Adakites from Solander Island, New Zealand. *New Zealand journal of Geology and Geophysics*, 40(2):121–126. doi: 10.1080/00288306.1997.9514746.

Regenauer-Lieb, Klaus, Dave A Yuen, and Joy Branlund (2001). The initiation of subduction: criticality by addition of water? *Science*, 294(5542):578–580. doi: 10.1126/science.1063891.

Ruff, Larry J, Jeffrey W Given, Chris O Sanders, and Christine M Sperber (1989). Large earthquakes in the Macquarie Ridge Complex: transitional tectonics and subduction initiation. *Pure and Applied Geophysics*, 129(1-2):71–129.

Stern, Robert J (2004). Subduction initiation: spontaneous and induced. *Earth and Planetary Science Letters*, 226(3):275–292. doi: 10.1016/j.epsl.2004.08.007.

Sutherland, Rupert, Philip Barnes, and Chris Uruski (2006). Miocene-Recent deformation, surface elevation, and volcanic intrusion of the overriding plate during subduction initiation, offshore southern Fiordland, Puysegur margin, southwest New Zealand. *New Zealand Journal of Geology and Geophysics*, 49(1):131–149. doi: 10.1080/00288306.2006.9515154.

Thielmann, Marcel and Boris JP Kaus (2012). Shear heating induced lithospheric-scale localization: Does it result in subduction? *Earth and Planetary Science Letters*, 359:1–13. doi: 10.1016/j.epsl.2012.10.002.

Toth, John and Michael Gurnis (1998). Dynamics of subduction initiation at preexisting fault zones. *Journal of Geophysical Research: Solid Earth*, 103(B8):18053–18067. doi: 10.1029/98JB01076.

Zhong, Shijie and Michael Gurnis (1994). Controls on trench topography from dynamic models of subducted slabs. *Journal of Geophysical Research: Solid Earth*, 99(B8):15683–15695. doi: 10.1029/94JB00809.

Chapter 4

UPPER LIMIT ON DAMAGE ZONE THICKNESS CONTROLLED BY SEISMOGENIC DEPTH

Ampuero, Jean Paul and Xiaolin Mao (2017). Upper limit on damage zone thickness controlled by seismogenic depth. *Fault Zone Dynamic Processes: Evolution of Fault Properties During Seismic Rupture*, 227:243. doi: 10.1002/9781119156895.ch13.

The thickness of fault damage zones, a characteristic length of the cross-fault distribution of secondary fractures, significantly affects fault stress, earthquake rupture, ground motions, and crustal fluid transport. Field observations indicate that damage zone thickness scales with accumulated fault displacement at short displacements but saturates at a few hundred meters for displacements larger than a few kilometers. To explain this transition of scaling behavior, we conduct 3D numerical simulations of dynamic rupture with off-fault inelastic deformation on long strike-slip faults. We find that the distribution of coseismic inelastic strain is controlled by the transition from crack-like to pulse-like rupture propagation associated with saturation of the seismogenic depth. The yielding zone reaches its maximum thickness when the rupture becomes a stable pulse-like rupture. Considering fracture mechanics theory, we show that seismogenic depth controls the upper bound of damage zone thickness on mature faults by limiting the efficiency of stress concentration near earthquake rupture fronts. We obtain a quantitative relation between limiting damage zone thickness, background stress, dynamic fault strength, off-fault yield strength, and seismogenic depth, which agrees with first-order field observations. Our results help link dynamic rupture processes with field observations and contribute to a fundamental understanding of damage zone properties.

4.1 Introduction

A typical fault zone architecture comprises a highly deformed core surrounded by a damage zone composed of rocks with higher fracture density and lower elastic moduli than the host rocks. In most mature faults, damage zones are 100 to 400 m wide and have between 20% and 60% wave velocity reductions relative to their country rock (e.g., Huang and Ampuero, 2011). Studying the formation of damage

zones provides insight into the mechanical, hydraulic, and seismic behavior of faults. Fault zone damage is in part inherited from the early process of fracture coalescence and strain localization that led to the formation of the fault, and in part results from damage during earthquakes (Mitchell and Faulkner, 2009). Damage zone thickness, defined as a characteristic scale of the cross-fault distribution of fracture density, varies from a few centimeters on small faults to a few hundred meters on large mature faults. Field observations indicate that damage zone thickness scales with accumulated fault displacement, which is a measure of fault maturity, but generally saturates at a few hundred meters for fault displacements larger than a few km (Mitchell and Faulkner, 2009; Savage and Brodsky, 2011). Explaining this transition of scaling behavior is the main goal of the present work.

Understanding what controls damage zone thickness is important because this parameter can have significant effects on earthquake rupture, seismic wave radiation, and state of stress and hydromechanical properties of the crust. The transition from damage zone to country rock is often sharp, marked by a change of decay rate of fracture density as a function of distance to the fault core (Johri et al., 2014b). Earthquakes happening inside damage zones can thus generate reflected waves and head waves, which can enhance ground motion near the fault (Spudich and Olsen, 2001) but also interact with earthquake ruptures and modulate rupture properties such as rupture speed, slip rate, and rise time (Huang et al., 2014; Pelties et al., 2015). In particular, seismological evidence of rupture speeds enhanced by fault zone effects was recently presented (Huang et al., 2016; Perrin et al., 2016a). Damage zones may also alter the stress field surrounding faults, leading to mean stress increase and stress rotations, thereby allowing high pore fluid pressure weakening of unfavorably oriented faults (Faulkner et al., 2006). The effect of reduced elastic moduli in damage zones and their systematic changes along strike induced by fault growth help explain patterns of long-term fault displacement and earthquake slip distributions (Cappa et al., 2014; Perrin et al., 2016a). Damage zone thickness is also an important factor affecting the fluid transport and storage properties of the crust and reservoirs (Johri et al., 2014b).

Off-fault inelastic deformation is observed all along the rupture trace of large earthquakes (Milliner et al., 2015), demonstrating the importance of damage generated coseismically in the vicinity of propagating rupture fronts. Off-fault yielding during dynamic rupture propagation has been previously studied through analytical approaches (Poliakov et al., 2002; Rice et al., 2005) and numerical simulations with

off-fault plasticity (e.g., Andrews, 1976a, 2005; Gabriel et al., 2013) or continuum damage (Xu et al., 2015). Plastic strain is often discussed as a proxy for damage (e.g., Xu et al., 2012a,b) and can be mapped into fracture density for comparison with field observations (Johri et al., 2014a). The thickness of the off-fault yielding zone generated by a single self-similar rupture (crack-like or pulse-like) increases linearly with distance from the hypocenter (Andrews, 2005; Gabriel et al., 2013). In contrast, the yielding zone thickness generated by steady-state pulse-like ruptures remains constant (Ben-Zion and Shi, 2005; Ben-Zion and Ampuero, 2009; Xu et al., 2012a,b). The accumulated effect of multiple slip events can be considered as a superposition of the coseismic plastic strain fields of each individual slip event (Johri et al., 2014a). Most previous numerical studies of coseismic damage are based on 2D models or on 3D models of relatively short ruptures (Ma and Andrews, 2010), and are unable to consider the influence of the aspect ratio of a rupture, i.e., the ratio of its along-strike length to along-dip width. A notable exception are the 3D simulations of long ruptures by Shi and Day (2013), which yielded an eventually stable thickness of the off-fault plastic zone. As proposed by Day (1982) on the basis of an asymptotic analysis of stress concentration near a 3D rupture front, the inelastic deformation induced by a rupture with high aspect ratio is controlled by width rather than length.

In this study, we use 3D numerical simulations of dynamic rupture on strike-slip faults with large aspect ratios to study first-order aspects of the off-fault yielding pattern in long faults. In particular, we assess the role of seismogenic depth in limiting fault zone width. The ingredients of our model, described in Section 4.2, are intentionally minimalistic: material properties surrounding the fault are uniform, a linear slip-weakening friction law is assumed on the fault. In Section 4.3, comparing results of simulations with different seismogenic depths, we find that the distribution of inelastic strain is controlled by the transition from crack-like to pulse-like rupture propagation associated with saturation of the seismogenic depth. The yielding zone reaches its maximum thickness when the rupture becomes a stable pulse-like rupture. In Section 4.4 we develop quantitative insight, from the perspective of fracture mechanics, on how the transition to pulse-like rupture in long faults explains the saturation of damage zone thickness with accumulated fault displacement. In particular, we show that seismogenic depth controls the upper limit of damage zone thickness on mature faults. In Section 4.5 we discuss how our results help link dynamic rupture models with field observations, and contribute to a fundamental understanding of damage zone properties.

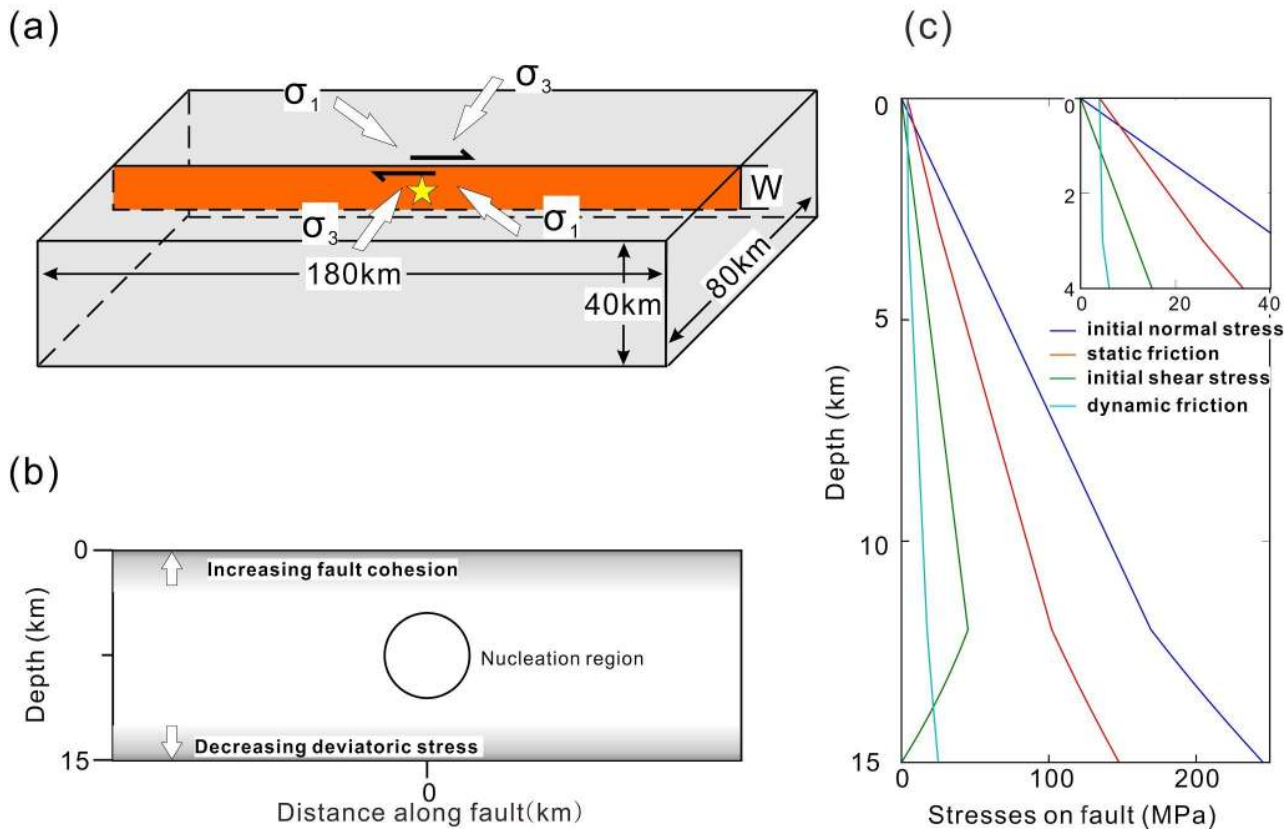

Figure 4.1: Model setup. (a) Model geometry and background stresses. σ_1 and σ_3 are maximum and minimum principal initial stresses, respectively. The angle between σ_1 and the fault strike is 30.96° and the intermediate principal stress is vertical. The seismogenic zone depth is denoted by W. (b) Fault plane view showing the nucleation zone (circle), a shallow zone of increased cohesion and a deep zone of tapered stressed. (c) Initial stresses and frictional strength on the fault as a function of depth.

4.2 Model description

The geometry of our numerical model is shown in Fig. 4.1(a). The fault is long enough (along strike) for dynamic rupture to reach an approximately steady state after it reaches the surface and bottom boundaries of the fault (Figs. 4.2 and 4.3 (a)). The simulation domain is large enough to avoid boundary effects. We aim to demonstrate the influence of seismogenic depth (W) on rupture propagation and inelastic response near advancing rupture fronts. Therefore, we consider a single, vertical, and planar strike-slip fault embedded in a uniform material with P-wave velocity of 6 km/s, S-wave velocity of 3.464 km/s and density of 2670 kg/m^3.

The initial stress field is depth-dependent, and fluid pressure is hydrostatic and time-independent. The directions of principal stresses are shown in Fig. 4.1 (b) and (c), respectively, for the case with W = 15 km. To avoid a sudden arrest of rupture at depth and the normal stress increases up to the same value as the effective intermediate principal stress.

A linear slip-weakening friction law (Andrews, 1976b) is employed, in which the friction coefficient μ is a function of cumulative slip D:

$$\mu(D) = \mu_s - (\mu_s - \mu_d)\min(D/D_c, 1), \tag{4.1}$$

where μ_d is the dynamic friction coefficient, μ_s is the static friction coefficient, and D_c is the critical slip-weakening distance. Here, we assume μ_s = 0.6, μ_d = 0.1 (representative of thermally weakened faults) and D_c = 0.3 m (representative of seismological estimates for large earthquakes). The fault strength τ includes a cohesion C_o (different from off-fault plastic cohesion C, which will be discussed later):

$$\tau = C_o + \mu(\sigma_n - P_f), \tag{4.2}$$

where σ_n is normal stress on the fault, and P_f is fluid pressure. To avoid an excessively intense surface break of the rupture, C_o is set to 0.4 MPa at depths larger than 3 km, and linearly increases to 4 MPa from 3 km depth to the surface (Figs. 4.1(b) and 4.1(c)). The relative strength S parameter (Andrews, 1976b; Das and Aki, 1977), defined by

$$S = \frac{\tau_s - \tau_o}{\tau_o - \tau_d}, \tag{4.3}$$

where τ_o, $\tau_s = \mu_s\sigma_o$, $\tau_d = \mu_d\sigma_o$ and σ_o are initial shear stress, static strength, dynamic strength and initial normal stress, respectively, is set to 2 on most of the fault (Fig. 4.1(c)).

Rupture initiation is achieved by forcing the fault to rupture within a circular zone surrounding the hypocenter (Fig. 4.1(b)). We linearly reduce the friction coefficient from its static value at specified time T to its dynamic value within a time period t_o = 0.5 s. T is set to be infinity outside the nucleation zone, and inside the nucleation zone

$$T = \frac{r}{0.7V_s} + \frac{0.081r_{crit}}{0.7V_s}\left(\frac{1}{1-(\frac{r}{r_{crit}})^2} - 1\right), \tag{4.4}$$

where r is the distance from the hypocenter, r_{crit} is the radius of the nucleation zone (set to 3 km here) and V_s is shear wave velocity. This procedure forces the rupture to expand at a variable speed, about 0.7 V_s near the hypocenter and decreasing to zero at r_{crit}. Spontaneous rupture gradually overtakes the ever-slowing forced rupture.

The Drucker-Prager yield criterion (Drucker and Prager, 1952) is adopted in our study as the off-fault yielding criterion, by which the yield stress $Y(\boldsymbol{\sigma})$ depends on the mean normal stress:

$$Y(\boldsymbol{\sigma}) = -\left(\frac{\sigma_{kk}}{3} + P_f\right)\sin\varphi + C\cos\varphi, \tag{4.5}$$

where $\boldsymbol{\sigma}$ is the stress tensor, φ is the internal frictional angle and C is the plastic cohesion. The maximum shear stress is

$$\tau_{max} = \sqrt{\frac{1}{2}s_{ij}s_{ij}}, \tag{4.6}$$

where s is the deviatoric part of the stress tensor

$$s_{ij} = \sigma_{ij} - \frac{1}{3}\sigma_{kk}\delta_{ij}. \tag{4.7}$$

A Drucker-Prager yield function is defined as:

$$F(\boldsymbol{\sigma}) = \tau_{max} - Y(\boldsymbol{\sigma}), \tag{4.8}$$

with yielding starting when $F(\boldsymbol{\sigma}) = 0$. After yielding starts, the Duvaut-Lions-type viscoplasticity (Duan and Day, 2008) is used to calculate the accumulation of plastic strain ε^p through:

$$\dot{\varepsilon}_{ij} = \frac{1}{2\mu T_v}F(\boldsymbol{\sigma})\frac{s_{ij}}{\tau_{max}}, \tag{4.9}$$

where μ is shear modulus and T_v is the viscoplastic relaxation time scale. Viscosity is included here as an artificial means to mitigate mesh-dependency due to extreme

strain localization (Templeton and Rice, 2008). A scalar quantity is defined to describe the magnitude of plastic strain (Figs. 4.4 and 4.5) as:

$$\varepsilon_o^p = \sqrt{2\varepsilon_{ij}^p \varepsilon_{ij}^p}. \tag{4.10}$$

In this study $\varphi = arctan(0.6)$, C= 1.36 MPa and T_v = 0.03 s.

The 3D dynamic rupture problem coupled to wave propagation and plastic deformation is solved numerically with SPECFEM3D, a code based on the spectral element method (Kaneko et al., 2011; Galvez et al., 2014). The implementation of viscoplasticity in SPECFEM3D was verified by comparison to other numerical methods in a community benchmark problem (Harris et al., 2011).

4.3 Simulation results

Crack- to pulse-like rupture transition controlled by fault geometry

Seismic observations and dynamic rupture models indicate that rise time, the duration of earthquake slip at a given point on a fault, can be either comparable to or much shorter than the overall earthquake duration. The former case defines crack-like ruptures (Madariaga, 1976) while the latter case corresponds to pulse-like ruptures (Heaton, 1990). Proposed mechanisms of local slip arrest leading to pulse-like ruptures include self-healing due to velocity-dependent friction (e.g., Perrin et al., 1995; Beeler and Tullis, 1996) and stopping phases (healing fronts) generated by spatial changes of initial stress or strength on the fault (e.g., Beroza and Mikumo, 1996). A particular case of the latter mechanism, first described by Day (1982), is the generation of stopping phases at the deep limit of the seismogenic zone, which acts as a rupture barrier.

On mature strike-slip faults, the fault length is usually much larger than the fault width, as in the model setup described in Fig. 4.1 (a). Our first example of dynamic rupture simulation with off-fault plasticity is on a long fault with W = 15 km. We show resulting snapshots of slip rate in Fig. 4.2, and slip rate and slip profiles at 7.5 km depth in Figs. 4.3 (a) and (b), respectively. The rupture first grows as a self-similar crack-like rupture: the rupture front expands in all directions from the hypocenter, the peak slip rate increases with rupture propagation distance, and slip occurs simultaneously within the whole ruptured region. When the rupture front reaches the bottom boundary of the seismogenic zone, a stopping front is generated and propagates back into the ruptured area. When the healing front reaches the surface, the rupture splits into two pulses (i.e., a

pair of rupture fronts followed closely by healing fronts) that propagate in separate directions along the fault strike. The pulses eventually develop into a steady state, characterized by stable slip, rupture speed and peak slip velocity. Notably, the steady pulse width (i.e., the along-strike length of the region of active slip at a given time) is comparable to the seismogenic width W (Fig. 4.3 (a)).

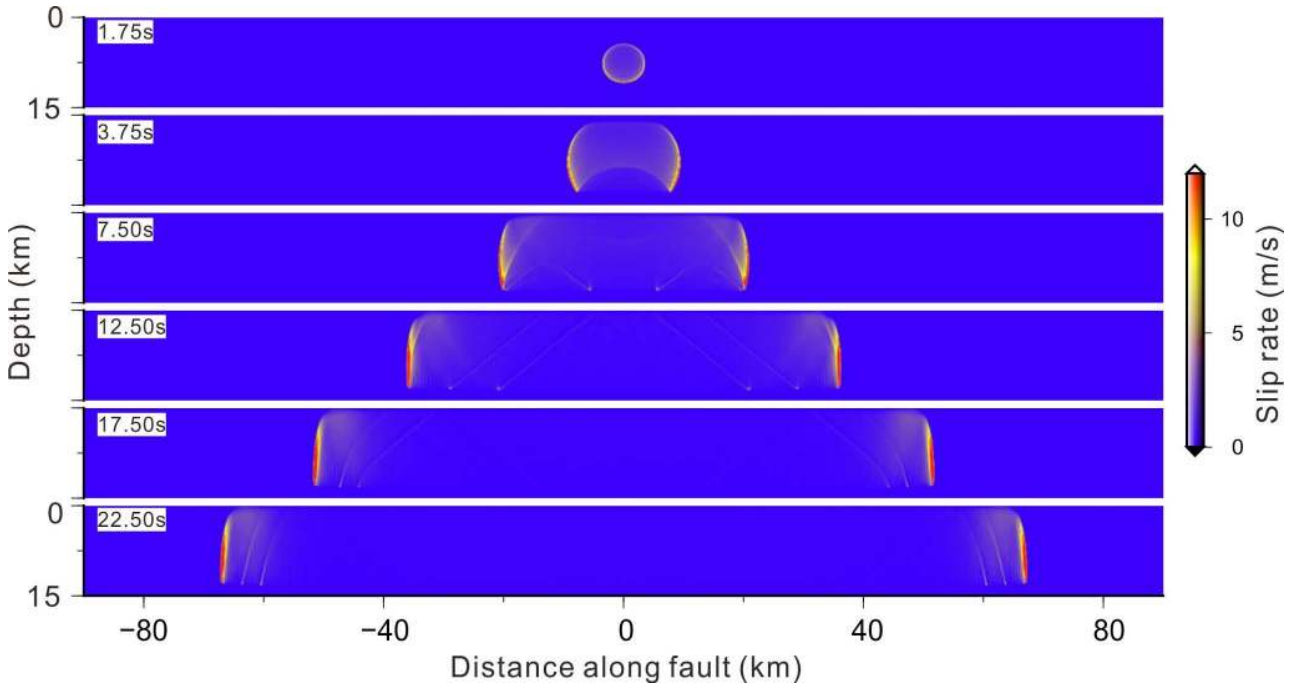

Figure 4.2: Development of a steady pulse-like rupture on a long fault. Distribution of horizontal slip rate at six different times (indicated by labels on the top left of each panel) in a dynamic rupture simulation with seismogenic depth W = 15 km.

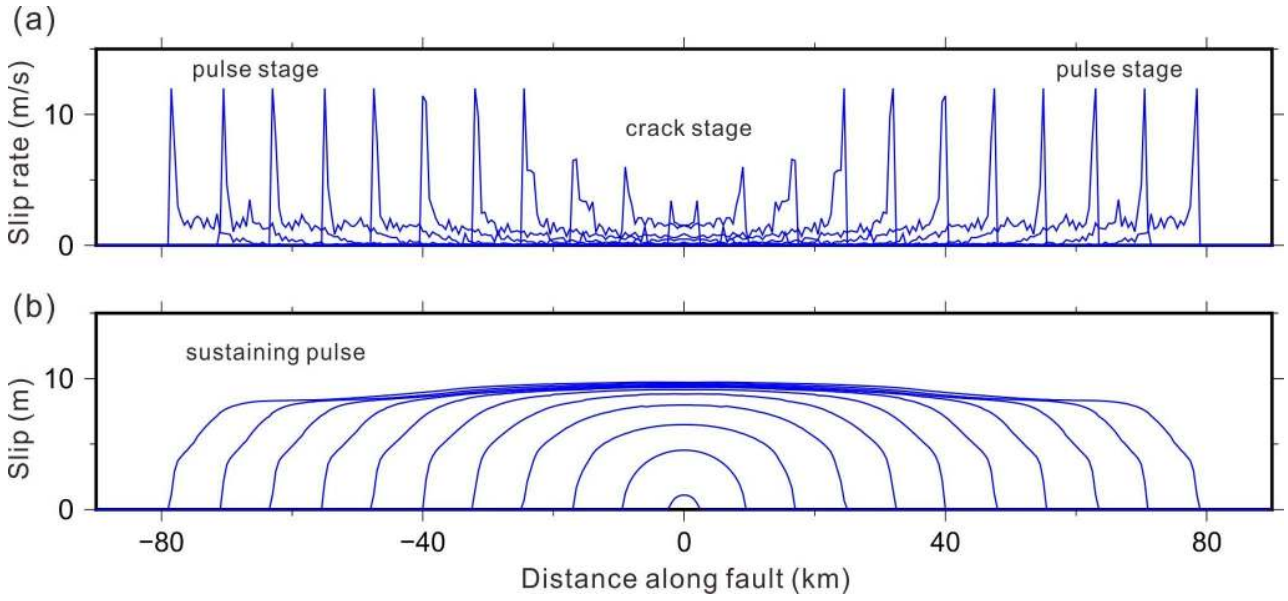

Figure 4.3: Slip rate (a) and slip (b) profiles every 2.5 s from 1.25 s to 26.25 s at 7.5 km depth for the rupture model with W = 15 km.

Plastic strain distribution

Figure 4.4 shows horizontal and vertical plastic strain distribution of our model with W = 15 km. Similar to Johri et al. (2014a), we observe that plastic strain decays as a function of distance from the fault core as a power-law at short distance, and drops more abruptly, exponentially at larger distance (Fig. 4.5). In this simulation and in those presented in the next section the change of plastic strain decay behavior occurs near $\varepsilon_p = 10^{-3.3}$. Thus, to facilitate the comparison between all our simulations, we define the thickness of the damage zone, H, as the distance at which $\varepsilon_p = 10^{-3.3}$. In the presence of dilatancy (volumetric and deviatoric plastic strains are proportional) and assuming the average fracture aperture is spatially uniform, fracture density is proportional to ε_p (Johri et al., 2014a). This relation connects rupture models with plasticity to field studies, in which the definition of damage zone thickness is based on fracture density. Field data on fracture density vs. distance has been interpreted either as power laws (Savage and Brodsky, 2011) or as exponential (Mitchell and Faulkner, 2009), but to our knowledge a transition between these two decay behaviors has not been reported. The field data shown in Figure 7-a of Savage and Brodsky (2011) is a rare example reminiscent of such transition. Nevertheless, based on the theoretical arguments developed in section 4.4, we expect the scaling properties discussed in this work to hold also for other definitions of H.

In Fig. 4.4(a), along the fault, the thickness of the damage zone first grows with increasing rupture distance, as found in 2D models (e.g., Gabriel et al., 2013; Xu et al., 2012b). However, H saturates at distance over $\sim$ 50 km, where the rupture becomes a stable pulse. This saturation was also noted in 3D simulations by Shi and Day (2013). In the deep region, damage is limited to the extensional quadrants. In Fig. 4.4(b), the vertical plastic strain pattern shows a "flower-like" structure with a narrow damage zone of nearly constant thickness in the deeper region and a wide damage zone of increasing thickness near the surface. Similar flower-like patterns of plastic strain were observed in previous 3D simulations (Ma and Andrews, 2010). In the shallower region, the inelastic strain is induced by seismic waves ahead of the rupture front, and is distributed in both extensional and compressional regions. The constant H in the deeper region in our model is explained in section 4.5 as a result of a linear depth-distribution of both initial stress and strength.

Damage zone thickness comparison for different seismogenic depths

We now examine the effect of the seismogenic depth W on the damage zone thickness H at mid-seismogenic depth. We conduct four additional simulations in which all settings are the same as in the previous one except the seismogenic depth, which is taken as W = 9, 12, 18 and 21 km, respectively. The width of the stress tapering zone near the fault bottom and the width of the zone of increased fault cohesion near the surface are set proportional to W.

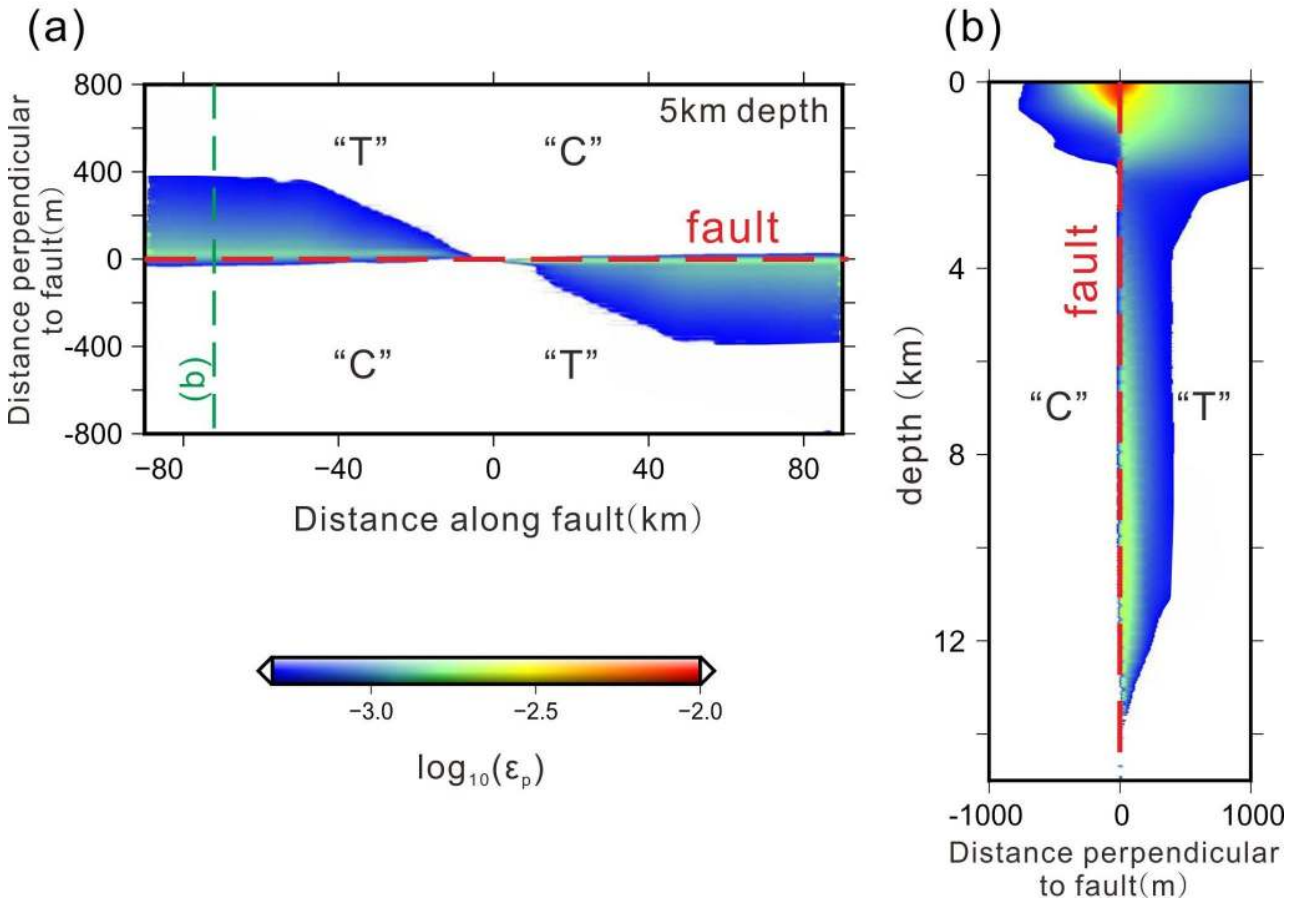

Figure 4.4: Distribution of plastic strain (ε_p) for the model with W = 15 km: (a) horizontal distribution at 5 km depth and (b) vertical distribution along the cross-section shown by a green dashed line in (a). The label C indicates a compressional region, and T a tensional region.

In Fig. 4.6 we compare the plastic strain distributions resulting from the three simulations with $W \leqslant 15$ km. The plastic strain patterns are similar for the three models. In particular, they all eventually reach a steady damage zone geometry at sufficient distance from the hypocenter. However, the off-fault extent of their plastic zones is different, it increases as a function of W. Fig. 4.5 compares fault-normal profiles of plastic strain at 5 km depth and at a horizontal distance of 70 km form the hypocenter, a distance at which the damage zone has already reached a steady thickness, H_{max}, in all five simulations. In this figure, distance is normalized by W and the inset shows how our measure of damage zone thickness H (the distance from the fault at which plastic strain is $\varepsilon_p = 10^{-3.3}$) depends on W. The steady damage zone thickness in our five models vary from ~ 100 to ~ 500 meters, a range of values that agrees well with the largest values obtained from field observations (Savage and Brodsky, 2011). The approximate collapse in Fig. 4.5 of the normalized plastic strain profiles corresponding to the four models with $W \geqslant 12$ km indicates that H_{max} is approximately proportional to W if W is large enough. The dashed gray line in the inset of Fig. 4.5 is a hypothesized asymptotic linear H_{max}-W scaling. The model with the smallest W (9 km) has an H_{max} significantly over-predicted by the linear H_{max}-W scaling (Fig. 4.5 inset). These key results of our simulations are put on a theoretical basis in the next section.

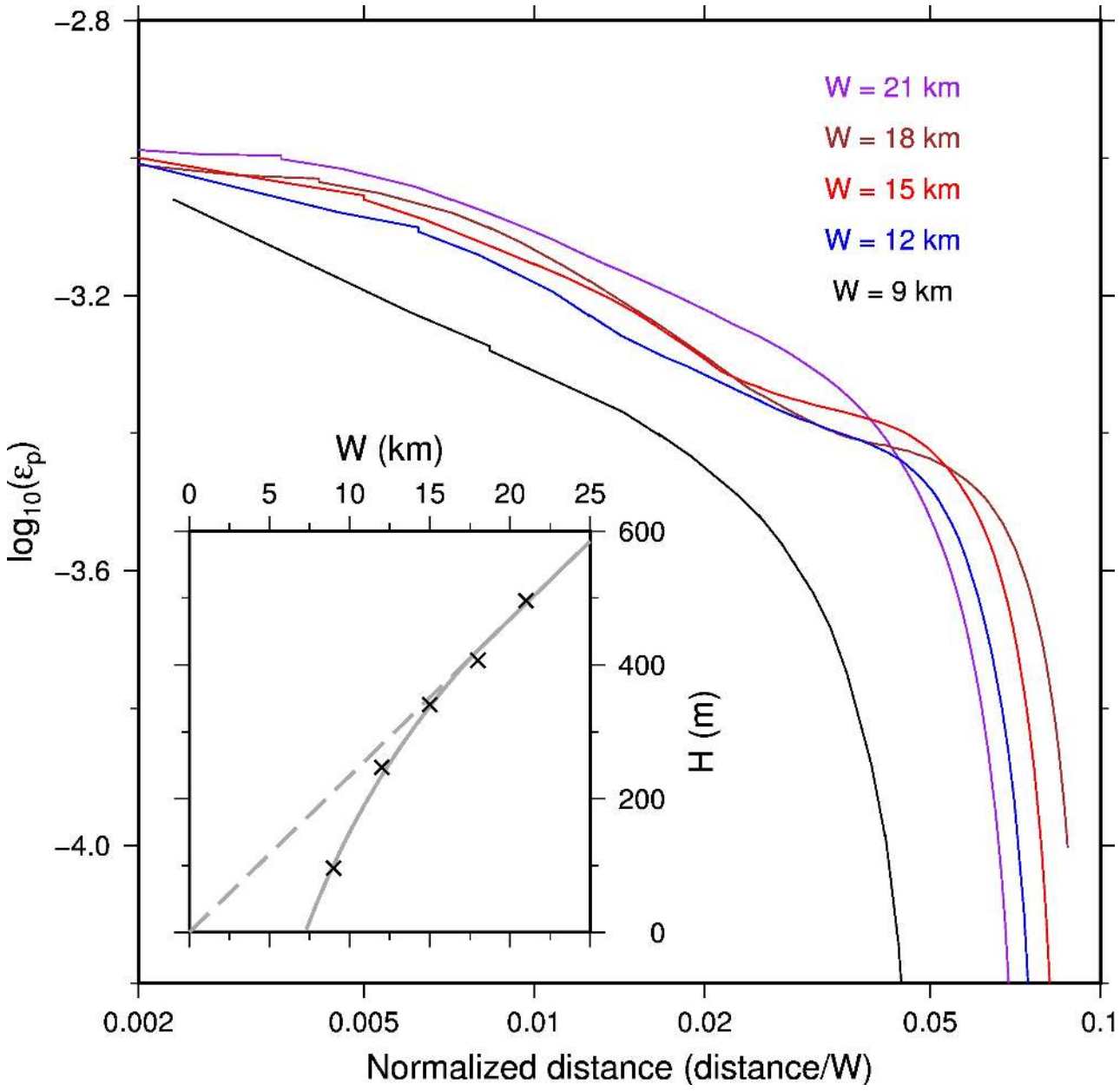

Figure 4.5: Plastic strain (ε_p) as a function of distance from the fault plane for models with different seismogenic depths (W) ranging form 9 to 21 km. Profiles are located at 5 km depth and 70 km horizontal distance from the hypocenter. The insert shows with crosses the damage zone thickness (H), defined here as the distance at which $\varepsilon_p = 10^{-3.3}$, as a function of W for all simulations. The solid gray curve is our interpretation of the non-linear trend in the simulation data. The dashed gray line is an asymptotic linear relation between H and W at large W motivated by our theoretical analysis.

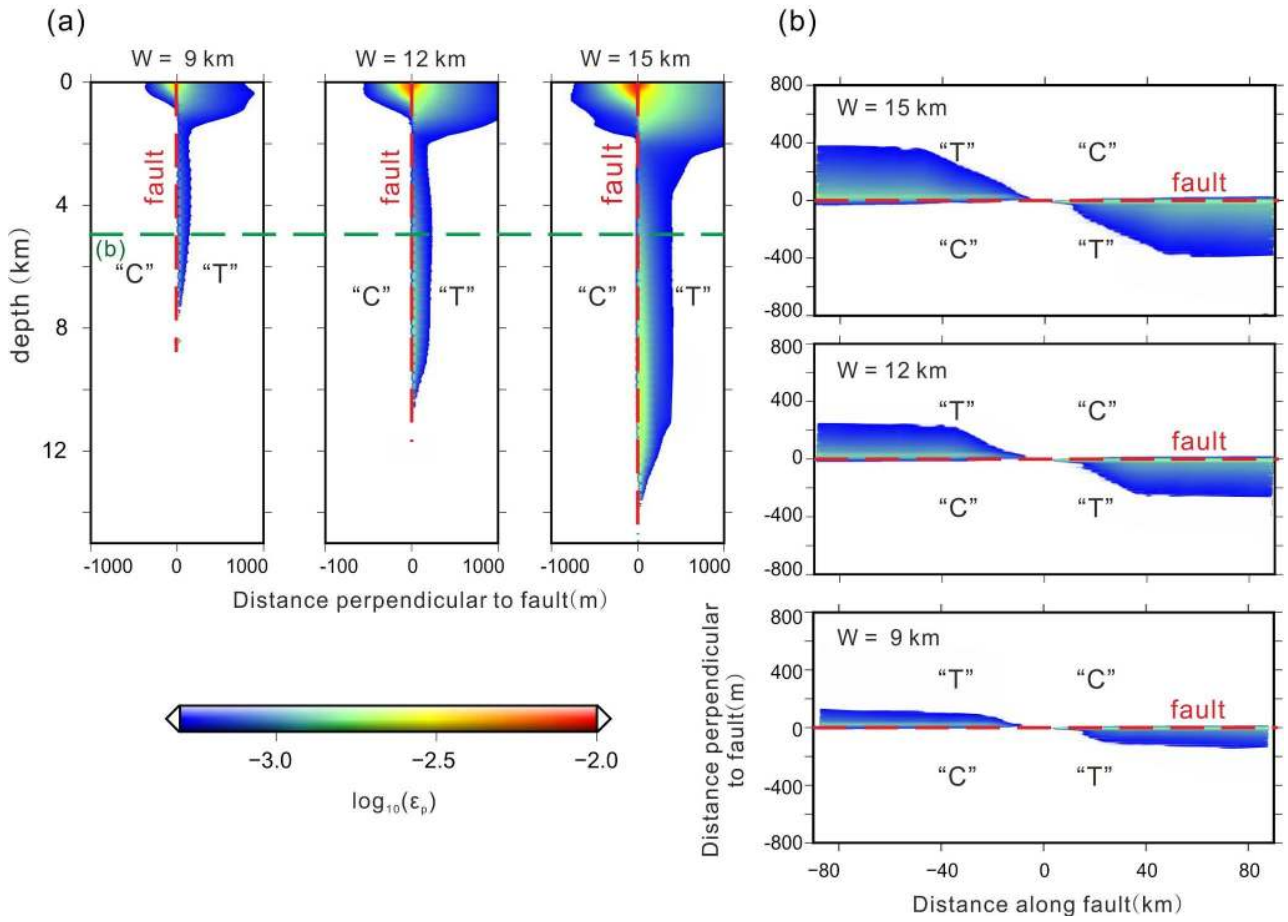

Figure 4.6: Comparison of the plastic strain distribution among different models with W = 9, 12, and 15 km, respectively, (a) along a vertical cross-section at 70 km horizontal distance from the hypocenter and (b) on a horizontal cross-section at 5 km depth.

4.4 Theoretical estimate of damage zone thickness

On the basis of fracture mechanics arguments, Ben-Zion and Ampuero (2009) and Xu et al. (2012b) developed theoretical relations between the thickness of dynamically generated damage zones, initial stresses, material strength and rupture speed. Xu et al. (2012b) found that this approach predicts well the yielding zone thickness obtained in 2D dynamic crack-like rupture simulations with off-fault plasticity. A fracture mechanics analysis of damage zones formed by quasi-static fault growth was developed by Scholz et al. (1993). These models predict a self-similar scaling in which H is proportional to fault or rupture length L, without saturation. Here, we apply the dynamic fracture mechanics approach to pulse-like ruptures in 3D, which allows us to assess the effect of seismogenic width.

An estimate of the thickness of the damage zone generated by a dynamic rupture is the distance at which the stress concentration near the rupture tip exceeds the yield strength of the material (e.g. equation 14a of Ben-Zion and Ampuero (2009)):

$$H \approx (\frac{K}{\tau_s - \tau_o})^2, \tag{4.11}$$

where K is the dynamic stress intensity factor. The yield strength τ_s involved in this equation pertains to the off-fault material, and can be higher than the yield strength of the fault. This estimate assumes that the on-fault slip-weakening zone near the rupture front is much smaller than the rupture dimensions, which is the case in our simulations, and significantly smaller than H, which is better satisfied at large W as discussed at the end of this section. The squared stress intensity factor K^2 scales with a characteristic length of the rupture. For small earthquakes, represented as circular ruptures, the characteristic length is the rupture radius and Equation 4.11 predicts self-similar scaling between H and rupture length L. For larger earthquakes with elongated rupture area, $L \gg W$, the characteristic length that controls K is the shortest one (Eshelby, 1957), and thus H scales with rupture width W. For pulse-like ruptures, the characteristic length is the along-strike width of the pulse. As illustrated in section 4.3.1, large earthquake ruptures that saturate the seismogenic depth are inevitably pulse-like, and their pulse width scales with seismogenic depth W. This break in self-similarity leads to a linear relation between H and W, as found in our simulations with large W (inset of Fig. 4.5).

In more detail, following Xu et al. (2012b) but considering pulse-like ruptures and ignoring some factors of order one,

$$H \approx (k(v_r)\frac{\tau_o - \tau_d}{\tau_s - \tau_d})^2 W, \tag{4.12}$$

where k is a decreasing dimensionless function of rupture speed, v_r. In particular, k and K are larger at the stopping ends of a rupture, especially if arrest occurs in a fault region with large fracture energy rather than low initial stress. Moreover, pulse width can be smaller than in our simulations if the pulse-like behavior is controlled by self-healing due to dynamic weakening mechanisms (Heaton, 1990) instead of a geometric effect of the finite seismogenic depth. Thus an upper bound on coseismic damage zone thickness is

$$H_{max} \approx (\frac{\tau_o - \tau_d}{\tau_s - \tau_d})^2 W. \tag{4.13}$$

This linear H_{max}-W relation is consistent with our simulation results at large W (Fig. 4.5 inset, dashed gray line). Equations 4.12 and 4.13 should be understood as containing a multiplicative factor of order 1 that accommodates different definitions of H and encapsulates geometric effects ignored in our derivation.

The departure from a linear H_{max}-W scaling at low W in our simulations (Fig. 4.5 inset) is attributed here to a blunting effect of the on-fault slip weakening zone. The derivation of Equation 4.13 assumes that H_{max} is significantly larger than the slip-weakening zone size l_c. Using equation 24 of Gabriel et al. (2013), we find that the ratio H_{max}/l_c is proportional to a function of rupture speed and, more importantly, to the non-dimensional number κ introduced by Madariaga and Olsen (2000) to represent the ratio between available elastic energy and fracture energy:

$$\kappa = \frac{W(\tau_o - \sigma_o \mu_d)^2}{G\sigma_o(\mu_s - \mu_d)D_c}, \tag{4.14}$$

where G is shear modulus. Because the initial stresses τ_o and σ_o increase linearly with depth in our models, κ is proportional to W^2 and decreasing W rapidly decreases κ. We thus consider that the model with $W = 9$ km has approached an unusual regime associated with low values of H_{max}/l_c in which the smoothening effect of the slip-weakening zone reduces significantly the off-fault stresses and hence the damage zoen thickness. This is simply an artifact of the large value of critical slip-weakening distance (D_c) and low value of initial stress ratio τ_o/σ_o adopted here to limit the computational cost of the simulations. We expect that simulations with smaller κ should give a nearly linear H_{max}-W relation down to smaller values of W. Moreover, regardless of the value of κ, Equation 4.13 provides a useful upper bound on H_{max}.

4.5 Discussion and conclusions

Our 3D dynamic rupture simulations and fracture mechanics arguments indicate that damage zone thickness is ultimately bounded in long faults by the limiting effect of

seismogenic depth on the efficiency of stress concentration near a rupture front. In particular, Equation 4.13 provides a quantitative prediction of the relation between limiting damage zone thickness, state of stress, dynamic fault strength, off-fault yield strength and seismogenic depth, which we can compare to field observations.

Average stress drops ($\tau_o - \tau_d$) of large earthquakes are typically on the order of a few MPa, and order of magnitude smaller than estimates of strength drop ($\tau_s - \tau_d = \sigma_o(\mu_s - \mu_d)$) based on typical values of effective confining stress σ_o at seismogenic depth and of static and dynamic friction coefficients. Thus, the predicted H_{max} is about two orders of magnitude smaller than W, that is , a few 100 m. This order-of-magnitude estimate is consitent with field observations of damage zone thickness on large-displacement faults (Savage and Brodsky, 2011; Mitchell and Faulkner, 2009, 2012).

The saturation of H as a function of fault displacement (long-term cumulative slip) in the data complied by Savage and Brodsky (2011) occurs at displacements of a few km or less. Considering that displacement to fault length ratios typically range from 0.1 to 0.01 on faults with displacement shorter than a few km (Kim and Sanderson, 2005), the saturation of H starts at fault lengths ranging from a few 10 km to a few 100 km. This range encompasses the typical values of seismogenic depth, which is consistent with our model. In particular, in the data of strike-slip faults compiled by Kim and Sanderson (2005), a displacement of a few km corresponds to a length of a few 10 km, which quantitatively supports our interpretation of the role of seismogenic depth in limiting damage zone thickness.

The constant thickness of deep damage zones found in our simulations can be rationalized from a theoretical basis. Our model assumed linearly increasing initial shear stress and material strength, such that the ratio $(\tau_o - \tau_d)/(\tau_s - \tau_d)$ is independent of depth. Equation 4.13 predicts a constant H in this situation. This estimate is not appropriate near the surface, where dynamic free surface effects and cohesion play important roles. Damage zone properties at seismogenic depth are difficult to resolve by seismological techniques. Current field data compilations (e.g., Savage and Brodsky, 2011) include observations on exhumed faults that capture fault zone structures from a range of depths, including shallow and deep ones, which may contribute to the data scatter. In this study, we have focused on a scaling feature (saturation of H) that is apparent in the field data despite its significant scatter.

Our theoretical argument further suggests that the ratio H_{max}/W is a relative measure of the stress τ_o at which an active fault operates in the long term. In particular,

Equation 4.13 predicts that a critically stressed fault, in which the average shear stress is close to yield ($\tau_o \approx \tau_s$), would have a thicker damage zone than a fault operating at sub-critical stress. According to this model, the small value of H_{max}/W in natural faults is additional evidence that long mature faults operate at stresses significantly lower than the crustal yield strength.

The simulations presented here are intentionally based on simplifying assumptions regarding fault friction, fault geometry, state of stress and material heterogeneities. An important next step in the development of earthquake models is to study the evolution of fault zone damage through multiple earthquake cycles on long faults, including not only the accumulations of plastic strain but also the reduction in elastic moduli around the fault (Kaneko et al., 2011; Xu et al., 2015). If the evolution of a fault towards increasing maturity is accompanied by a tendency to operate at lower stress (Fang and Dunham, 2013), our theoretical results suggest the hypothesis that further damage may localize on thinner zones, which could be tested in simulations of long-term damage evolution. Such a simulation framework could also provide insight on how fault growth leaves systematic changes of damage zone properties along strike that may control the distribution of earthquake slip and rupture speed (Cappa et al., 2014; Perrin et al., 2016a).

An additional argument allows us to conclude that short-term damage processes are essential in the evolution of fault zone structure. While the present work emphasizes damage occurring over co-seismic time scales, a similar saturation of damage zone thickness is predicted for slower, quasi-static damage processes, because the static stress intensity factor K is also limited by the depth extent of fault slip (seismic or aseismic). However, if damage were dominated by time scales longer than deep afterslip and longer than the relaxation time of the asthenosphere, the relevant model would be a throughgoing crack in a thin elastic slab (the lithosphere, decoupled from the asthenosphere). The long-term K would no longer be limited by W, as shown by Lehner et al. (1981), and the damage zone thickness would not saturate.

These different predictions of scaling behavior also help us identify aspects of fault zone evolution that may be controlled by long-term damage processes. At a larger scale than the damage zones considered here, faults develop an "outer damage zone" (Perrin et al., 2016b) that encompasses a network of secondary faults. The younger fault branches often organize near the tips of the main fault into splay fault fans, whose width scales with fault length without saturation (Perrin et al., 2016a). This observation is consistent with a model in which the evolution of outer damage zones

is controlled by fault growth and branching processes operating over time scales longer than the viscous relaxation time of the asthenosphere.

Acknowledgments

This work was supported by the Southern California Earthquake Center (funded by NSF Cooperative Agreement EAR-1033462 and USGS Cooperative Agreement G12AC20038) and by the National Science Foundation (CAREER award EAR-1151926).

References

Andrews, DJ (1976a). Rupture propagation with finite stress in antiplane strain. *Journal of Geophysical Research*, 81(20):3575–3582. doi: 10.1029/jb081i020p03575.

Andrews, DJ (1976b). Rupture velocity of plane strain shear cracks. *Journal of Geophysical Research*, 81(32):5679–5687. doi: 10.1029/jb081i032p05679.

Andrews, DJ (2005). Rupture dynamics with energy loss outside the slip zone. *Journal of Geophysical Research: Solid Earth*, 110(B1). doi: 10.1029/2004jb003191.

Beeler, NM and TE Tullis (1996). Self-healing slip pulses in dynamic rupture models due to velocity-dependent strength. *Bulletin of the Seismological Society of America*, 86(4):1130–1148.

Ben-Zion, Yehuda and Jean-Paul Ampuero (2009). Seismic radiation from regions sustaining material damage. *Geophysical Journal International*, 178(3):1351–1356. doi: 10.1111/j.1365-246x.2009.04285.x.

Ben-Zion, Yehuda and Zheqiang Shi (2005). Dynamic rupture on a material interface with spontaneous generation of plastic strain in the bulk. *Earth and Planetary Science Letters*, 236(1-2):486–496. doi: 10.1016/j.epsl.2005.03.025.

Beroza, Gregory C and Takeshi Mikumo (1996). Short slip duration in dynamic rupture in the presence of heterogeneous fault properties. *Journal of Geophysical Research: Solid Earth*, 101(B10):22449–22460. doi: 10.1029/96jb02291.

Cappa, Frédéric, Clément Perrin, Isabelle Manighetti, and Elodie Delor (2014). Off-fault long-term damage: A condition to account for generic, triangular earthquake slip profiles. *Geochemistry, Geophysics, Geosystems*, 15(4):1476–1493. doi: 10.1002/2013gc005182.

Das, Shamita and Keiiti Aki (1977). A numerical study of two-dimensional spontaneous rupture propagation. *Geophysical journal international*, 50(3):643–668. doi: 10.1111/j.1365-246x.1977.tb01339.x.

Day, Steven M (1982). Three-dimensional finite difference simulation of fault dynamics: rectangular faults with fixed rupture velocity. *Bulletin of the Seismological Society of America*, 72(3):705–727.

Drucker, Daniel Charles and William Prager (1952). Soil mechanics and plastic analysis or limit design. *Quarterly of applied mathematics*, 10(2):157–165. doi: 10.1090/qam/48291.

Duan, Benchun and Steven M Day (2008). Inelastic strain distribution and seismic radiation from rupture of a fault kink. *Journal of Geophysical Research: Solid Earth*, 113(B12). doi: 10.1029/2008jb005847.

Eshelby, John D (1957). The determination of the elastic field of an ellipsoidal inclusion, and related problems. *Proc. R. Soc. Lond. A*, 241(1226):376–396. doi: 10.1098/rspa.1957.0133.

Fang, Zijun and Eric M Dunham (2013). Additional shear resistance from fault roughness and stress levels on geometrically complex faults. *Journal of Geophysical Research: Solid Earth*, 118(7):3642–3654. doi: 10.1002/jgrb.50262.

Faulkner, DR, TM Mitchell, David Healy, and MJ Heap (2006). Slip on 'weak' faults by the rotation of regional stress in the fracture damage zone. *Nature*, 444 (7121):922. doi: 10.1038/nature05353.

Gabriel, A-A, J-P Ampuero, LA Dalguer, and Paul Martin Mai (2013). Source properties of dynamic rupture pulses with off-fault plasticity. *Journal of Geophysical Research: Solid Earth*, 118(8):4117–4126. doi: 10.1002/jgrb.50213.

Galvez, Percy, J-P Ampuero, Luis A Dalguer, Surendra N Somala, and Tarje Nissen-Meyer (2014). Dynamic earthquake rupture modelled with an unstructured 3-d spectral element method applied to the 2011 m 9 tohoku earthquake. *Geophysical Journal International*, 198(2):1222–1240. doi: 10.1093/gji/ggu203.

Harris, Ruth A, Michael Barall, DJ Andrews, Benchun Duan, Shuo Ma, EM Dunham, A-A Gabriel, Y Kaneko, Y Kase, BT Aagaard, et al. (2011). Verifying a computational method for predicting extreme ground motion. *Seismological Research Letters*, 82(5):638–644. doi: 10.1785/gssrl.82.5.638.

Heaton, Thomas H (1990). Evidence for and implications of self-healing pulses of slip in earthquake rupture. *Physics of the Earth and Planetary Interiors*, 64(1): 1–20. doi: 10.1016/0031-9201(90)90002-f.

Huang, Yihe and Jean-Paul Ampuero (2011). Pulse-like ruptures induced by low-velocity fault zones. *Journal of Geophysical Research: Solid Earth*, 116(B12). doi: 10.1029/2011jb008684.

Huang, Yihe, Jean-Paul Ampuero, and Don V Helmberger (2014). Earthquake ruptures modulated by waves in damaged fault zones. *Journal of Geophysical Research: Solid Earth*, 119(4):3133–3154. doi: 10.1002/2013jb010724.

Huang, Yihe, Jean-Paul Ampuero, and Don V Helmberger (2016). The potential for supershear earthquakes in damaged fault zones–theory and observations. *Earth and Planetary Science Letters*, 433:109–115. doi: 10.1016/j.epsl.2015.10.046.

Johri, Madhur, Eric M Dunham, Mark D Zoback, and Zijun Fang (2014a). Predicting fault damage zones by modeling dynamic rupture propagation and comparison with field observations. *Journal of Geophysical Research: Solid Earth*, 119(2): 1251–1272. doi: 10.1002/2013jb010335.

Johri, Madhur, Mark D Zoback, and Peter Hennings (2014b). A scaling law to characterize fault-damage zones at reservoir depthsfault damage zones at depth. *AAPG Bulletin*, 98(10):2057–2079. doi: 0.1306/05061413173.

Kaneko, Y, J-P Ampuero, and N Lapusta (2011). Spectral-element simulations of long-term fault slip: Effect of low-rigidity layers on earthquake-cycle dynamics. *Journal of Geophysical Research: Solid Earth*, 116(B10). doi: 10.1029/2011jb008395.

Kim, Young-Seog and David J Sanderson (2005). The relationship between displacement and length of faults: a review. *Earth-Science Reviews*, 68(3-4):317–334. doi: 10.1016/j.earscirev.2004.06.003.

Lehner, Florian K, Victor C Li, and JR Rice (1981). Stress diffusion along rupturing plate boundaries. *Journal of Geophysical Research: Solid Earth*, 86(B7):6155–6169. doi: 10.1029/jb086ib07p06155.

Ma, Shuo and DJ Andrews (2010). Inelastic off-fault response and three-dimensional dynamics of earthquake rupture on a strike-slip fault. *Journal of Geophysical Research: Solid Earth*, 115(B4). doi: 10.1029/2009jb006382.

Madariaga, Raul (1976). Dynamics of an expanding circular fault. *Bulletin of the Seismological Society of America*, 66(3):639–666.

Madariaga, Raul and Kim B Olsen (2000). Criticality of rupture dynamics in 3-d. *Pure and Applied Geophysics*, 157(11-12):1981–2001. doi: 10.1007/pl00001071.

Milliner, Christopher WD, James F Dolan, James Hollingsworth, Sebastien Leprince, Francois Ayoub, and Charles G Sammis (2015). Quantifying near-field and off-fault deformation patterns of the 1992 mw 7.3 landers earthquake. *Geochemistry, Geophysics, Geosystems*, 16(5):1577–1598. doi: 10.1002/2014gc005693.

Mitchell, TM and DR Faulkner (2009). The nature and origin of off-fault damage surrounding strike-slip fault zones with a wide range of displacements: A field study from the atacama fault system, northern chile. *Journal of Structural Geology*, 31(8):802–816. doi: 10.1016/j.jsg.2009.05.002.

Mitchell, TM and DR Faulkner (2012). Towards quantifying the matrix permeability of fault damage zones in low porosity rocks. *Earth and Planetary Science Letters*, 339:24–31. doi: 0.1016/j.epsl.2012.05.014.

Pelties, Christian, Yihe Huang, and Jean-Paul Ampuero (2015). Pulse-like rupture induced by three-dimensional fault zone flower structures. *Pure and Applied Geophysics*, 172(5):1229–1241. doi: 10.1007/s00024-014-0881-0.

Perrin, Clément, Isabelle Manighetti, Jean-Paul Ampuero, Frédéric Cappa, and Yves Gaudemer (2016a). Location of largest earthquake slip and fast rupture controlled by along-strike change in fault structural maturity due to fault growth. *Journal of Geophysical Research: Solid Earth*, 121(5):3666–3685. doi: 10.1002/2015jb012671.

Perrin, Clément, Isabelle Manighetti, and Yves Gaudemer (2016b). Off-fault tip splay networks: A genetic and generic property of faults indicative of their long-term propagation. *Comptes Rendus Geoscience*, 348(1):52–60. doi: 10.1016/j.crte.2015.05.002.

Perrin, Gilles, James R Rice, and Gutuan Zheng (1995). Self-healing slip pulse on a frictional surface. *Journal of the Mechanics and Physics of Solids*, 43(9):1461–1495. doi: 10.1016/0022-5096(95)00036-i.

Poliakov, Alexei NB, Renata Dmowska, and James R Rice (2002). Dynamic shear rupture interactions with fault bends and off-axis secondary faulting. *Journal of Geophysical Research: Solid Earth*, 107(B11). doi: 10.1029/2001jb000572.

Rice, James R, Charles G Sammis, and Robert Parsons (2005). Off-fault secondary failure induced by a dynamic slip pulse. *Bulletin of the Seismological Society of America*, 95(1):109–134. doi: 10.1785/0120030166.

Savage, Heather M and Emily E Brodsky (2011). Collateral damage: Evolution with displacement of fracture distribution and secondary fault strands in fault damage zones. *Journal of Geophysical Research: Solid Earth*, 116(B3). doi: 10.1029/2010jb007665.

Scholz, CH, NH Dawers, J-Z Yu, MH Anders, and PA Cowie (1993). Fault growth and fault scaling laws: preliminary results. *Journal of Geophysical Research: Solid Earth*, 98(B12):21951–21961. doi: 10.1016/0148-9062(94)90484-7.

Shi, Zheqiang and Steven M Day (2013). Rupture dynamics and ground motion from 3-d rough-fault simulations. *Journal of Geophysical Research: Solid Earth*, 118(3):1122–1141. doi: 10.1002/jgrb.50094.

Spudich, P and KB Olsen (2001). Fault zone amplified waves as a possible seismic hazard along the calaveras fault in central california. *Geophysical Research Letters*, 28(13):2533–2536. doi: 10.1029/2000gl011902.

Templeton, Elizabeth L and James R Rice (2008). Off-fault plasticity and earthquake rupture dynamics: 1. dry materials or neglect of fluid pressure changes. *Journal of Geophysical Research: Solid Earth*, 113(B9). doi: 10.1029/2007jb005529.

Xu, Shiqing, Yehuda Ben-Zion, and Jean-Paul Ampuero (2012a). Properties of inelastic yielding zones generated by in-plane dynamic ruptures—i. model description and basic results. *Geophysical Journal International*, 191(3):1325–1342. doi: 10.1111/j.1365-246x.2012.05679.x.

Xu, Shiqing, Yehuda Ben-Zion, and Jean-Paul Ampuero (2012b). Properties of inelastic yielding zones generated by in-plane dynamic ruptures—ii. detailed parameter-space study. *Geophysical Journal International*, 191(3):1343–1360. doi: 10.1111/j.1365-246x.2012.05685.x.

Xu, Shiqing, Yehuda Ben-Zion, Jean-Paul Ampuero, and Vladimir Lyakhovsky (2015). Dynamic ruptures on a frictional interface with off-fault brittle damage: feedback mechanisms and effects on slip and near-fault motion. *Pure and Applied Geophysics*, 172(5):1243–1267. doi: 10.1007/s00024-014-0923-7.

Chapter 5

MECHANICAL STRENGTH AND ANISOTROPY OF CONTINENTAL LITHOSPHERE AT THE ZAGROS-HIMALAYA BELT AND SURROUNDING REGIONS

Variation of lithospheric strength controls the distribution of stress and strain within plates and at plate boundaries. Simultaneously, deformation caused by localized stress and strain reduces the lithospheric strength. We calculate the effective elastic thickness, T_e, which is a proxy of lithospheric strength, and its anisotropy at the Zagros-Himalaya belt and surrounding regions. T_e varies from < 5 km to over 100 km, and shows good correlations with geological and geophysical data. Along plate boundaries, mountain belts and major faults, T_e is usually smaller than 30 km. In basins, T_e is between 30 - 60 km. In stable cratons, T_e is larger than 60 km. In the regions with low and intermediate strength (T_e < 60 km), the extent of T_e anisotropy is usually large, and the weak direction of T_e anisotropy agrees well with the directions of GPS data and crustal stress. In stable cratons, the extent of T_e anisotropy is usually small. Our results suggest that mechanical weakening is the dominate mechanism in reducing the lithospheric strength in regions where T_e is smaller than 60 km. In stable cratons, the effects of mechanical weakening can be ignored, and only thermal weakening resulted from mantle processes can modify the lithospheric strength substantially.

5.1 Introduction

The classic plate tectonic theory assumes that plate boundary accommodates most plate deformation, generating large earthquakes in a relatively narrow zone, while the plate interior is rigid with little deformation. However, in the continents, large plates are divided into blocks and are connected with suture zones. Deformations often extend into the interior of a plate as suggested by large earthquakes within the plate (e.g., Zhang et al., 2003). At continental collision regions, deformation can occur over a wide zone, sometimes even wider than 1000 km (Kreemer et al., 2003). These observations contradict the classic plate tectonic theory, and in order to explain these phenomena, study of the strength variation of continental plates and plate boundaries is needed. In addition to the important tectonic meaning, understanding the strength variation in the continents and its interaction with lithospheric

deformation contributes to a better estimation of seismic hazards.

Analyzing the flexural behavior of the lithosphere is a common way to estimate the vertically integrated strength of the lithosphere. In the flexural bending model, a uniform elastic plate with thickness T_e lies over a viscous fluid and bends under the applied surface or subsurface loads. The bending related predictions are compared with observations to determine the proper value of T_e (Watts, 2001). T_e is called the effective elastic thickness of the lithosphere and is related to the rigidity (D) of the lithosphere through

$$D = \frac{ET_e^3}{12(1-\upsilon)}, \tag{5.1}$$

where E is the Young's modulus and υ is the Poisson's ratio of the lithosphere. T_e estimations are divided into forward model methods and spectral methods based on whether comparing the direct model predictions with observations or studying the correlations between model predictions in spectral domain. Both kinds of methods are widely used to study the continental lithospheric strength (e.g., Pirouz et al., 2017; Chen et al., 2017), while only spectral methods have been advanced to compute mechanical anisotropy.

One limitation of the flexural bending model is related to the assumption of uniform elastic plate thickness in the derivation of the governing differential equation for the flexure (w) of the plate. To illustrate this, we consider a plate extending in the x direction and bending under the applied load $q(x)$. The second order differential equation for the moment (M) is expressed as

$$\frac{d^2M}{dx^2} = -q(x) + P\frac{d^2w}{dx^2}, \tag{5.2}$$

where P is the horizontal pressure within the plate. M is related to both the rigidity (D) of the plate and the second derivative of the flexure ($\frac{d^2w}{dx^2}$). The Young's modulus and the Poisson's ratio are generally set to be constant during the calculation. With the further assumption of constant thickness for the plate, we arrive at the forth order differential equation for the flexure (w)

$$D\frac{d^4w}{dx^4} = q(x) - P\frac{d^2w}{dx^2}. \tag{5.3}$$

Eq. (5.3) is the basis for plate bending analysis and T_e calculations. However, if the plate thickness is not constant and

$$\frac{d^2D}{dx^2} \neq 0, \tag{5.4}$$

then Eq. (5.3) need to be modified, which shows that using Eq. (5.3) to calculate T_e variation may be problematic. Nevertheless, numerous previous studies mapped T_e variations with methods incorporating Eq. (5.3) (e.g., Lowry and Smith, 1994; Lowry and Pérez-Gussinyé, 2011; Audet and Bürgmann, 2011).

The relationship between T_e and lithospheric deformation in the continent has been investigated previously. In western U.S., Lowry and Smith (1994, 1995) showed that Cenozoic normal faults are found primarily in areas of low T_e, with an approximate correlation between seismicity and T_e gradient. Later, Lowry and Pérez-Gussinyé (2011) suggested that the low T_e region plays an important role in localizing deformation. Audet et al. (2007) and Audet and Bürgmann (2011) also concluded that strain is prone to concentrate at weak region where T_e is small based on comparisons between T_e and other physical properties in western Canada and global continental regions. These studies used low spatial resolution spectral methods which may influence the detailed explanations between T_e and lithospheric deformation. Kirby and Swain (2011) improved the spatial resolution in T_e estimation with the high resolution 'fan' wavelet method. With the improved method, Mao et al. (2012) showed that earthquakes occur more frequently in regions where T_e is smaller than 30 km, and within the Cathaysia block, in the eastern part of South China, there exists a large low T_e and low seismicity region. Chen et al. (2015a) showed that T_e variations at the Arabian plate are correlated with the structural differences in the lithosphere between the Arabian shield in the west and the Arabian platform in the east. Although these studies improved our understanding of T_e, the relationship between T_e and other geological and geophysical data is still not clear, and how the lithospheric strength controls and is affected by the lithospheric deformation remains poorly understood.

The azimuthal variations in the strength is described with the T_e anisotropy model which is composed with a long axis with the largest T_e value and a short axis with the smallest T_e value at perpendicular directions and the azimuth of the short T_e axis (Kirby and Swain, 2006). The tectonic and geophysical meanings of T_e anisotropy are more obscure compared to T_e, and its direction does not show a unique relationship with other geophysical observations in previous work. Kirby and Swain (2006) found that the weak direction of T_e anisotropy is nearly perpendicular to shear-wave splitting direction in Australia, while Audet et al. (2007) obtained parallel relationships between the weak direction of T_e anisotropy and both shear-wave splitting direction and maximum horizontal compressive stress direction in western

Canada. Later, Audet and Bürgmann (2011) suggested that no preferred angular relationships exist between the weak diretion of T_e anisotropy and dynamic indicators in the crust and mantle. Different hypotheses are proposed for the formation of T_e anisotropy, including localized brittle failure of crustal rocks under deviatoric stress (Lowry and Smith, 1995), 'frozen' deformation by alignment of olivine in the lithospheric mantle (Kirby and Swain, 2006; Simons et al., 2003), and large-scale tectonic features and faults (Burov et al., 1998; Audet and Mareschal, 2004), while no agreements have yet been reached.

In order to better understand the relationship between T_e and lithospheric deformation, and to investigate the tectonic and geophysical meanings of T_e anisotropy, we study variations of T_e and its anisotropy at the Zagros-Himalaya belt and the surrounding regions. The Zagros-Himalaya belt is one of the most active continental deformation region that is surrounded by relative stable continental blocks, which makes the study region ideal to investigate the relationship between lithospheric strength and deformation. We first briefly introduce the tectonic background of the study region and the high resolution wavelet coherence method used to obtain T_e and its anisotropy. We then show our T_e and its anisotropy results, and compare them with different geological and geophysical data.

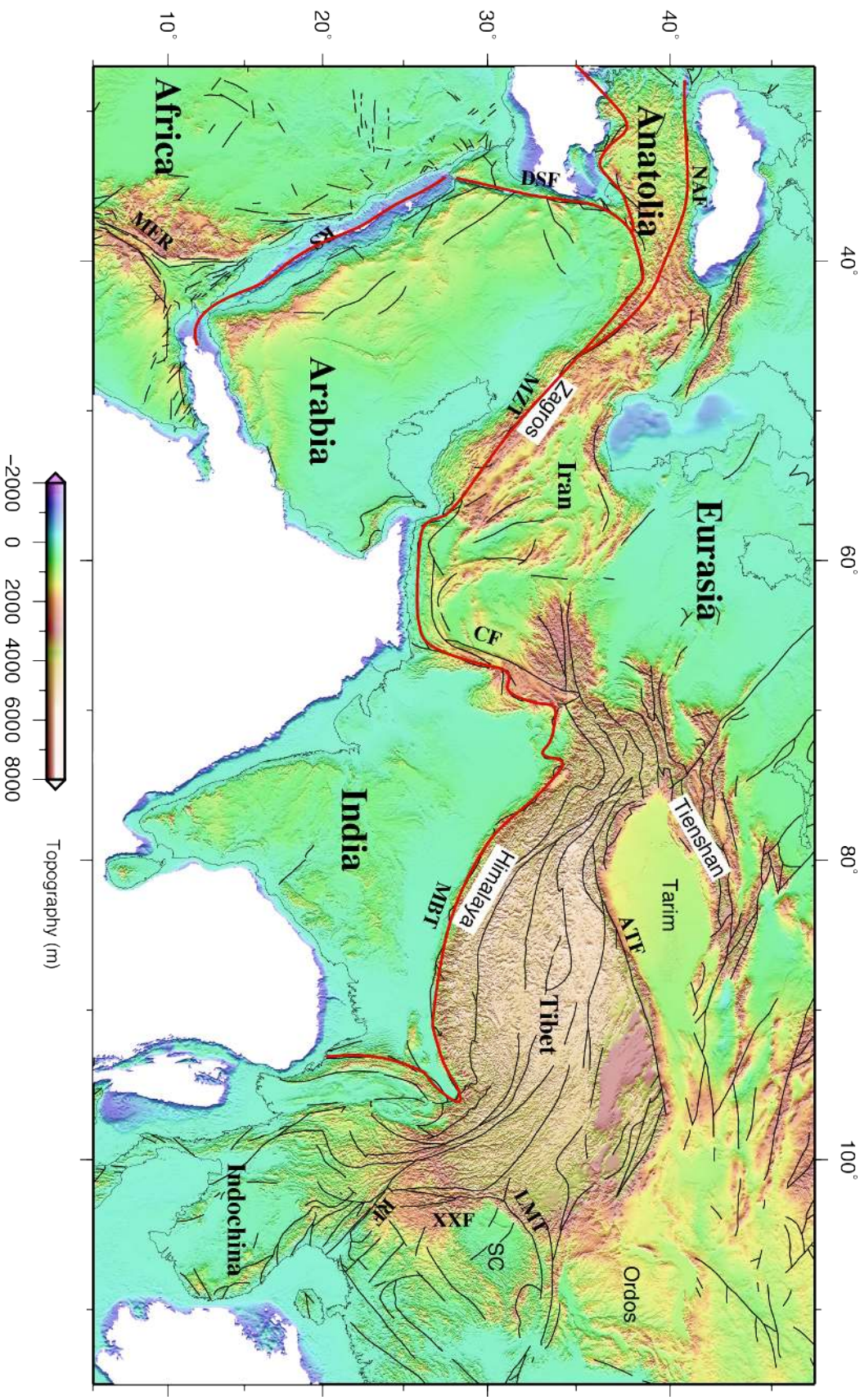
Africa
Anatolia
Arabia
Eurasia
India
Indochina
Iran
Tibet
Tarim
Ordos
Tienshan
Himalaya
Zagros
NAF
DSF
MER
MZT
CF
MBT
ATF
XXF
RF
LMT
SC
10°
20°
30°
40°
60°
80°
100°
−2000
0
2000
4000
6000
8000
Topography (m)

Figure 5.1: Map of Zagros-Himalaya belt and surrounding regions showing topography and major active faults (black line). Red line shows the major plate boundary. Abbreviations: ATF-Altyn Tagh fault, CF-Chaman fault, DSF-Dead Sea transform fault, LMT-Longmen Shan thrust belt, MBT-Main Boundary thrust, MZT-Main Zagros thrust, NAF-North Anatolian fault, RS-Red Sea, SC-Sichuan basin, and XXF-Xiangshuihe-Xiaojiang fault system.

5.2 Tectonic background

The Zagros and the Himalaya (Fig. 5.1) are two prominent mountain belts built by continental collisions of India-Asia and Arabia-Asia following the closure of the Neo-Tethyan Ocean in the early Paleogene (e.g., Yin, 2010). In the Himalaya, collision between India and Asia at 55-30 Ma shortened thrust belts in the southern and northern Tibet and created a large intracontinental basin. Subsequent crustal thickening and a possible thermal event in the mantle raised the elevation of the Tibet plateau up to its current height. Collision between India and Asia also caused lateral extrusion of southeast Asia between 32 Ma and 17 Ma. The latest stage of the India–Asia collision was expressed by north-trending rifting and the development of V-shaped conjugate strike-slip faults. In the Zagros, the Arabia-Asia collision casued the early crustal thickening in the orogenic interior at or prior to 30-20 Ma. This style of deformation was replaced by strike-slip faulting at ~15-5 Ma associated with further northward penetration of Arabia into Asia and the westward extrusion of the Anatolia block. Due to these two continental collisions, widespread active faultings and large earthquakes developed along the Zaros-Himalaya belt and extended into the interior of east Asia and southeast Asia (Fig. 5.1 and 5.2), and high deformation rates are observed in these regions (Kreemer et al., 2003). However, the interiors of India, Arabia, and Central Asia remain stable with almost no deformation.

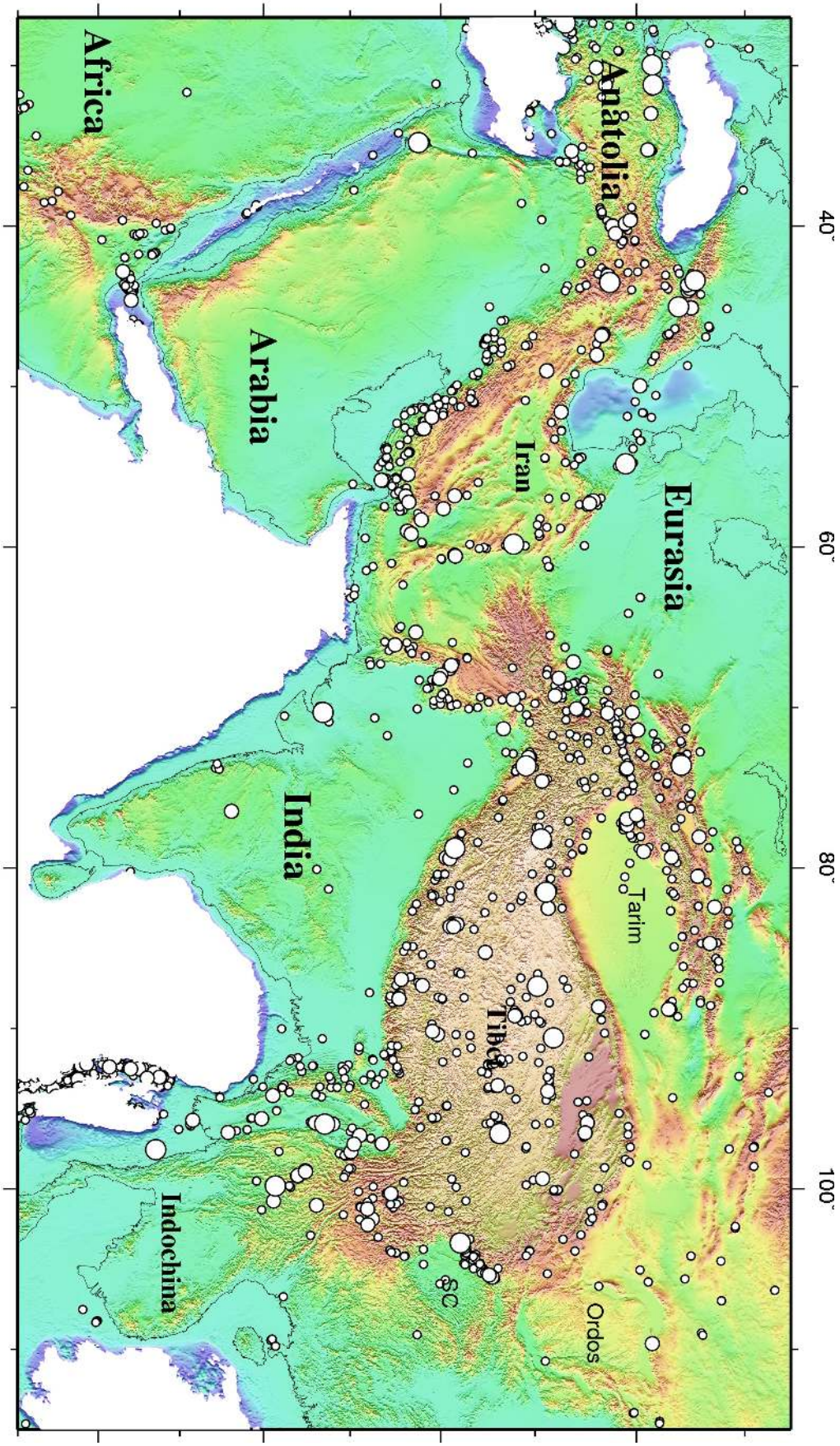
Africa
Anatolia
Arabia
Eurasia
Iran
India
Tarim
Tibet
SC
Ordos
Indochina
40°
30°
20°
10°
40°
60°
80°
100°
Ms > 5
Ms > 6
Ms > 7

Figure 5.2: Map of intermediate and large earthquakes between 1979 and 2017 with focal depth shallower than 50 km. Earthquake data are from U.S. Geological Survey.

5.3 Methods

We use a 'fan' wavelet based spectral method to calculate T_e and its anisotropy. The wavelet transform is a space-domain convolution of a signal with a wavelet, at a series of scales. It was first introduced into T_e calculations by Stark et al. (2003) in which they used the Derivative of Gaussian (DoG) wavelet to determine the variations of T_e in southern Africa. Later, Kirby and Swain (2004) showed that DoG wavelet yields over- or under-estimates of the Fourier spectra. A 'fan' wavelet, which is a superposition of two-dimensional Morlet wavelets, is employed by Kirby and Swain (2004) for isotropic T_e calculations, and by Kirby and Swain (2006) for anisotropic T_e estimate. Subsequently, 'fan' wavelet has been widely used to compute the variations of T_e and its anisotropy due to its convenience (there is no need to switch window size for different T_e values as in old spectral methods, e.g., the multi-taper method) (e.g., Tassara et al., 2007; Audet et al., 2007; Mao et al., 2012; Chen et al., 2015b).

For a 2D space-domain ($\boldsymbol{x}$) signal $g(\boldsymbol{x})$ with Fourier transform $G(\boldsymbol{k})$, its wavelet coefficients are computed via

$$\tilde{g}(s, \boldsymbol{x}, \theta) = \boldsymbol{F}^{-1}[G(\boldsymbol{k})\hat{\psi}_{s\theta}(\boldsymbol{k})], \tag{5.5}$$

where s and θ are the scale and azimuth of the Morlet wavelet, $\boldsymbol{F}^{-1}$ is the inverse 2D Fourier transform, $\hat{\psi}_{s\theta}(\boldsymbol{k})$ is the Fourier transform of the dilated, translated and rotated wavelet defined as

$$\hat{\psi}_{s\theta}(\boldsymbol{k}) = s\hat{\psi}(s\Omega^{-1}(\theta)\boldsymbol{k}) \tag{5.6}$$

$$\hat{\psi}(\boldsymbol{k}) = e^{\frac{-|\boldsymbol{k}-\boldsymbol{k_0}|^2}{2}} - e^{\frac{-(|\boldsymbol{k}|^2+|\boldsymbol{k_0}|^2)}{2}}, \tag{5.7}$$

where Ω is the rotation matrix, $\boldsymbol{k_0} = (|\boldsymbol{k_0}| \sin\theta, |\boldsymbol{k_0}| \cos\theta)$, and $|\boldsymbol{k_0}| = 2.668$. Equations (5.4) and (5.3) are the Fourier transformed 'mother' and 'daughter' wavelets respectively. The scale s can be converted to an 'equivalent Fourier wavenumber', k_F, by

$$k_F = \frac{|\boldsymbol{k_0}|}{s}. \tag{5.8}$$

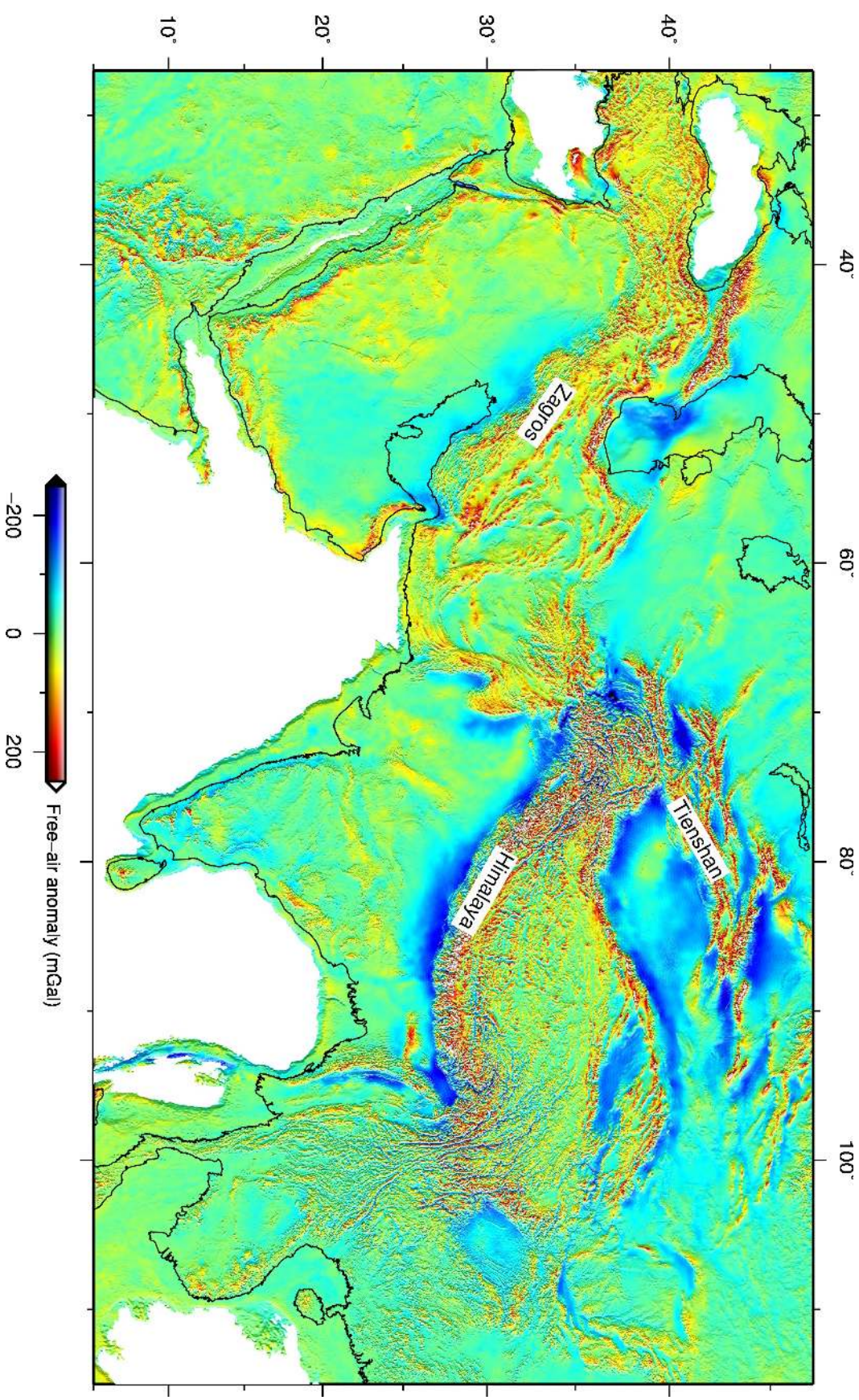
10°
20°
30°
40°
40°
60°
80°
100°
Zagros
Himalaya
Tienshan
−200
0
200
Free−air anomaly (mGal)

Figure 5.3: Map of free-air gravity anomaly. Strong negative anomalies in foreland basins and positive anomalies in mountains, e.g., Zagros, Himalaya and Tienshan regions, which may indicate flexural supporting from the lithosphere.

The square of the real part of coherency (SRC) between Bouguer gravity anomaly g and topography h is given by

$$\Gamma^2(s, \boldsymbol{x}) = \frac{(Re < \tilde{g}\tilde{h}^* >_\theta)^2}{< \tilde{g}\tilde{g}^* >_\theta < \tilde{h}\tilde{h}^* >_\theta}, \tag{5.9}$$

where Re is the real part used, * indicates complex conjugate, and the angular bracket denote an average over some azimuthal extent. The isotropic SRC is gained by averaging from 0° to 180° at the given scale and location, and the anisotropic SRC is derived by averaging over an azimuthal extent of 90° centered at the given central azimuth.

Following Forsyth (1985), with an assumed isotropic T_e for the uniform elastic plate, we perform load deconvolution to obtain the predicted coherence. The SRC curve for different scales at each space point is converted to wavenumber domain through equation (5.5), and compared with the predicted coherence curves with different assumed T_e to find the best-fitting isotropic T_e. Predicted anisotropic coherence curve is obtained by assuming T_{emax}, T_{emin} and the azimuth of T_{emin} for an orthotropic elastic plate (Kirby and Swain, 2006). Similar procedures are followed as in the isotropic T_e case to determine the three orthotropic elastic plate parameters at each space point. This method compares the 2-D wavelet coherence with orthotropic elastic plate given a large number of assumptions, which is debatable. However, the response of the lithosphere should in theory be close to that of a thin elastic plate, and the orthotropic elastic plate model has the advantage of determining physical estimates of the anisotropy (Audet and Mareschal, 2007).

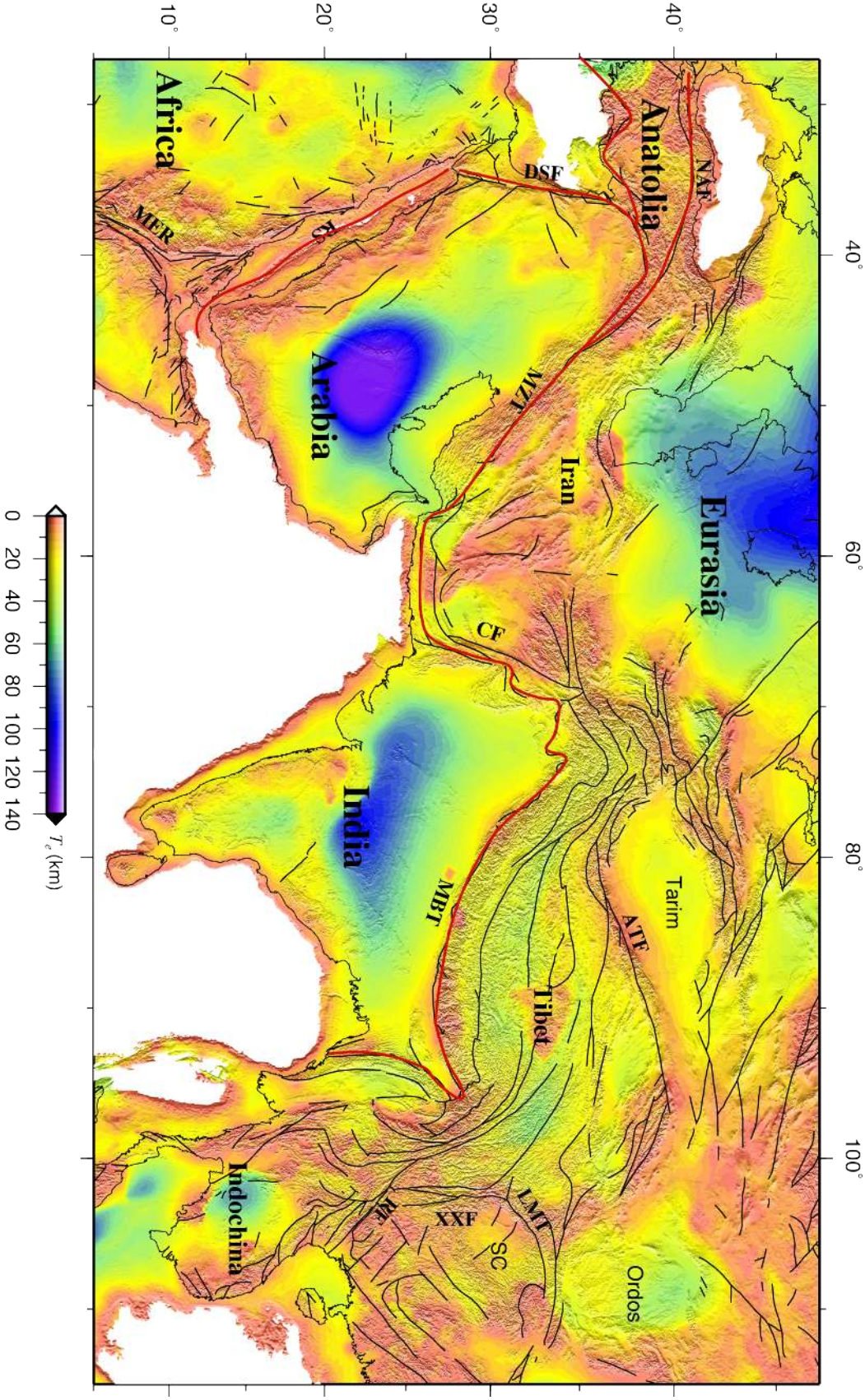
Africa
Anatolia
Arabia
Eurasia
India
Iran
Tarim
Tibet
Ordos
Indochina
NAF
DSF
EF
MEFR
MZT
CF
MBT
ATF
LMT
SC
XXF
RF
40°
60°
80°
100°
10°
20°
30°
40°
0 20 40 60 80 100 120 140
T_z (km)

Figure 5.4: Isotropic T_e distribution with major faults (black line) and plate boundaries (red line). Abbreviations are the same as Fig. 5.1.

5.4 Data

Our topography/bathymetry data are derived from ETOPO1 digital elevation model (DEM) (Amante, 2009), and our free-air gravity anomaly data are derived from the V18 Gravity Anomaly model (Sandwell and Smith, 2009). Free-air gravity anomaly data are shown in Figure 5.3. Strong negative free air anomalies in foreland basins and positive anomalies in mountains, e.g. Zagros, Himalaya and Tienshan regions, indicate flexural support from the lithosphere. Bouguer gravity anomaly data are obtained by performing complete terrain correction to free-air gravity anomaly (Fullea et al., 2008). To reduce boundary effects in spectral analyses, the original data cover a larger area than the study area (with each boundary extending out ~ 1500 km). Calculations of T_e and its anisotropy are on a geodetic coordinate system with 20 km x 20 km resolution grids, and Lambert conic conformal projection is used to transfer data and results between geographic and geodetic coordinates.

5.5 Results

Isotropic T_e

T_e in the study region varies from < 5 km to over 100 km and shows good correlation with geological and geophysical boundaries (Fig. 5.4). Along plate boundaries, mountain belts, and major faults, T_e is usually smaller than 30 km, e.g., the Red Sea spreading ridge, the Dead Sea transform fault, the North Anatolian fault, the Zagros belt, the Chaman fault, the Himalaya belt, the Tienshan belt, the Altyn Tagh fault, the Longmen Shan thrust belt, the Xiangshuihe-Xiaojiang fault system. T_e in basins is between 30-60 km, and generally increases with distance away from active boundaries, e.g., the Zagros and Himalaya foreland basins have T_e between 30-60 km, the Tarim basin has T_e between 30-40 km, the Junggar basin has T_e between 40-50 km, the Qaidam basin has T_e between 40-50 km, the Sichuan basin has T_e 30 km, and the Ordos basin has T_e between 30-50 km, with a stronger northern part and weaker southern part. Into the stable cratons, T_e is often larger than 60 km, e.g., the Arabian craton, the Indian craton, and the Central Asian craton. The Iranian Plateau has relatively uniform T_e of 30 km, and the Tibetan Plateau has a stripe-like T_e distribution, with larger T_e in terrains and smaller T_e in the suture zones.

There are two sharp T_e gradient regions near the stable cratons (Fig. 5.4). One is at the southern boundary of the Indian craton, which agrees well with the boundary

of Deccan Volcanic Province. The other one is at the southwest boundary of the Arabian craton, which is right next to the proposed mantle flow beneath the Arabian plate (e.g. Hansen et al., 2006). These two sharp T_e gradient regions may indicate thermal weakening of the lithospheric strength in stable craton regions.

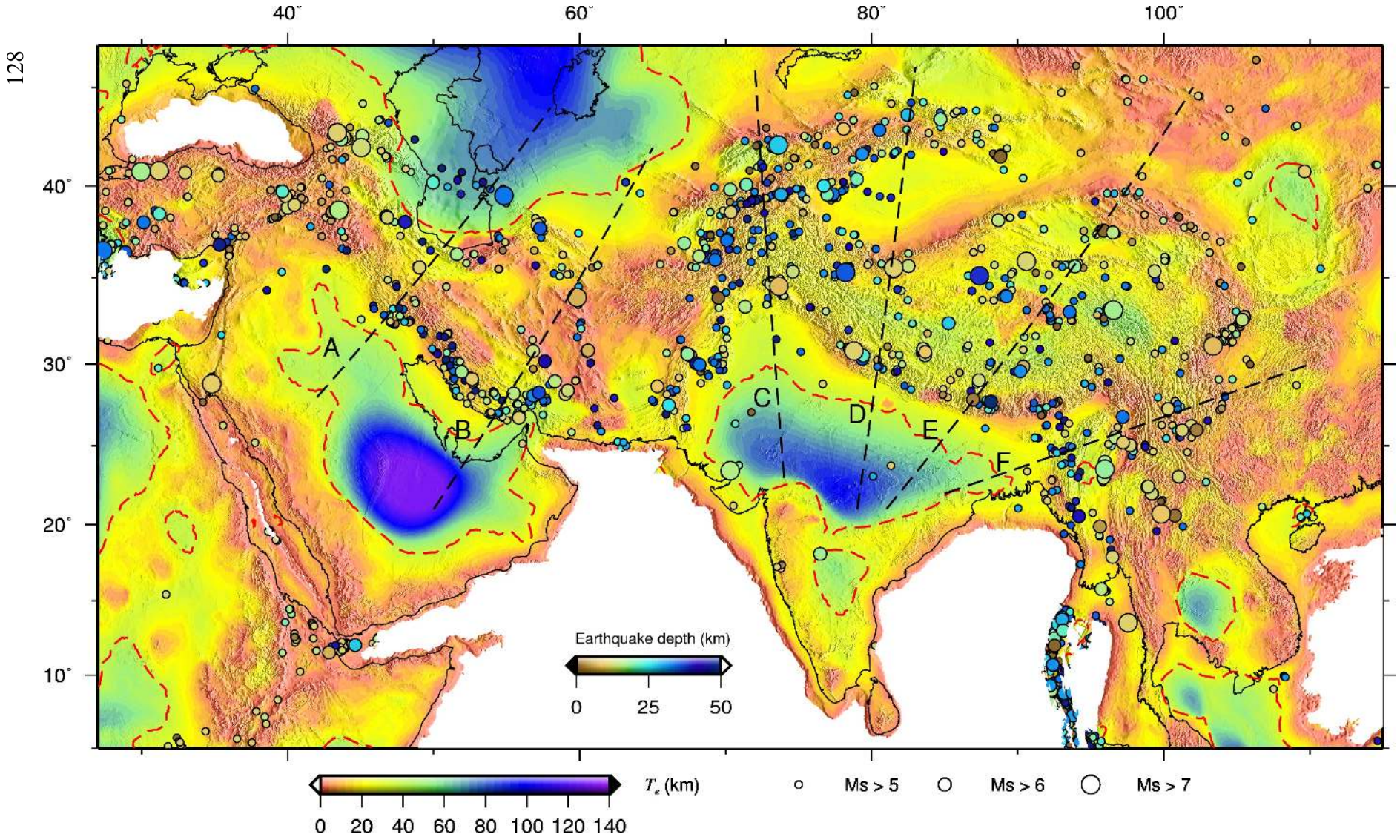
40˚
60˚
80˚
100˚
40˚
30˚
20˚
10˚
A
B
C
D
E
F
Earthquake depth (km)
0
25
50
T_e (km)
0 20 40 60 80 100 120 140
Ms > 5
Ms > 6
Ms > 7

Figure 5.5: T_e distribution with intermediate and large earthquakes between 1979 and 2018 with focal depth shallower than 50 km. Earthquake data are from U.S. Geological Survey. The red dashed line shows the T_e = 60 km contour.

T_e vs earthquake and other geophysical data

Our T_e variation shows good correlation with earthquake distribution (Fig. 5.5). Most intermediate and large earthquakes (Ms > 5) are limited in the region T_e smaller than 60 km, and they prone to occur at the high T_e gradient or relatively weak areas. When T_e is larger than 60 km, there are few earthquakes. The correlation between T_e variation and earthquake distribution is most obvious at the Tibetan Plateau. The stripe-like T_e variation leads to stripe-like earthquake distribution. The concentration of active lithospheric deformation within both low T_e and high T_e gradient regions imply that lithospheric deformation is controlled by T_e distribution, while at the same time, lithospheric deformation (mechanical weakening) reduces lithospheric strength. However, when the lithosphere is strong enough (T_e is larger than 60 km), mechanical weakening is ignorable.

We then compare T_e with other geophysical data on different sections which cross both low-intermediate and high T_e regions (Fig. 5.6). We see that wherever topography varies sharply (active tectonic region), lithospheric strength is low, and T_e is usually smaller than the crust thickness, which indicates that the lithospheric strength is limited in the crust, and the lithospheric mantle is weak in the active regions. While, when the topography is flat (stable region), T_e is usually large and deeper than the Moho depth, which shows that in the stable regions, lithospheric mantle is strong and contributes to a large amount of the total strength. Thick sediments in these cross sections correspond to foreland basins. We observe that T_e decreases rapidly at these areas, which suggests that the bending of the lithosphere reduces the lithospheric strength largely. All large earthquakes (Ms > 7) happen at a shallower depth than T_e, which shows that large earthquakes occur within the elastic core of the vertically stratified lithosphere.

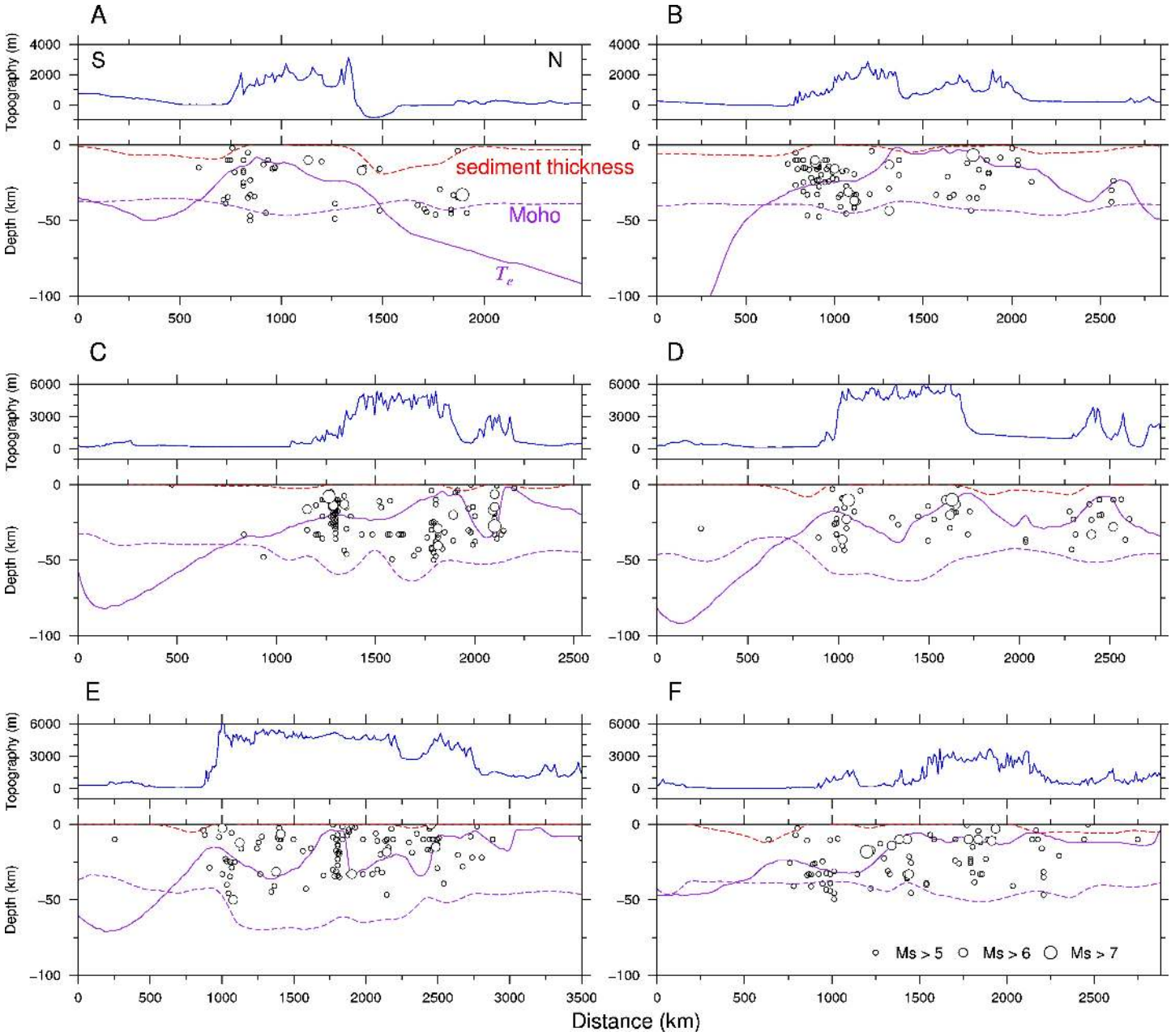

Figure 5.6: Cross sections showing the effective elastic thickness (purple line), Moho depth (dashed purple line), sediment thickness (red line) and topography (blue line). Positions of these cross sections are shown in Figure 5.5. Both the Moho depth and sediment thickness data are from crust 1.0 model (Laske et al., 2013).

T_e anisotropy map

Both the weak direction and extent of T_e anisotropy vary substantially over the region (Fig. 5.7). At large thrust faults, e.g., the thrust fault between Tianshan and Tarim and the Main Boundary thrust between India and Tibet, weak direction tends to be perpendicular to the fault strike. At large strike-slip faults, e.g., the Chaman fault, weak direction seems to be parallel to the fault strike. At the spreading center, e.g., the Rea Sea, weak direction is perpendicular to the spreading axis. At these three different fault types mentioned above, the T_e anisotropic directions are generally consistent with the maximum principal stress directions in the crust, which suggests that mechanical weakening could be an efficient mechanism in reducing lithospheric strength in these relative weak regions. At the Main Zagros thrust, the weak direction of T_e anisotropy is complex, which may be related to the fact that both thrust and strike-slip components are large on this fault. In the Zagros foreland basin, the dominant weak direction is the northwest and southeast direction. In the Himalaya foreland basin, the weak direction is not clear. In the Tarim basin, the weak direction changes from north-south direction in the western part to west-east direction in the eastern part. In the Ordos basin, the weak direction is west-east direction. In the interior of stable cratons, the anisotropic extent is usually restricted, which indicates little deformation within the strong lithosphere.

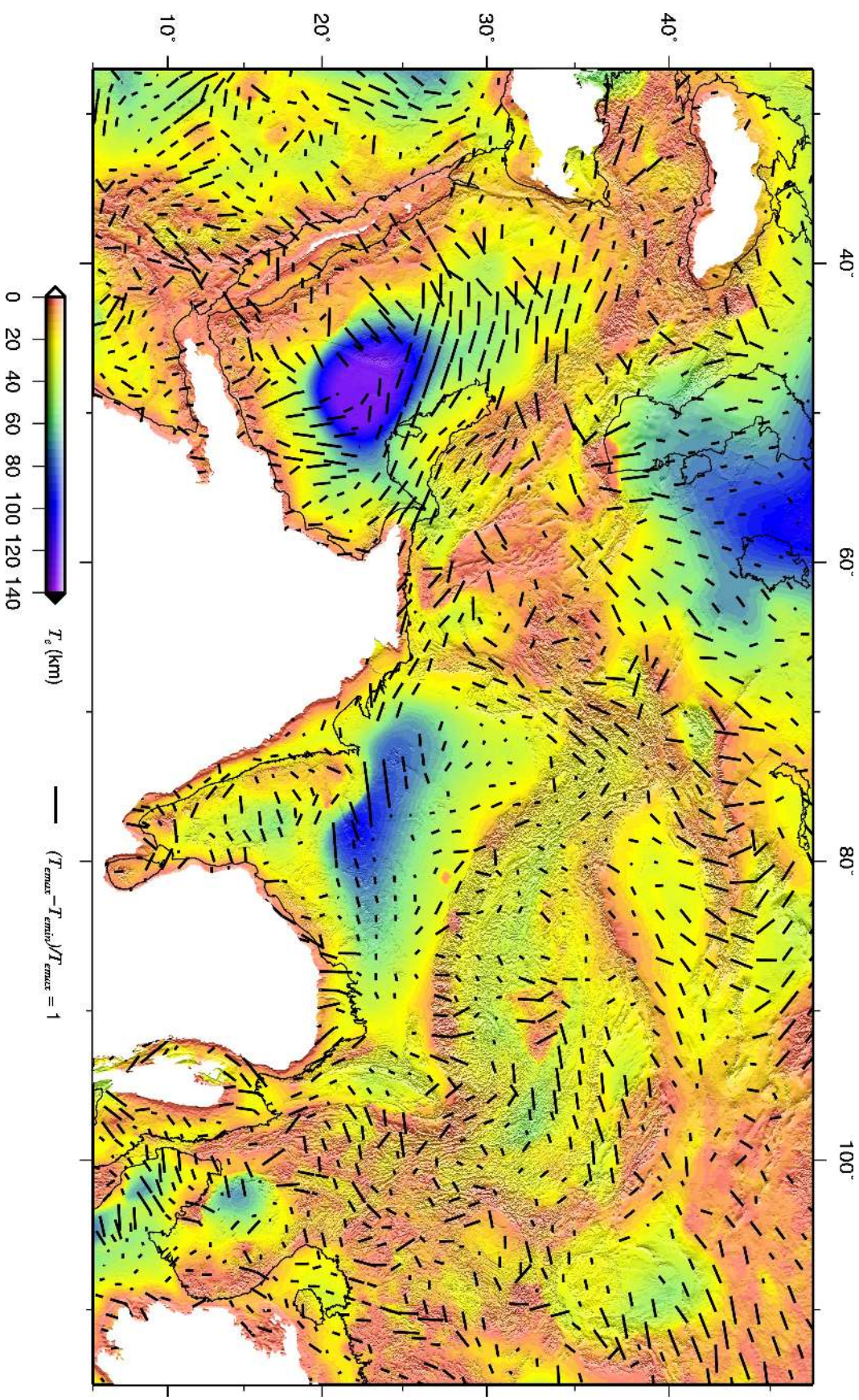
10°
20°
30°
40°
40°
60°
80°
100°
0 20 40 60 80 100 120 140
T_e (km)
$(T_{emax}-T_{emin})/T_{emax}=1$

Figure 5.7: Direction and extent of T_e anisotropy mapped on isotropic T_e variation. Orientation of black line shows the weakest direction of the lithospheric strength.

T_e anisotropy vs other geophysical data

Comparing to GPS velocities respect to Eurasia (Fig. 5.8b), our T_e anisotropic direction agrees with surface movement except within the Zagros. The agreements are most obvious around the Tibetan Plateau, where the north-south collision in the west and eastward extrusion in the east are all well represented in the weak directions of T_e anisotropy. The maximum principal stress directions (Fig. 5.8c) are also generally consistent with our weak T_e directions. Agreements between our weak T_e directions and these crustal stress and strain indicators further confirm that mechanical weakening resulted from yielding under plate boundary forces is the main weakening mechanism of the lithospheric strength in the low and intermediate T_e region.

Another way of comparing anisotropic extents is mapping the maximum to minimum T_e ratio (Fig. 5.8d). Dominant parts of continental lithosphere in the study region have ratios between 1-2, but several areas have larger anisotropic ratios (up to 4-5). The lithospheric strength, D, is proportional to the third power of T_e, which means that the azimuthal difference in the lithospheric strength could be larger than 10 times in these areas. One striking anisotropic band lies in the central-western part of the Arabian plate, and it extends north-south. Shear-wave splitting (SKS) studies (e.g., Hansen et al., 2006) show that mantle flow beneath that region is in also in north-south direction, and tomography from seismic travel time and waveform inversions (e.g., Chang and Van der Lee, 2011) indicates that a channelized mantle flow exists beneath Arabian plate. Comparing with the isotropic T_e distribution, we can see that this band corresponds to large T_e changes. The T_e anisotropic direction in this regions is not consistent with the general northwest-southeast weak direction of the other part of the Arabian plate. Together, they show that thermal weakening from mantle flow reduced the lithospheric strength in this region.

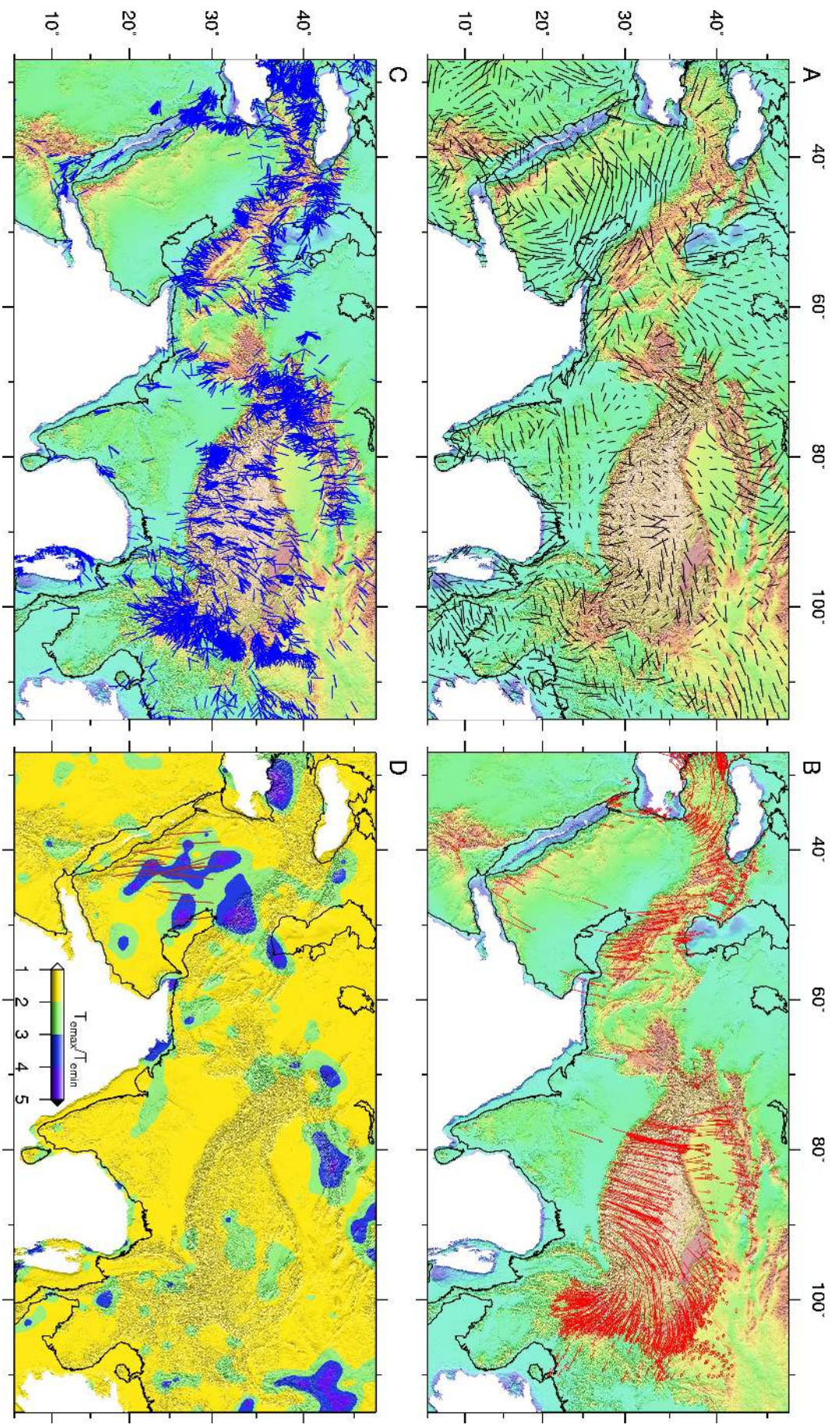
A
B
C
D
40°
60°
80°
100°
10°
20°
30°
40°
T_{emax}/T_{emin}
1
2
3
4
5

Figure 5.8: (a) T_e anisotropy mapped on topography. (b) GPS velocities respect to Eurasia over map of topography. GPS data are taken from Gan et al. (2007); Mohadjer et al. (2010); Reilinger et al. (2006); Walpersdorf et al. (2006). (c) Maximum principal stress direction in the crust (Heidbach et al., 2016) over map of topography. (d) Map of the azimuthal differentiation ratio of T_e. Brown lines show the SKS direction (Hansen et al., 2006), which is generally thought to be the direction of channelized mantle flow beneath the Arabian plate.

5.6 Discussion and conclusions

Our results of T_e and its anisotropy in the Zagros-Himalaya belt and surrounding regions show good correlations with geological and geophysical observations. Along plate boundaries, mountain belts and major faults, T_e is usually smaller than 30 km. In the basins, T_e is between 30 - 60 km. In the stable cratons, T_e is larger than 60 km. Earthquake is prone to occur at the high T_e gradient or relatively low T_e region when T_e is smaller than 60 km. Few earthquakes occur when T_e is larger than 60 km. In the regions with low and intermediate strength (T_e < 60 km), the extent of T_e anisotropy is usually large, and the weak direction of T_e anisotropy agrees well with GPS and crustal stress.

Our results also suggest that in the active regions and basins, the lithosphere can not transmit plate boundary forces efficiently and yields under the applied forces, while in the stable craton regions, the lithosphere is strong enough to transmit boundary forces efficiently with little internal deformation. We conclude that mechanical weakening is the dominate mechanism to reduce the lithospheric strength in regions where T_e is smaller than 60 km, while in stable cratons, the effects of mechanical weakening can be ignored, and only thermal weakening resulted from mantle processes can modify the lithospheric strength substantially.

One potential shortage of using spectral methods to calculate T_e variation is related to the uniform elastic plate assumption in the forward prediction step. Lithospheric strength varies substantially in space, while during load deconvolution, the elastic plate is assumed to be uniform in space. The idea is that the inverted T_e represents averaged or characteristic lithospheric strength in this region centered at this grid point. Therefore, this assumption tends to smoothen the actual T_e variations in space. The absolute T_e values in our results may be affected by this smoothening. However, our conclusion of the interactions between T_e and lithospheric deformation is unlikely to be affected since the general trends of low and high of the T_e variations are not changed by the smoothening.

References

Amante, Christopher (2009). ETOPO1 1 arc-minute global relief model: procedures, data sources and analysis. *http://www. ngdc. noaa. gov/mgg/global/global. html*.

Audet, Pascal and Roland Bürgmann (2011). Dominant role of tectonic inheritance in supercontinent cycles. *Nature Geoscience*, 4(3):184–187. doi: 10.1038/ngeo1080.

Audet, Pascal and Jean-Claude Mareschal (2004). Anisotropy of the flexural response of the lithosphere in the Canadian Shield. *Geophysical Research Letters*, 31(20). doi: 10.1029/2004gl021080.

Audet, Pascal and Jean-Claude Mareschal (2007). Wavelet analysis of the coherence between Bouguer gravity and topography: application to the elastic thickness anisotropy in the Canadian Shield. *Geophysical Journal International*, 168(1): 287–298. doi: 10.1111/j.1365-246x.2006.03231.x.

Audet, Pascal, A Mark Jellinek, and Hideharu Uno (2007). Mechanical controls on the deformation of continents at convergent margins. *Earth and Planetary Science Letters*, 264(1-2):151–166. doi: 10.1016/j.epsl.2007.09.024.

Burov, E, C Jaupart, and JC Mareschal (1998). Large-scale crustal heterogeneities and lithospheric strength in cratons. *Earth and Planetary Science Letters*, 164 (1-2):205–219. doi: 10.1016/s0012-821x(98)00205-2.

Chang, Sung-Joon and Suzan Van der Lee (2011). Mantle plumes and associated flow beneath Arabia and East Africa. *Earth and Planetary Science Letters*, 302 (3-4):448–454. doi: 10.1016/j.epsl.2010.12.050.

Chen, Bo, Mikhail K Kaban, Sami El Khrepy, and Nassir Al-Arifi (2015a). Effective elastic thickness of the Arabian plate: Weak shield versus strong platform. *Geophysical Research Letters*, 42(9):3298–3304. doi: 10.1002/2015gl063725.

Chen, Bo, Jianxin Liu, Chao Chen, Jinsong Du, and Ya Sun (2015b). Elastic thickness of the Himalayan–Tibetan orogen estimated from the fan wavelet coherence method, and its implications for lithospheric structure. *Earth and Planetary Science Letters*, 409:1–14. doi: 10.1016/j.epsl.2014.10.039.

Chen, Bo, Carina Haeger, Mikhail K Kaban, and Alexey G Petrunin (2017). Variations of the effective elastic thickness reveal tectonic fragmentation of the Antarctic lithosphere. *Tectonophysics*. doi: 10.1016/j.tecto.2017.06.012.

Forsyth, Donald W (1985). Subsurface loading and estimates of the flexural rigidity of continental lithosphere. *Journal of Geophysical Research: Solid Earth*, 90 (B14):12623–12632. doi: 10.1029/jb090ib14p12623.

Fullea, J, M Fernandez, and H Zeyen (2008). FA2BOUG—A FORTRAN 90 code to compute Bouguer gravity anomalies from gridded free-air anomalies: Application to the Atlantic-Mediterranean transition zone. *Computers & Geosciences*, 34(12):1665–1681. doi: 10.1016/j.cageo.2008.02.018.

Gan, Weijun, Peizhen Zhang, Zheng-Kang Shen, Zhijun Niu, Min Wang, Yongge Wan, Demin Zhou, and Jia Cheng (2007). Present-day crustal motion within the Tibetan Plateau inferred from GPS measurements. *Journal of Geophysical Research: Solid Earth*, 112(B8). doi: 10.1029/2005jb004120.

Hansen, Samantha, Susan Schwartz, Abdullah Al-Amri, and Arthur Rodgers (2006). Combined plate motion and density-driven flow in the asthenosphere beneath Saudi Arabia: Evidence from shear-wave splitting and seismic anisotropy. *Geology*, 34(10):869–872. doi: 10.1130/g22713.1.

Heidbach, Oliver, Mojtaba Rajabi, Karsten Reiter, and Moritz Ziegler (2016). World stress map 2016. *Science*, 277:1956–1962.

Kirby, JF and CJ Swain (2004). Global and local isostatic coherence from the wavelet transform. *Geophysical research letters*, 31(24). doi: 10.1029/2004gl021569.

Kirby, JF and CJ Swain (2006). Mapping the mechanical anisotropy of the lithosphere using a 2D wavelet coherence, and its application to Australia. *Physics of the Earth and Planetary Interiors*, 158(2-4):122–138. doi: 10.1016/j.pepi.2006.03.022.

Kirby, JF and CJ Swain (2011). Improving the spatial resolution of effective elastic thickness estimation with the fan wavelet transform. *Computers & geosciences*, 37(9):1345–1354. doi: 10.1016/j.cageo.2010.10.008.

Kreemer, Corné, William E Holt, and A John Haines (2003). An integrated global model of present-day plate motions and plate boundary deformation. *Geophysical Journal International*, 154(1):8–34. doi: 10.1046/j.1365-246x.2003.01917.x.

Laske, Gabi, Guy Masters, Zhitu Ma, and Mike Pasyanos (2013). Update on CRUST1. 0—A 1-degree global model of Earth's crust. In *Geophys. Res. Abstr.*, volume 15, page 2658.

Lowry, Anthony R and Marta Pérez-Gussinyé (2011). The role of crustal quartz in controlling Cordilleran deformation. *Nature*, 471(7338):353. doi: 10.1038/nature09912.

Lowry, Anthony R and Robert B Smith (1994). Flexural rigidity of the Basin and Range-Colorado Plateau-Rocky Mountain transition from coherence analysis of gravity and topography. *Journal of Geophysical Research: Solid Earth*, 99(B10):20123–20140. doi: 10.1029/94jb00960.

Lowry, Anthony R and Robert B Smith (1995). Strength and rheology of the western US Cordillera. *Journal of Geophysical Research: Solid Earth*, 100(B9): 17947–17963. doi: 10.1029/95jb00747.

Mao, Xiaolin, Qin Wang, Shaowen Liu, Minjie Xu, and Liangshu Wang (2012). Effective elastic thickness and mechanical anisotropy of South China and surrounding regions. *Tectonophysics*, 550:47–56. doi: 10.1016/j.tecto.2012.05.019.

Mohadjer, S, R Bendick, A Ischuk, S Kuzikov, A Kostuk, U Saydullaev, S Lodi, DM Kakar, A Wasy, MA Khan, et al. (2010). Partitioning of India-Eurasia convergence in the Pamir-Hindu Kush from GPS measurements. *Geophysical Research Letters*, 37(4). doi: 10.1029/2009gl041737.

Pirouz, Mortaza, Jean-Philippe Avouac, Adriano Gualandi, Jamshid Hassanzadeh, and Pietro Sternai (2017). Flexural bending of the Zagros foreland basin. *Geophysical Journal International*, 210(3):1659–1680. doi: 10.1093/gji/ggx252.

Reilinger, Robert, Simon McClusky, Philippe Vernant, Shawn Lawrence, Semih Ergintav, Rahsan Cakmak, Haluk Ozener, Fakhraddin Kadirov, Ibrahim Guliev, Ruben Stepanyan, et al. (2006). GPS constraints on continental deformation in the Africa-Arabia-Eurasia continental collision zone and implications for the dynamics of plate interactions. *Journal of Geophysical Research: Solid Earth*, 111(B5). doi: 10.1029/2005jb004051.

Sandwell, David T and Walter HF Smith (2009). Global marine gravity from retracked Geosat and ERS-1 altimetry: Ridge segmentation versus spreading rate. *Journal of Geophysical Research: Solid Earth*, 114(B1). doi: 10.1029/2008jb006008.

Simons, Frederik J, Rob D van der Hilst, and Maria T Zuber (2003). Spatiospectral localization of isostatic coherence anisotropy in Australia and its relation to seismic anisotropy: Implications for lithospheric deformation. *Journal of Geophysical Research: Solid Earth*, 108(B5). doi: 10.1029/2001jb000704.

Stark, CP, J Stewart, and CJ Ebinger (2003). Wavelet transform mapping of effective elastic thickness and plate loading: Validation using synthetic data and application to the study of southern African tectonics. *Journal of Geophysical Research: Solid Earth*, 108(B12). doi: 10.1029/2001jb000609.

Tassara, Andrés, Chris Swain, Ron Hackney, and Jon Kirby (2007). Elastic thickness structure of South America estimated using wavelets and satellite-derived gravity data. *Earth and Planetary Science Letters*, 253(1-2):17–36. doi: 10.1016/j.epsl.2006.10.008.

Walpersdorf, Andrea, Denis Hatzfeld, H Nankali, Farokh Tavakoli, Faramarz Nilforoushan, M Tatar, P Vernant, J Chéry, and F Masson (2006). Difference in the GPS deformation pattern of North and Central Zagros (Iran). *Geophysical Journal International*, 167(3):1077–1088. doi: 10.1111/j.1365-246x.2006.03147.x.

Watts, Anthony Brian (2001). *Isostasy and Flexure of the Lithosphere*. Cambridge University Press.

Yin, An (2010). Cenozoic tectonic evolution of Asia: A preliminary synthesis. *Tectonophysics*, 488(1-4):293–325. doi: 10.1016/j.tecto.2009.06.002.

Zhang, Peizhen, Qidong Deng, Guomin Zhang, Jin Ma, Weijun Gan, Wei Min, Fengying Mao, and Qi Wang (2003). Active tectonic blocks and strong earthquakes in the continent of China. *Science in China Series D: Earth Sciences*, 46 (2):13–24. doi: 10.1002/cjg2.699.

Chapter 6

CONCLUSION

With numerical models constrained by different geological and geophysical observations, we studied the lithosphere and mantle dynamics at different locations over short and long timescales. With gravity and topography data, we investigated the interactions between the mechanical strength and lithospheric deformations in continental collision region. Our results provide some new insights into a comprehensive understanding of the lithosphere and mantle dynamics and demonstrate the strength of integrating numerical models with observations in revealing complex Earth processes.

In Chapter 2, we developed a multiphysics approach to simulate subduction zone evolution and to predict subduction zone topography. We discussed the influences of different geophysical, petrological and geochemical processes at subduction zones. We show that surface geometry, surface processes, elasticity, and oceanic crust have strong influences on the stress state and deformation within plates, water weakening decouples the overriding plate and the subducting slab at the mantle wedge region and contributes to the initiation of overriding plate failure, and oceanic crust has similar effects with sediments on lubricating the subduction interface. We also show that free slip surface topography and free surface topography have substantial differences, and free surface topography is influenced by different processes though adjusting the complex force balance. Our model of the New Hebrides Subduction Zone explains the origin of isolated deep earthquakes and the difference in the seismic intensities between the northern and southern deep earthquake clusters. With the multiphysics approach we developed, we are able to predict subduction zone topography as well as realistic slab behavior.

In Chapter 3, we tested the influence of inherited lithospheric heterogeneity on subduction initiation. We built a geodynamic model for the Puysegur Incipient Subduction Zone (PISZ) south of New Zealand. With a vertical preexisting weak zone, the compression between two plates leads to the formation of a new thrust fault on the subducting plate. Eventually, the thrust fault evolves into a new subduction interface, while the preexisting weak zone becomes a vertical fault inboard of the thrust fault. Our results are consistent with the two-fault system at PISZ, while the

initial condition is very simple. Our model also provides important insights into how subduction initiates at fracture zones and transform faults, where the initial weak zone may have mechanically unfavorable dip angles. Strike-slip motions on the Puysegur Ridge and the Puysegur subduction interface are ignored in our 2D model, which may have some influence on the stress evolution during subduction initiation. Since about 20 Ma, a large component of the relative plate motion between the Australian plate and Pacific plate was absorbed by strike-slip movements on the two faults, and the related accumulated plastic strain would have contributed to the weakening of the faults. Without taking this into consideration, our 2D model may predict a higher resistant force during the subduction initiation.

In Chapter 4, we investigated the scaling between damage zone thickness and fault width with 3D dynamic rupture simulations. Our 3D dynamic rupture simulations and fracture mechanics arguments indicate that damage zone thickness is ultimately bounded in long faults by the limiting effect of seismogenic depth on the efficiency of stress concentration near a rupture front. We provide a quantitative prediction of the relation between limiting damage zone thickness, state of stress, dynamic fault strength, off-fault yield strength and seismogenic depth, which we can compare to field observations. We conclude that short term damage processes are essential in the evolution of fault zone structure. In our simulations, we inhibit the effects of free surface by increasing the cohesion near the free surface, which may be unrealistic. The scaling between damage zone thickness and fault width can be influenced by the free surface effects. For instance, free surface effects can contribute a factor 2, resulting from the effective doubling of W by a mirror-image rupture.

In Chapter 5, we studied the interactions between mechanical strength and lithospheric deformations in continental collision region. Our results of T_e and its anisotropy in the Zagros-Himalaya belt and surrounding regions show good correlations with other geological and geophysical data. Along plate boundaries, mountain belts and major faults, T_e is usually smaller than 30 km. In the basins, T_e is between 30 - 60 km. In the stable cratons, T_e is larger than 60 km. The weak direction of T_e anisotropy is a good indicator for the active deformation direction and agrees well with the surface GPS and stress data. Our results suggest that mechanical weakening is the dominate mechanism for the reduction of lithospheric strength in the regions with low and intermediate T_e values (< 60 km), while in the high T_e (> 60 km) region, thermal weakening is more efficient modifying the lithospheric strength. The uniform elastic plate assumption in the forward prediction step contradicts with the

goal of mapping T_e variations. We suggest that this assumption tends to smoothen the actual T_e variations in space, and the absolute T_e values in our results may be affected by this smoothening. However, our conclusion of the interactions between T_e and lithospheric deformation is unlikely to be affected since the general trends of low and high of the T_e variations are not changed by the smoothening.

Moving forward, the multiphysics geodynamic approach we developed is powerful to simulate subduction zone evolution, while is currently computationally expensive. Some further work is still needed in order to make it more efficient, e.g., including adaptive mesh refinement to reduce the computation involved for high resolution model. Lithospheric heterogeneities play important roles in influencing the long term evolution of the lithosphere and mantle system, while the formation of these heterogeneities is also related to short term damage processes. However, short and long term processes are currently separated from each other in numerical models. Combination of both short and long term processes in a consistent numerical model is potentially an important direction. The mechanical strength and anisotropy are important properties of the lithosphere, while no numerical models take advantage of the variation of T_e and its anisotropy estimated from gravity and topography data. Incorporating this valuable piece of data into numerical models may contribute to a better fitting between model predictions of lithospheric deformations and observations.